Physicochemical and Cellular Analysis of Polydopamine for Use as an Orthopaedic Bioadhesive

Submitted in partial fulfillment of the requirements for the degree of

Masters of Applied Science

by

Alexander Steeves, BSc. (Hon)

uOttawa

June, 2018

DECLARATION

I hereby declare that the thesis entitled "Physicochemical and Cellular Analysis of Polydopamine for Use as an Orthopedic Bioadhesive" submitted by me, for the award of the degree of *Master's of Applied Science* from the University of Ottawa, is a record of bonafide work carried out by me under the supervision of Dr. Fabio Variola, PhD, Faculty of Engineering, University of Ottawa. I further declare that the work reported in this thesis has not been submitted and will not be submitted, either in part or in full, for the award of any other degree or diploma in this institute or any other institute or university.

The first study, **Evaluation of the direct effects of poly(dopamine) on the *in vitro* response of human osteoblastic cells**, was a joint effort between Dr. Fabio Variola, Aman Atwal and myself. SEM, AFM and LC-MS data processing was conducted by Aman Atwal. Raman and ATR-FTIR spectroscopy was performed by Dr. Variola. In its entirety, sample preparation, cell culture and RT-PCR was performed by myself. Specifics for cell culture include the selection of cell model, culturing, procedure, processing, imaging and analysis for all cell proliferation, spreading and focal adhesion experiments. Specifics for RT-PCR include designing of primers, cDNA synthesis, optimization, experimentation and analysis. Figure generation was completed by Dr. Variola and myself. The manuscript was written by Dr. Variola with contribution by myself in the cell culture section.

The second study, **Method of deposition affects physicochemical, bioactive and serum-independent components of polydopamine coatings**, was designed and executed in its entirety by myself and am the sole author of relevant written work.

ABSTRACT

Polydopamine (PDA), a unique bioinspired polymer, has been a subject of interest in fields including orthopedic biomaterials and antibacterial surfaces. Its osteogenic effects and ability to control surface traits through precise variables (e.g., pH, temperature) have led to its use as a coating in the enhancement of a wide range of materials, including metals and ceramics. In this Thesis, two studies were carried out to better understand the capability and mechanism of PDA-mediated bioactivity. In the first study, we investigated whether PDA coatings can further enhance the bioactivity of nanoporous Titanium (NPTi). While physicochemical traits were in line with literature, PDA was effective in enhancing cell proliferation, beyond NPTi, as early as 8 hours with enhancement in cell spreading and focal adhesion prevalence as early as 1 hour. No changes in adsorptive capacity were found, suggesting a serum-independent component (SIC) of the surface. The second study was focused on (1) determining how treatment parameters influence the physiochemical makeup of PDA surfaces, (2) assessing how PDA surfaces influence stem cell behavior and (3) confirming and investigating the SIC of PDA effect. Results confirm that there is indeed a SIC of PDA coatings with enhancement in cell spreading that improves with the increased size and density of PDA particles. Our findings show that the SIC works in concert with circulating sera to elicit the bioactive effects of PDA. The novel rPDA surface, obtained by adding rotation during the coating deposition, is also shown to elevate bioactivity during normal culturing, beyond classical coatings, with ongoing work suggesting enhancement in the osteogenic differentiation of hMSCs. Taken together, this work has demonstrated novel aspects underlying the potential and mechanism of action for the bioactivity of PDA, ultimately providing new evidence supporting the use of PDA as a biomedical material.

ACKNOWLEDGEMENT

With immense pleasure and deep sense of gratitude, I wish to express sincere thanks to my supervisor **Dr. Fabio Variola**, without his motivation and guidance, this research would not have been successfully completed. In addition, I'd like to thank him for his faith in my interests and aptitude, allowing the research freedom (and funds) to attempt experiments that weren't always completely flushed out, though he didn't know it at the time.

I express my sincere thanks to my lab mates **Usman Syed**, **Dilara Jakupovic**, **Eleanor Gerson**, **William Ho** and **Andrew Irwin** for their continued support, encouragement and shared love for food and caffeine (especially AYCE sushi).

I wish to extend my profound sense of gratitude to my parents **David** and **Carol Steeves** for providing me with not only the love, support and resources that allowed me to complete my research but also giving me the opportunity to come home to our magical basement couch where all anxiety and worries can wash away. While they didn't always understand the work I was doing, it that never stopped them from trying.

To my *brosif* **Ryan Steeves**, who always has my best interests in heart and has been a constant been a source of protection, love and reason at any time of the day, no matter what. Also love and thanks to his much better half **Samantha Steeves** for keeping him in line.

Last but not the least, I would like to thank my girlfriend **Zahra Wells** and a true mans best friend **Pablo Bear**. Zahra and Pablo have always been in my corner and provided a constant and loving support throughout the highs and lows with their only demands being for treats, walks and scratches.

TABLE OF CONTENTS

LIST OF FIGURES

LIST OF TABLES

LIST OF TERMS AND ABBREVIATIONS

AFM	Atomic Force Microscopy
AGC	Automatic Gain Control
ANOVA	Analysis of Variance
ATR-FTIR	Attenuated Total Reflection, Fourier Transform Infrared spectroscopy
BSG	Borosilicate Glass
BSP	Bone Sialoprotein
CCD	Charge-Coupled Device
CCRI	Centre for Catalysis Research and Innovation
Cdc42	Cell division control protein 42 homolog
cDNA	complementary DNA
CTRL	Control (condition)
DAPI	4’,6-Diamidino-2-Phenylindole
DHI	Dihydroxyindole
DMEM	Dulbecco’s Modified Eagle Medium
DMT	Derjaguin, Muller and Toporov model (elastic modulus)
DNA	Deoxyribonucleic Acid
dNTP	Nucleoside Triphosphate
DOPA	3,4-dihydroxy-1-phenylalinine
DPFM	Digitial Pulsed Force Mode

DTT	Dithiothreitol
ECM	Extracellular Matrix
EtOH	Ethyl alcohol
ERK	Extracellular signal Regulated Kinase
EGF	Epidermal Growth Factor
FA	Focal Adhesion
FAK	Focal Adhesion Kinase
FBS	Fetal Bovine Serum
FT-IR	Fourier Transform Infrared Spectrometry
FX	Focal Complex
GAP	GTPase-Activating Protein
GEF	Guanine Nucleotide Exchange Factor
GDP	Guanosine Diphosphate
GTP	Guanosine Triphosphate
H_2O_2	Hydrogen Peroxide
H_2SO_4	Sulfuric Acid
HCl	Hydrochloride (salt)
hMSC	Human Mesenchymal Stem Cell
hVIN1	Human anti-Vinculin 1 (antibody)
IA	Immunoaffinity
IgG	Immunoglobulin G
LC-MS	Liquid Chromatography-Mass Spectrometry
NA	Numerical Aperture
NC	Non-Contact (AFM)
NORM	Normal (condition)

NP	Nanopourous
NPA	No Preadsorption
NPTi	Nanopourous Titanium
OC	Osteocalcin
OSX	Osterix
PA	Preadsorption
PBS	Phosphate Buffered Saline
PDA	Polydopamine
PFA	Paraformaldehyde
PGA	poly(Glycolic) Acid
pH	Potential of Hydrogen
PI3K	Phosphoinositide 3-kinase
PLA	poly(Lactic Acid)
PTFE	Polytetrafluoroethylene
Rac1	Ras-related C3 botulinum toxin substrate 1
RhoA	Ras homolog gene family, member A
RMS	Root Mean Squared (roughness)
RNA	Ribonucleic Acid
rPDA	Rotationally Deposited PDA
RT-PCR	Reverse Transcriptase-Polymerase Chain Reaction
Runx2	Runt-related transcription factor 2
SA	Surface Area
$\mathbf{Si_3N_4}$	Silicon Nitride
SEM	Scanning Electron Microscopy
SIC	Serum Independent Component

sPDA	Statically Deposited PDA
STEPs	Stochastic, Transient Extension Periods
Ti	Titanium
TIC	Total Ion Current
TIRF	Total Internal Reflection Fluorescence microscopy
UHPLC	Ultra High Pressure Liquid Chromatography
VASP	Vasodilator-stimulated Phosphoprotein
VIN	Vinculin
XPS	X-Ray Photoelectron Spectroscopy

CHAPTER 1

Outline

1.1 Novelty and contribution

The motivation of this thesis research was to further the investigation into the mechanism of action and practical applications of PDA coatings. This was approached with two studies.

(1) In the first study, we first performed a physicochemical assessment of NPTi and NPTi+PDA surfaces. We determined that the surface was adequately generated and discovered little difference in preadsorption of serum proteins. I was able to confirm an enhancement in PDA-mediated bioactivity of MG-63 cells, namely the improvement of proliferation, spreading and focal adhesion development/maturation.

(2) In the second study, I was able to confirm the successful generation of unique PDA surfaces on borosilicate glass. Despite striking differences at a glance, we discovered surfaces were chemically similar. We utilized unique AFM technology to probe the nanometric physical characteristics of discrete structures on the surface and discovered that the two distinct structures, film and aggregate, are similar in all variables except for the fact it takes 5x more force and 18x more energy to detach from film. This introduces the novel concept of physico-structure heterogeneity on PDA surfaces which has not been previously determined.

Considering this heterogeneity, I analyzed the two surfaces with the major distinction being the topographical features and determined that the rPDA surfaces, with more globular films and increased density of larger aggregates, are superior in bioactive effects for hMSCs.

Finally, I wanted to determine whether the bioactivity of PDA is tied directly to its serum adsorption capabilities, as suggested in previous literature. Using hMSCs cultured in serum-free media seeded on surfaces with/without preadsorption of serum protein, I was able to confirm that there is in fact a serum independent component to PDA surfaces that play a significant role in cell spreading and less so, though still evident, in cell proliferation.

This research has generated the following journal papers and conference proceedings;

Journal Articles

1. **Steeves, A.***, Atwal, A.*, Schock, S. C. and Variola, F. ”Evaluation of the direct effects of poly(dopamine) on the *in vitro* response of human osteoblastic cells.” *Journal of Materials Chemistry B* **4**. (2016)
2. **Steeves, A.**, Variola, F. ”Method of deposition affects physicochemical, bioactive and serum-independent components of polydopamine coatings.” *in preparation*. (2018)
3. Ho, W., **Steeves, A.** and Variola, F. ”Cellular response to semi-ordered and biomimetic nanotubular surfaces.” *in preparation*. (2018)

Conference and Seminar Proceedings

1. **Steeves, A.**, Variola, F. ”Method of deposition affects physicochemical, bioactive and serum-independent components of polydopamine coatings (*Poster*)”, Canadian Biomaterials Society (CBS) 34th AGM, Vancouver, BC (May 2018)
2. **Steeves, A.**, Variola, F. Investigating the physicochemical and bioactive effects of polydopamine coatings on osteoblastic and stem cells (*Technical seminar*), uOttawa Centre for Catalysis Research and Innovation Seminar Series, Ottawa, ON (April 2018)
3. **Steeves, A.**, Vijay, M., Tieu, A., Yan, W., Xu, M., Daniels, B. and Variola, F. ”In vitro activity of pulsed water jet modified titanium (*Oral*), WJTA-IMCA Conference, New Orleans, LA (October 2017)
4. **Steeves, A.** and Variola, F. In vitro cellular response to bio-inspired surfaces (*Oral*), International Materials Research Congress (IMRC) 25th AGM, Cancun, Mexico, (August 2016)
5. **Steeves, A.**, Atwal, A., Schock, S. C. and Variola, F. Evaluation of mussel derived polymer as bioactive coating for titanium (*Poster*), 10th World Biomaterials Congress (WBC), Montreal, QC (May 2016)
6. **Steeves, A.**, Atwal, A. and Variola, F. Evaluation of mussel derived polymer as bioactive coating for titanium (*Poster*), Nano Ontario Annual Conference, Ottawa, ON (November 2015)

7. **Steeves, A.**, Atwal, A. and Variola, F. Osteoblastic response to mussel inspired polymeric coating of titanium (*Oral*), International Material Research Congress (IMRC) 24th AGM, Cancun, Mexico (August 2015)

8. **Steeves, A.**, Atwal, A. and Variola, F. Osteoblastic response to mussel-inspired polymeric coating of titanium (*Oral*), Canadian Biomaterials Society (CBS) 32nd AGM, Toronto, ON (May 2015)

1.2 Outline of the thesis

In Chapter 2, the background of polydopamine, cells and AFM is explained.

In Chapter 3, the materials and methods used throughout the two studies are explained.

In Chapter 4, the physicochemical and bioactive analysis of Ti, NPTi and NPTi+PDA is discussed. In the first part, a physicochemical examination is completed via a combination of SEM, AFM, Raman and FTIR. In the second part, a bioactivity analysis of MG-63 osteoblast-like cells on respective surfaces is completed through assessment of cell proliferation, spreading and focal adhesion generation at early and late timepoints.

In Chapter 5, the analysis of a unique antibacterial PDA surface generated through rotation is discussed. An exhaustive physicochemical analysis is completed with the use of SEM, contact angle goiniometry, non-contact and digitial pulsed force mode AFM and XPS. A novel differentiation of PDA features is revealed. Furthermore, a bioactivity analysis is completed comparing the unique rPDA surface to the classical PDA surface and highlights the advantages of rPDA in cell spreading, proliferation and focal adhesion generation. Following this, an assessment to determine whether a serum independent component of PDA exists is completed, consequently identifying that one exists and its determined effects on different cell processes.

In Chapter 6, concluding statements regarding the research in this thesis are presented.

CHAPTER 2

Introduction

The development of a synthetic micro- and nano-environment is a hallmark of modern tissue engineering with an emphasis on developing materials that interact and elicit a predictable and precise biological response. While these biomaterials are most often seen in modern medicine as metallics and ceramics, the use of versatile polymeric materials is a fast-growing research area with their ability to act as both a base-substrate and source of surface functionalization for other materials.

Recent focuses look at improving the control of the cell-substrate interface so as to not only enhance biocompatibility, expansion and differentiation, but also to retain key properties of multi-/pluri-potent cells pertinent for tissue engineering.[1][2] Polymers can vary in their structure with origins being either synthetic, including poly(lactic acid) (PLA) and polyglycolic acid (PGA), or natural, including collagen and fibronectin.[3] Naturally sourced polymers have the benefit of being biodegradable and intrinsically biologically active due to the endogenous incorporation of ligands that interact with cell receptors.

2.1 Polydopamine (PDA)

In the search for natural methods of beneficial functionalization for multiple classes of materials, inspiration was drawn from the adhesive proteins of mussels which were found to be largely comprised of lysine amino acids as well as 3,4-dihydroxy-l-phenylalinine (DOPA), the precursor to the neurotransmitter 3,4-dihydroxyphenethylamine (Dopamine, DA) (**Figure 2.1A-C**).[4] Subsequently, it was found that the spontaneous oxidative polymerization of dopamine in an alkaline solution was an effective method for the dip-coating of a variety of materials, including metallics and ceramics, resulting in a thin polydopamine (PDA) film on the surfaces (**Figure 2.1F-G**).[4] Since its discovery, PDA has been investigated in a variety of fields including energy, environmental and biomedical sectors. Namely in the biomedical field, PDA has been found to be a unique and versatile soft material that has been explored as a bioactive coating of a range of materials, as an effective drug encap-

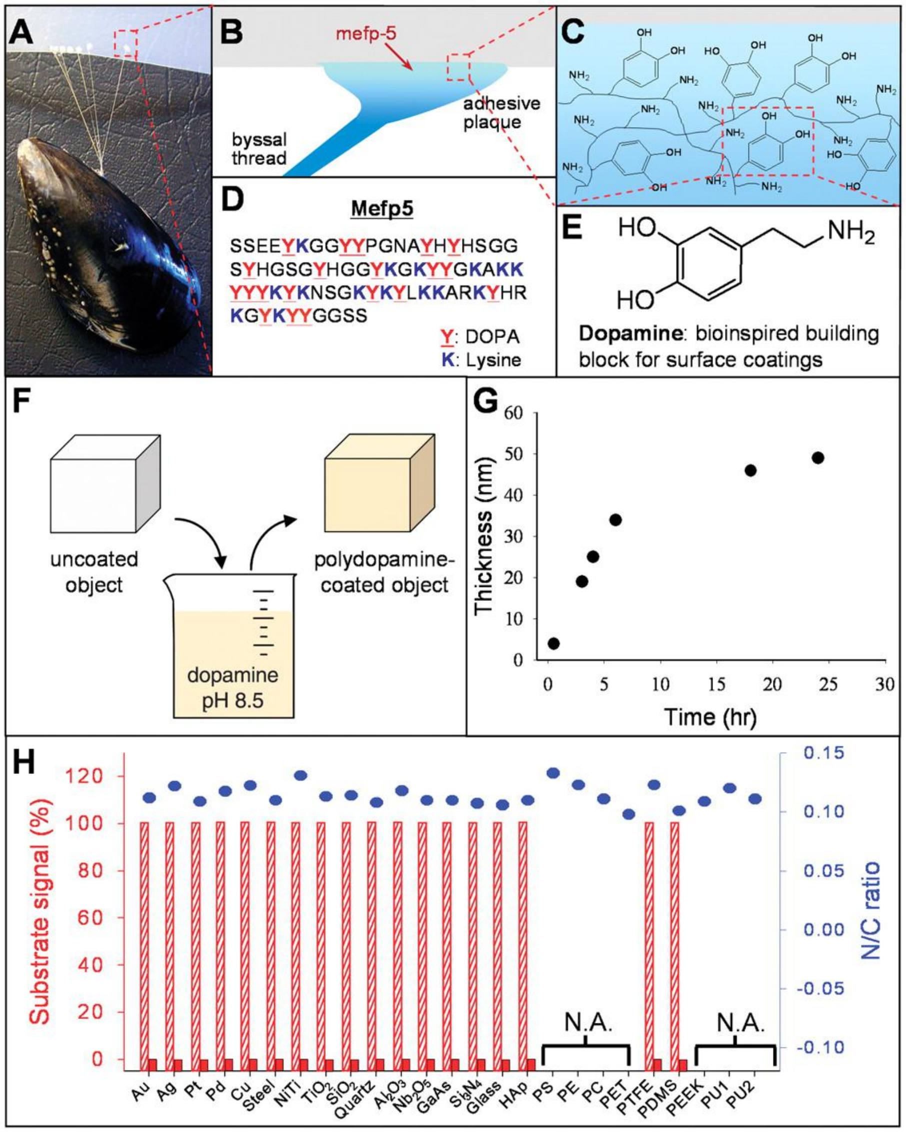

Fig. 2.1 Origin and coating procedure for PDA

(**A**) Photograph of a mussel attached to commercial PTFE. (**B** and **C**) Schematic illustrations of the interfacial location of Mefp-5 and a simplified molecular representation of characteristic amine and catechol groups. (**D**) The amino acid sequence of Mefp-5. (**E**) Dopamine contains both amine and catechol functional groups found in Mefp-5 and was used as a molecular building block for polymer coatings. (**F**) A schematic illustration of thin film deposition of PDA by dip-coating an object in an alkaline dopamine solution. (**G**) Thickness evolution of PDA coating on Si as measured by AFM of patterned surfaces. (**H**) XPS characterization of 25 different PDA-coated surfaces. The bar graph represents the intensity of characteristic substrate signal before (hatched) and after (solid) coating by PDA. The intensity of the unmodified substrate signal is in each case normalized to 100%. Substrates with characteristic XPS signals indistinguishable from the PDA signal are marked by N.A. The blue circles represent the N/C ratio after PDA coating.[4]

sulation medium and as a co-deposition partner for surface modification.[5][6][7][8]

2.1.1 Deposition

Since the discovery of simple deposition protocol of PDA using the autooxidation of Dopa HCl in an alkaline solution (e.g., Tris-HCl), much work has been committed to experimenting with differing methods and variables so as to be able to tune the resultant polymeric surface. Variables including pH, identity of buffer solution, oxidants, reactant concentrations and temperature have all been investigated and result in the generation of PDA surfaces and particles of different sizes, film thickness and chemical compositions.[9][10][11][12] In general, high pH, use of oxidants, increased concentrations of reactants and higher temperatures lead to films that are thicker, reactions that are quicker and aggregates that are larger. An additional variable to the deposition of PDA is the application of motion during the deposition process. The three variations are static, which is used in classical deposition, stirring, which is has been used to prevent particle deposition on the substrate, and shaking.[4][13] Recently, the method of shaking has been shown to resulting film has led to the remarkable enhancement in the contact-active antibacterial activity of PDA coatings for both gram-positive and gram-negative specimen.[14] These antibacterial surfaces, deposited while on a rotational platform and herein referred to as rotationally deposited PDA (rPDA), while those surfaces deposited on a static platform are referred to as statically deposited PDA (sPDA). In addition to the reported improvement in antibacterial properties, cursory investigation showed no adverse effects of rPDA on HeLa cell survivability.

2.1.2 Structure

Over a decade later since the first seminal publication on PDA, the structure and formation of PDA is still largely unresolved.[4][15] However, there is a consensus on the dissolved oxygen, such as that present in the alkaline Tris buffer, promoting auto-oxidative polymerization resulting in the intermittent presence one or more of dopamine, quinone and 5,6-dihydroxyindole (DHI) subunits (**Figure 2.2**).[16] Subsequent models conflict heavily and suggest radically different structures including the formation of non-covalent supramolecular or covalent hetero-/homo-polymers.[17][18][19]

2.1.3 Protein adsorption

Adsorption of sera protein on substrate is known to play a critical role in the ability for cells to detect and initially react to surfaces. Surface chemistry, topography and wettability have been shown to affect the complex time-dependent adsorption process through changes

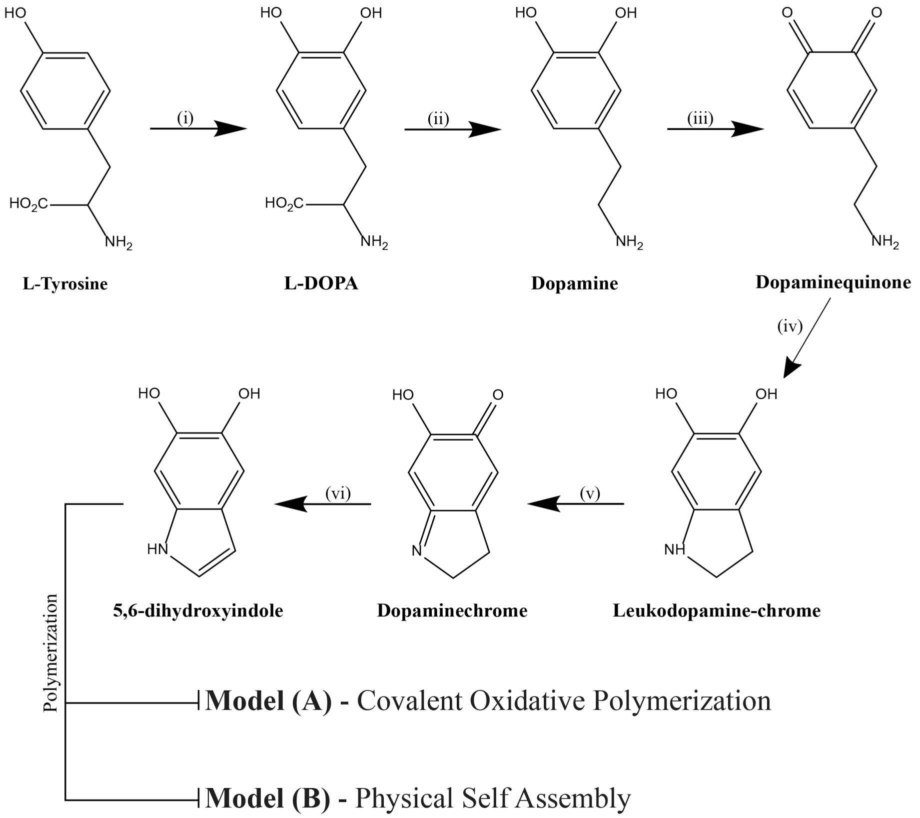

Fig. 2.2 Stepwise synthesis to produce 5,6-dihydroxyindole (DHI)

in kinetics, efficiency and conformational characteristics of adsorbed protein.[20][21] The ability of PDA to enhance adsorption of protein, with tunable kinetics, has been well established and investigated as a method of biofunctionalization for various substrate compositions and structures.[22][23][24] Native conformational stability has also been an indicated attribute of PDA and is supported by the retention of enzymatic catalytic activity of adsorbed enzymes, though this has not been fully explained and is unable to account for differential cell-specific responses.[25][4] However, such previous work is absent of comparison to pristine surfaces, characterization of the deposited PDA and as well does not discriminate for fundamental separation of protein preadsorption versus circulating serum. Recently, work in our lab investigated the effects of PDA deposition in the improvement of bioactivity on nanopourous titanium and found little difference in the most abundant serum proteins, measured via LC-MS, despite there being a considerable improvement in bioactivity.[26] Statistically significant differences in Apolipoprotein A-11 and $'beta$-2-glycoprotein were inconsistent are not believed to play a substantial effect on cellular response. As such, there is an indication that the benefits of PDA coatings extend beyond its ability to preadsorb and retain the conformation of protein, suggesting a serum independent component (SIC) responsible at least in part for PDAs bioactivity.

2.2 Cells

The choice of an effective cell model for the study of osteo-related research requires an assessment of the molecular, morphological and behavior of available lines. Many lines exist, with origins ranging from human (e.g., Saos-2) to mice (e.g., MC-3T3), and are frequently isolated from malignant osteosarcomas (bone tumors). However useful, cell lines isolated from osteosarcomas are limited by their abnormal molecular functioning which in turn affects the morphological and behavioral characteristics. As such, the two cell lines that were chosen was the MG-63 osteoblast-like line and bone marrow derived hMSCs.

2.2.1 MG-63 cells

For some time, osteo-based biological studies have utilized the osteoblast-like MG-63 cell line for experimental modelling. These fibroblast cells, isolated from the osteosarcoma of a 14-year-old male, are noted for their heterogeneity of mature and immature osteoblastic features with relatively low expression of the osteocalcin (OC) and bone sialoprotein (BSP) osteoblastic markers.[27] The limitless cell growth, ease of culturing and the congruity of integrin-subunits allow for simple cell-substrate studies due to their ability to regulate various functions in osteogenesis.[28] Taken together, the MG-63 line is comparatively found to be an optimal choice for osteoblast-like experimental modelling of biomaterials that interface with bone such as those with the potential to be used in orthopedic or periodontal implants.

2.2.2 Human mesenchymal stem cells (hMSCs)

Human mesenchymal stem cells (hMSCs) are extraordinary clonogenic cells that are noted for their ability for self-renewal, important in tissue development, and their multipotency, allowing them to differentiate into one of multiple lineages including osteoblasts, chrondocytes and adipocytes.[29] Since their discovery, a great deal of research has gone into discovering the mechanisms that direct hMSCs to differentiate and to generate relevant therapies and substrate.[30] To this end, researchers have sought for a better understanding of the stimuli that influence stem cells through investigation into stem-cell niche, which is the surrounding microenvironment to which hMSCs are found within the body and known to influence fate. These stem cell niches are composed of growth factors, chemical signals (e.g., chemokines) and ECM comopnents that provide physicochemical stimuli (e.g., stiffness, ligands).[31] This work has led to the extraordinary diverse array of potential mesenchymal stem therapies and include an optimistic outlook for ailments including myocardial infarction, cartilage repair and osteoarthritis.[32][33][34] In line with this, research field of interest is the development of biomaterial interfaces that assist in the stem cell proliferation and differentiation, including PDA.[30][4]

2.2.3 Cell structures

2.2.3.1 Actin cytoskeleton

The actin cytoskeleton is one of the three major structural elements in an eukaryotic cell, besides intermediate filaments and microtubules. Filamental actin consists of repeating subunits of right-helical actin monomers, termed globular actin (G-Actin). Growth and maintenance of F-Actin is achieved through tight regulation via nucleating factors (Arp2/3 complex) and associated polymerization proteins (e.g., profilin). Many critical cell functions, including cell division, motility and signaling depend on the actin cytoskeleton, and as such has been thoroughly researched to understand its importance in, and regulation of, its processes in varied cells and pathologies. Of the actin cytoskeletal elements, a major structure involved in cellular functioning, including environmental sensing, is the filopodia.

Filopodia Filopodia are thin, finger-like projections that protrude from the cell edge, most notably the lamellipodium, and enable cells to interact and probe their physicochemical surroundings. These structures possess specialized receptors as their tips and have been associated with a wide variety of cellular processes with the greatest association being their involvement in migratory-based functions including cellular migration, wound healing and cell-cell interaction. Integral to their ability to detect the physical environment, the spiral F-actin structure of filopodia interacting with myosin-V results in the transmission of force from the base of the structure.[35][36] These dynamics result in use of filopodia in cellular responses such as influence of migratory behavior which can be based on chemical cues, such as surface bound chemicals environmental (chemotaxis) or substrate bound chemoattractant (haptotaxis), and physical cues including substrate rigidity (durotaxis). Another structure related to filopodia are the nanoscale membrane projections, termed nanopodia, that have been found to provide the sensory information of features as small as 8 nm.[37]

Molecular regulation and response Molecular regulation of the actin cytoskeleton is achieved by GTPase proteins that possess a conserved switching mechanism with the activate state characterized by the binding of Guanine Triphosphate (GTP). These enzymes are involved in a series of cellular processes including proliferation, differentiation, signal transduction and cytoskeletal dynamics.[38] A well studied subfamily is the Rho family of small GTPases (21 kDa) that are characterized by their involvement in intracellular processes, including cell morphology, development and movement. The three most studied Rho GTPases are Rac1, Cdc42 and RhoA which are non-exclusively associated with lamellipodia, filopodia and stress fibers, respectively.

RhoA is a two switch region (I and II) GTPase involved in the regulation of cell cycle progression, actin organization and is also indicated in differentiation of stem cells to varied lineages. During the cell cycle, proliferative signals (e.g., growth factors) activate signal transduction pathways that result in RhoA activity, which downstream, elicits control through the maintenance of Cyclin D1 expression and stability via effector proteins.[39] To note, RhoA is key regulator of cell-substrate adhesions (i.e. focal adhesions) and as such is an important target in the investigation of cell-substrate mechanotransduction.[40] Differentiation into the osteogenic lineage is also indicated to be controlled by RhoA activity and is an upstream regulator of the signal cascade which results in Runx2 activation, a protein essential for osteoblastic differentiation.[41][42]

2.2.3.2 Focal adhesions

Components and Generation Cellular adhesion and interaction with underlying substrate is a complex process which requires the regulated dynamics of a host of intracellular and transmembrane proteins allowing for the transduction of external forces to the internal

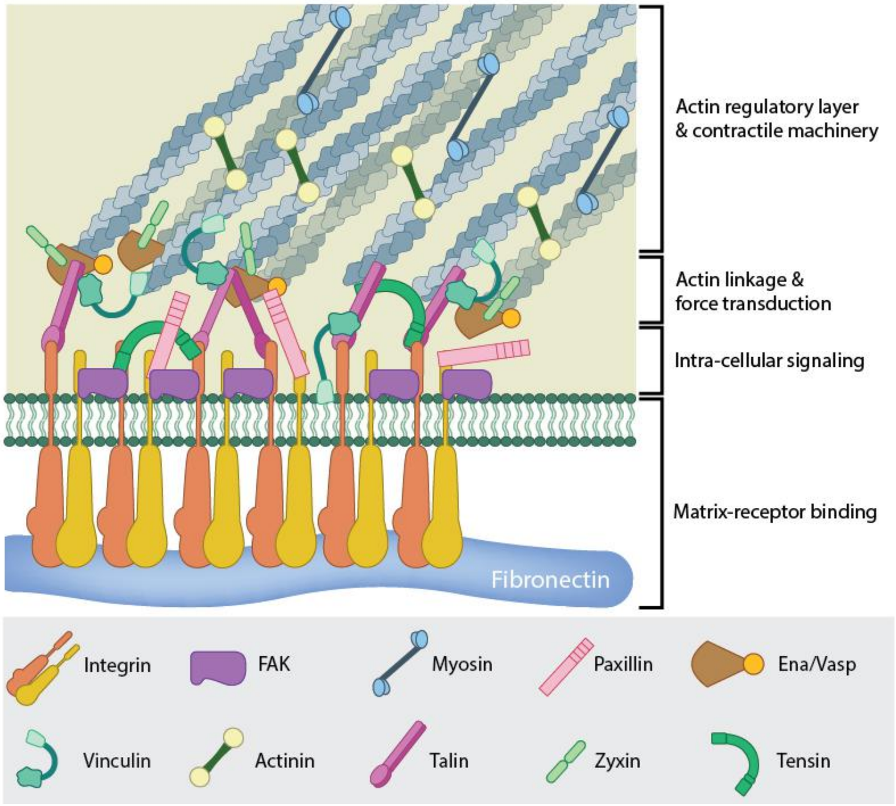

Fig. 2.3 Schematic representation of an focal adhesion

A mature FA contains hundreds of proteins that are grouped based on their contribution to four basic processes: receptor/matrix binding, linkage to actin cytoskeleton, intracellular signal transduction and actin polymerization. Both actin polymerization and acto-myosin contractile machinery generate forces that affect mechanosensitive proteins in the actin linking module, the receptor module (e.g. integrins), the signaling module and the actin polymerization module. The combined activity of the mechanosensitive components forms the mechanoresponsive network. Image courtesy of the Mechanobiology Institute, National University of Singapore.[54]

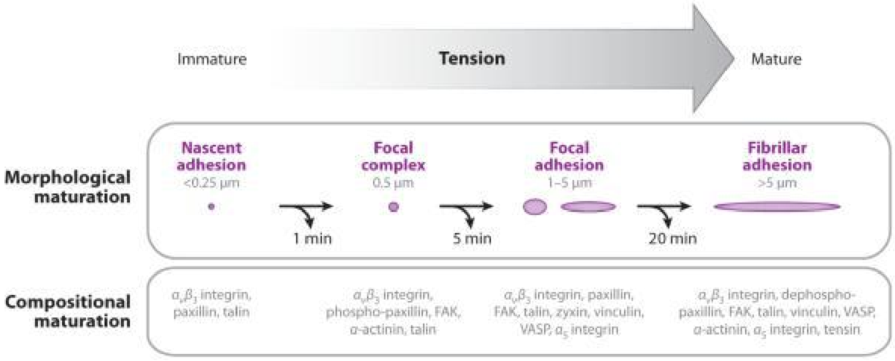

Fig. 2.4 Schematic diagram comparing the morphological phases of adhesion maturation

(**Above**) Adhesion represented by purple ovals; length scales indicated are focal adhesion lengths. (**Below**) Compositional phases of adhesion maturation with protein components. At each of these steps, adhesion turnover can occur (curved black arrows) after a certain amount of time (timescale below each arrow). FAK, focal adhesion kinase; VASP, vasodilator-stimulated phosphoprotein.[47]

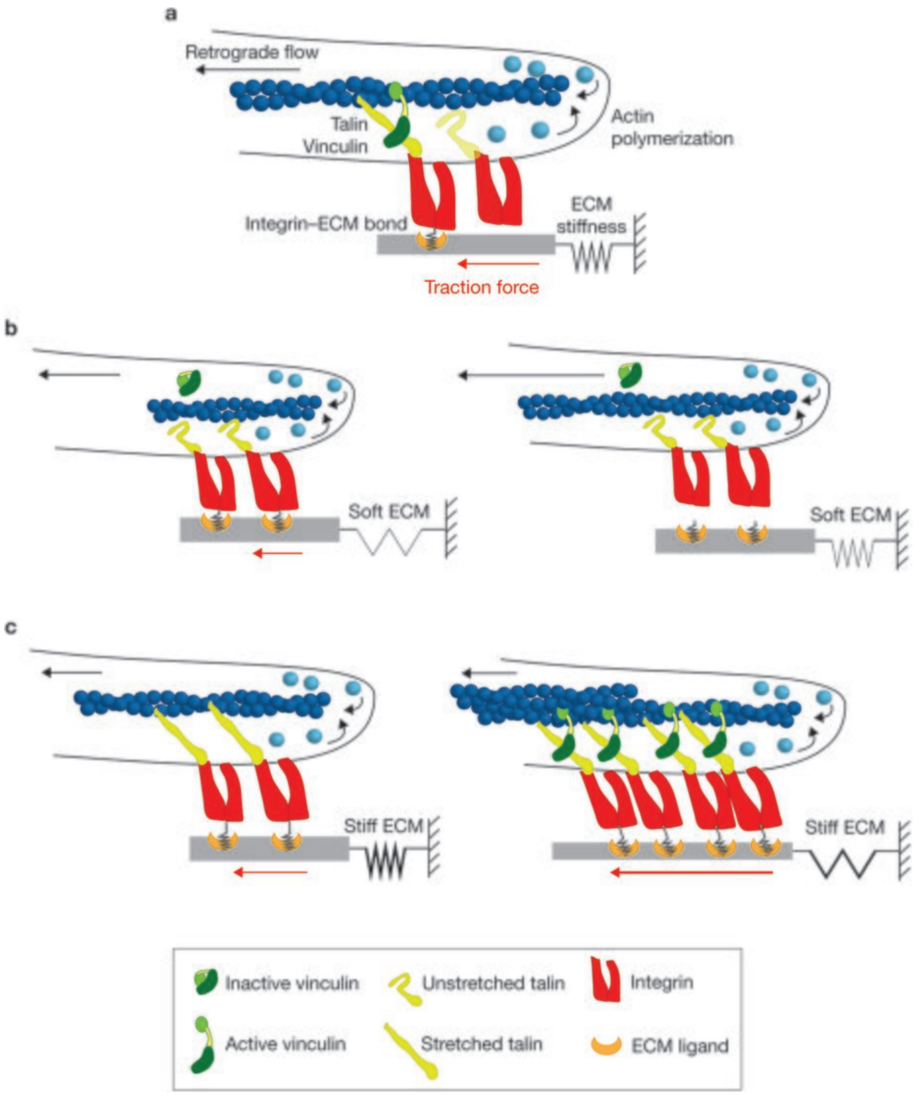

Fig. 2.5 The enhanced Roca-Cusachs molecular clutch model

(**A**) An overview of the mechanosensitive molecular clutch model, as proposed in the current study1. (**B**) On soft substrates, the rate of load transmission is slower than the integrin–ECM bond lifetime, resulting in bond dissociation before talin can unfold or vinculin can bind. (**c**) On stiff substrates, load is transmitted faster than the integrin–ECM bond lifetime, resulting in talin unfolding, vinculin binding and actin-mediated reinforcement.[55]

cell structure which are critical for a range of cellular processes include cell cycle and migration.[43] Integrin, an multimeric α-β dimer transmembrane protein composed of a large extracellular domain and short cytoplasmic tail, is crucial in initial interaction between a cell and substrate.[44] External ligand binding to integrin is hypothesized to result in substantial allosteric changes that transmit to the intracellular domain, subsequently inducing recruitment of adaptor and signaling proteins that promote the clustering and crosslinking of integrin.[45][46] Subsequent integrin clustering results in the recruitment of a swarm of proteins involved in the transduction of mechanical forces into intracellular signaling cascades involving the anchoring to the actin cytoskeleton (**Figure 2.3**). Early cell-matrix contacts form small nascent focal complexes ($\sim$0.5 μm in length) that may be strengthened and matured into larger focal adhesions ($\sim$1-5 μm in length) and further into fibrillar adhesions ($>$5 μm in length) that are specific to fibronectin adhesion (**Figure 2.4**).[47] Maturation from focal complexes to adhesions are the result of the integrin-actin molecular clutch linkages in line with the Roca-Cusachs molecular clutch model (**Figure 2.5**).[48][49] In this model, the stiffness of the substrate results in resistive force which applies a load on the integrin-ECM bonds which have a finite lifetime. Stiff substrates result in a quicker transmission of this load via these integrin-ECM bonds which in turn induces the unfolding of the adapter protein talin into an active conformation, subsequently enabling associated protein and actin association and reinforcement. Conversly, soft substrate are unable to transmit this force in an adequate amount of time and so the integrin-ECM bonds are unable to be reinforced before dissociating.[50] Vinculin (VIN), one of the many components of multimeric focal adhesion complex, plays a critical role in the transduction of cell-substrate mechanical forces as both a protein cross-linker and force transducer. Under mechanical stress, vinculin's active open conformation works to maintain the active open conformation of talin which in turn promotes the linking of talin to actin filaments, a process critical in focal complex strengthening into mature adhesions.[51] Application of load on vinculin, whether by stiffer substrate or succeeding traction forces, has been shown to reduce vinculin turnover which has been shown to be critical for directional migration though unnecessary for random migration.[52] The stability and strengthening of adhesions by vinculin has shown to be crucial for the maintenance of adhesion strength with VIN knockdown models resulting in a 30% loss of adhesion strength with the remainder associated with integrin binding and clustering.[53] Consequently, the role of vinculin in FA formation, maturation and dynamics makes it an ideal target for the visualization of cell-substrate adhesion sites at both the scale of focal complexes and adhesions.

Dynamics in Cellular Processes Cellular adhesion to the extracellular matrix play critical roles in a range of biological processes including proliferation, cell spreading and migration. Focal adhesion formation and subsequent induction of FAK/RhoA is hypothesized to directly promote proliferation through a topography-dependent modulation.[56][57] During the initial stages of cell spreading, integrin-containing filopodial projections are present around the periphery of a cell and are crucial in the initial cell-ECM interaction and subsequent cell spreading.[58] These projection produce the initiation of cell-substrate adhesions that result in lengthening of the filopodia, associated with accumulation of additional integrin and focal adhesion components, resulting in swelling of these projections into nascent focal complexes and subsequently into focal adhesions.[58] Subsequent focal adhesions formed around the periphery of the plasma membrane have shown to be highly dependent on the spacing of integrin ligands, exemplified by the differential evidence of spreading with productive tethers on nanopatterns of 8 nm Au particles spaced 108 nm apart, versus patterns with 58 nm spacings.[59] These 108 nm spacings were also found to be critical during cellular migration and dynamic behavior. Curiously, recent studies have shown that in 3D substrate, confinement is sufficient for cell-substrate interaction and enables the cell to proceed with focal adhesion independent cell migration.[60]

2.2.3.3 Substrate effects on cell spreading and migration

Local and bulk interfacial characteristics, including stiffness and topography, can directly affect the activation of integrin-ECM binding groups which play a role in spreading and motility.[61][62] The differential activation of these transmembrane mechanotransductive complexes will in turn modulate several characteristics of the kinetic spreading process including velocity and predominance and behavior of morphological structures (e.g., filopodia).[63] Another influenced variable is the initiation of spreading after initial cell-substrate adherence, which will lead to the transition from the spherical to circular morphologies which represent uninitiated and initiated spreading, respectively.[64] Once initiated, cells will undergo a fast period of quick isotropic spreading, represented herein by circular morphology, and is characterized with lower centripetal actin flow indicative of low projection formation (**Figure 2.6D-F**).[65] Following this, the cells undergo anisotropic spreading through a sequence of ”stochastic, transient extension periods” (STEPs) that results in high centripetal actin flow due to peripheral projection formation and velocity and is represented herein by the protrusive morphology (**Figure 2.6A-C**).[65]

The probing of chemical cues by filopodia have been found to be critical for cellular processes including migration with subsequent cell-specific effects including differentiation. Two primary forms of chemical cue sensing resulting in migration are based on

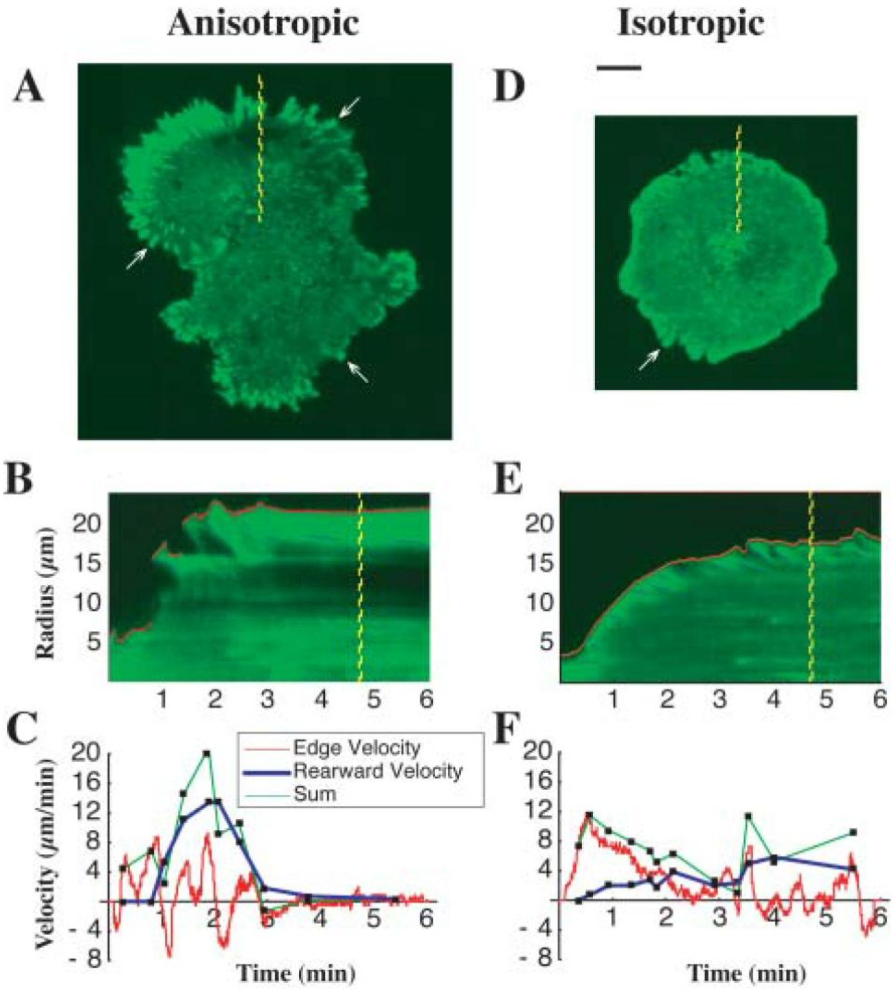

Fig. 2.6 Isotropic and anisotropic spreading of cells

Low actin rearward movement in isotropic spreading cells. Time-lapse TIRF microscopy of the spreading of transiently transfected GFP -actinin-labeled cells revealed further information regarding the nature of the difference between anisotropic (**A-C**) and isotropic (**D-F**) cells. As an indicator of focal contacts, -actinin labeling shows that in anisotropic spreading cells (A, arrows), focal contacts matured more quickly than in isotropic cells (**D**, arrow). GFP -actinin is also used as an indicator of the rearward movement of the actin cytoskeleton. Using kymographs (time-space plots in which the spatial axis is perpendicular to the cell's edge) of fluorescent time-lapse sequences for both anisotropic (**B**) and isotropic (**E**) cells, we computed the velocity of the rearward movement of -actinin, the edge velocity, and the sum of the two in anisotropic spreading (**C**) and isotropic spreading (**F**). Rearward movement in anisotropic cells (**C**, blue curve) was much higher at early times compared to that of isotropic spreading cells (**F**, blue curve).[65]

either detection of environmental chemicals (chemotaxis) or substrate bound chemoattractant (haptotaxis) and are enabled by the presence of specific cell surface receptors.[66] Absent of an environmental chemical gradient, stochastic pseudopodial protrusions extend throughout the periphery and are integral for haptotaxis.[67] When a gradient is detected through the activation of a ligand-receptor pathways (e.g., endothelial growth factor [EGF]-EGFR), drive the activity of the Arp2/3 complex which catalyzes F-actin polymerization forming additional pseudopodia and resultant lamellipodia.[68]

Physical attributes of substrate are well known to play significant roles in filopodial generation and cell dynamics which can result in modulation of cellular functioning. As filopodia are critical for the initial and prolonged sensing of the substrate, control of these properties can allow for the modulation of cellular response in the development of next generation biomaterials and to provide a valid model for the study of diseases. Topographical characteristics, as small as 8 nm, are detected by cells and have been shown to elicit affects in filopodial generation and dynamics.[37] Increased porosity and surface roughness is associated with preferential adhesion, filopodial generation and migration.[69][70] The size of features, whether as nanoislands/pillars, nanotube arrays or pores, have been critically linked to the response of a variety of cells, however these dimensions are indicated to be structure specific (e.g., width, height, angle) and there is no one size fits all rule.[71] Investigation into another aspect of these features, orderedness, has shown that increasing disorder and large structures negatively influences projection extension and behavior possibly due to the entrapment of projections in the larger asperities.[72] Numerous physical properties, including substrate rigidity and compliance, have been correlated to responses at the single-cell and tissue levels thereby playing roles in individual migration and wound healing, respectively. Durotaxis, migration resulting from rigidity sensing, is facilitated by nascent filopodial protrusions that have been shown to apply a myosin-II dependent force when probing the surround area.[73] Consequently, the rigidity of the surface has been shown to effective guide the motility with cell-specific preferences for optimal migration.[62] The stiffness of the substrate can also critically induce hMSCs toward specific lineages with soft ($<$1 kPa), medium (8-17 kPa) and hard (25-40 kPa) directing these multipotent cells towards become neurons, muscles and osteobalsts, respectively.[74] Curiously, recent work by Venugopal et al. (2018) has shown that the seeding density of hMSCs can supersede the substrate stiffness effects on morphology and proliferation where higher density seeding on soft substrates can present with more numerous mature focal adhesions and higher proliferation rates similar to that seen when seeded in lower density on a stiff substrate such as glass.

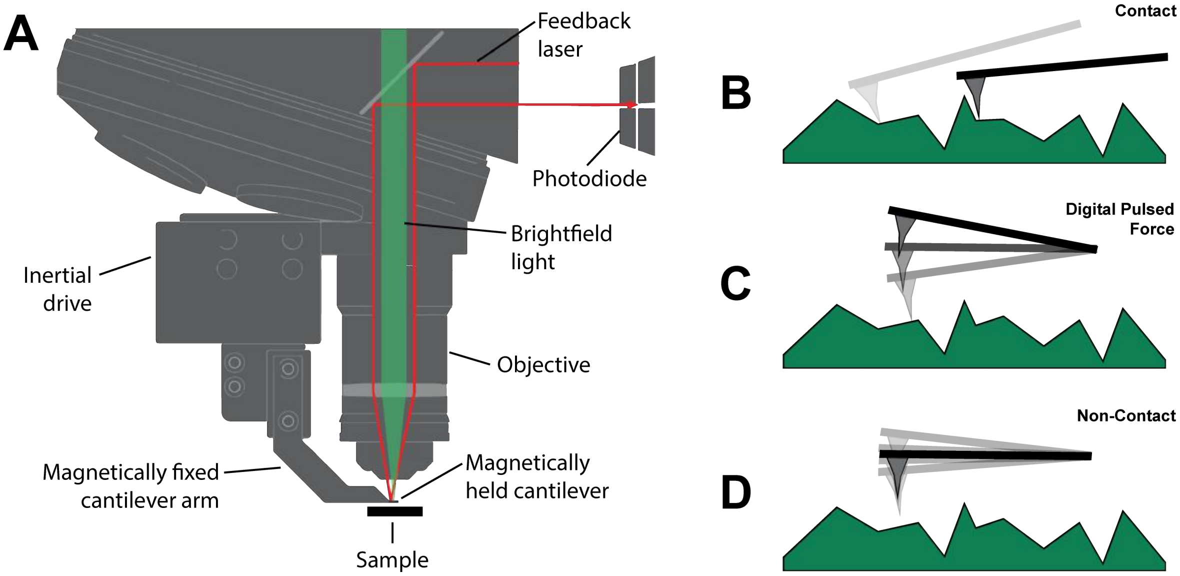

Fig. 2.7 AFM setup and available modes

(A) Schematic of the optical paths for the photodiode laser and standard objective. **(B-D)** Available modes with the WITec alphaRSA 300.

2.3 Atomic force microscopy (AFM)

AFM is a unique super resolution method of scanning probe microscopy (SPM) that generates physicochemical data from the direct and indirect interaction with the target surface. In our lab, the WITec alpha300 RSA is an upright oriented system with both the light path of the incident photodiode laser and primary objective being fixed above the sample (**Figure 2.7A**) allowing for imaging of both transparent and opaque surfaces. The system is capable of Contact, Non-Contact (NC) and Digital Pulsed Force Mode (DPFM) techniques. Contact mode involves scanning with the tip in direct contact with the surface at a predetermined setpoint voltage (**Figure 2.7B**) with topography changes causing deflections in the cantilever that are measured at the photodiode. Non-Contact mode involves the AC-driven oscillation of the cantilever 50 to 150 Å above the surface with Van der Waals forces between the tip and surface dampening or shifting the phase of the oscillatory movement which is then detected at the photodiode (**Figure 2.7C**). Digital Pulsed Force Mode (DPFM) involves the intermittent contact of the tip and surface as it is driven in a sinusoidal waveform throughout the scan, in essence creating a raster image with each pixel being a force-distance curve (**Figure 2.7D**).

2.3.1 DPFM theory and analysis

2.3.1.1 Background

As previously mentioned, DPFM-AFM is a technique involving the intermittent contact of a tip as it is driven with a sinusoidal modulation (**Figure 2.8A**), which allows for the measuring a variety of substrate mechanical properties. When the tip comes to a critical distance from the surface, the recorded waveform is modulated at various points throughout the cycle (**Figure 2.8B**). Similar to force-distance curves, a snap-in to initial contact can be detected with the shape of the following ascension being indicative of the material stiffness. The peak of this curve represents the maximum force (F_{max}) to the substrate. Following this, the tip begins its retraction from the surface though is still in contact until the force of adhesion (F_{ad}) is reached and detachment occurs. The resulting waveform is the free cantilever oscillations which undergo dampening with respect to the adhesion between the tip-surface as well as the spring constant (k) of the cantilever, until baseline is reached. Windows across specific portions of the cycle (**Figure 2.8C**) can be used to produce contrast images as seen in **Figure 2.8D-F** for stiffness (Panel D), topography (Panel E), adhesion (Panel F) and F_{max} (not shown).

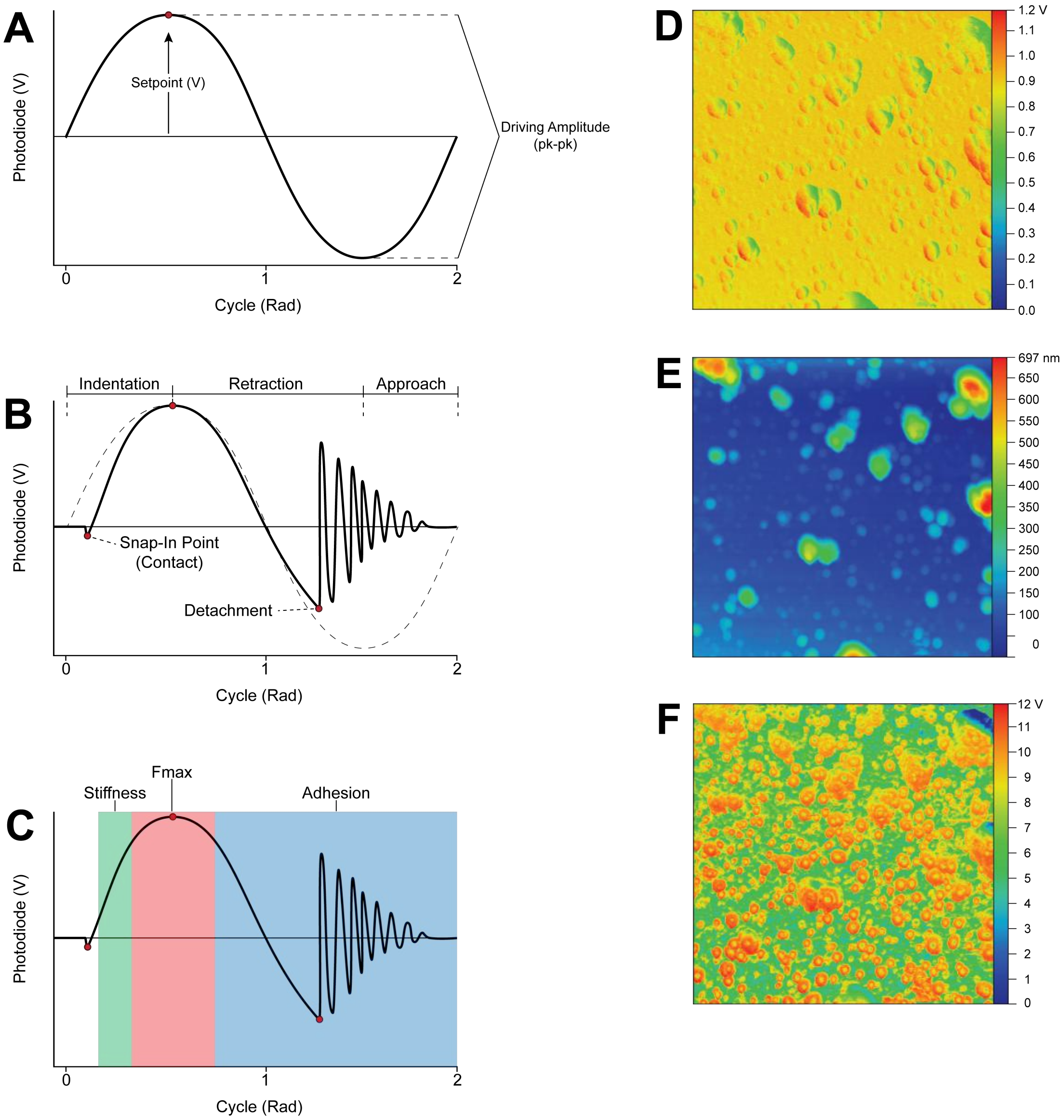

Fig. 2.8 Digitial Pulsed Force Mode (DPFM) imaging theory

(A-C) Sequence of visualization of DPFM curves, their critical characteristics and typical windows selected during imaging. **(D-F)** Examples of contrast maps from typical windows representing stiffness, topography and adhesion, respectively.

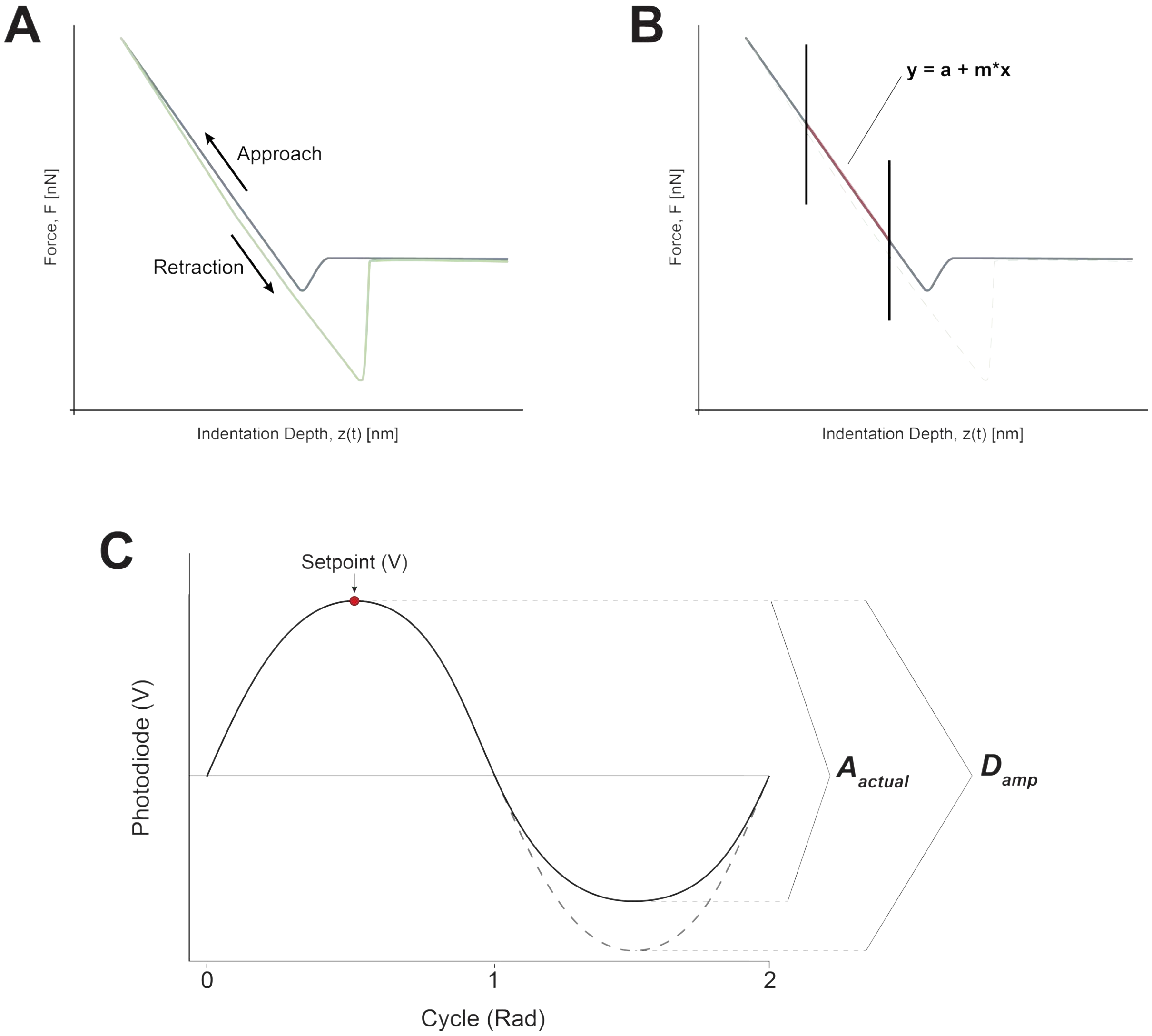

Fig. 2.9 Example of measuring sensitivity and modulation factor

(**A**) A standard force-distance curve acquired from nanoindentation of a sample. (**B**) Determining the sensitivity [S] of the system. Linear regression of the linear portion of the approach curve will generate the slope [m]. The reciprocal of the slope (1/m) is the sensitivity. (**C**) Determining the modulation factor [U]. At multiple driving amplitudes [D_{amp}], measure the ratio between the measured peak-peak distance over D_{amp}.

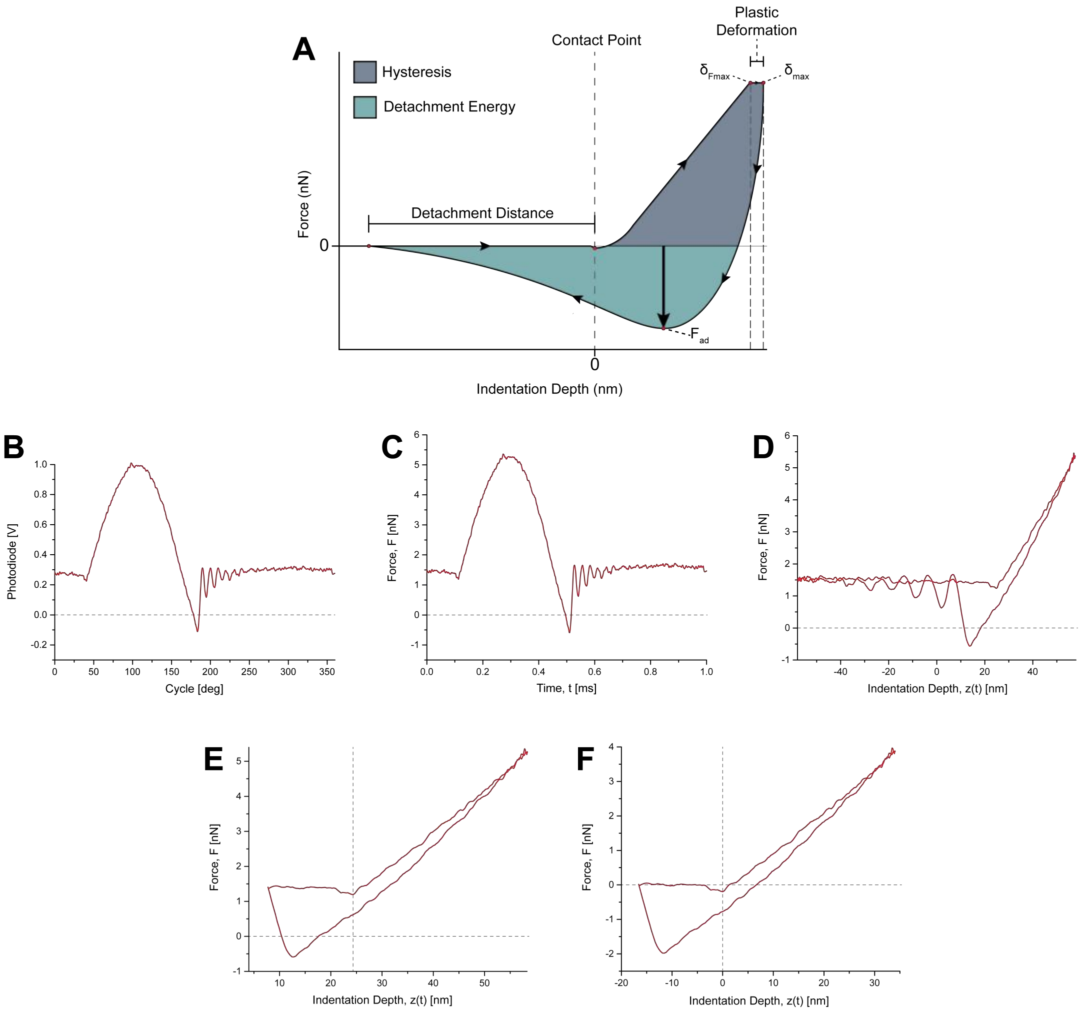

Fig. 2.10 Step-wise analysis of DPFM curves for determination of mechanical properties

(A) The ideal outcome of the curve analysis with critical variables identified. **(B-F)** The series of transformations to transform a DPFM curve into a force-indentation curve for analysis.

2.3.1.2 Curve conversion

Through the following series of transformations, a $Cycle\,[Rad] - V_P\,[V]$ DPFM curve can be converted into a $Force\,[nN] - Indentation\,[nm]$ curve which contains a wealth of information that can provide insight in the mechanical properties of the substrate as represented in **Figure 2.10A**.

1. **Measuring of the tip sensitivity** (S). This is to determine the offset between measured voltage and position through the linear regression of the indentation portion of a force-distance curve of the tip on a hard surface (e.g., Si) as represented in **Figure 2.9B** using **Equation 2.1**.

   $$S = \frac{V_P}{d} \tag{2.1}$$

   where V_P is the measured voltage from the photodiode, and d is the displacement

2. **Calculating the average modulation factor** (U). The modulation factor is the ratio offset between the actual peak-peak amplitude of the sinusoidal modulation (A_{actual}) over the applied peak-peak driving amplitude (D_{amp}), can be done with **Equation 2.2** and with visual reference in **Figure 2.9B**.

   $$U = \frac{A_{actual}}{D_{amp}} \tag{2.2}$$

3. **The conversion of the** $Cycle\,[Rad] - V_P\,[V]$ **to a** $Force\,[F] - Time\,[t]$ (**Figure 2.10C**). Since our frequency is 1 kHz, each cycle is completed in 1 ms and so the x-axis (2 Rad or 360 degrees) can be normalized between 0-1 ms thus giving t. The applied force (F) can be determined by calculating the product of the tip sensitivity (S), cantilever spring constant (k) and measured voltage from the photodiode (V_P) as represented in **Equation 2.3**.

   $$F = S * k * V_P \tag{2.3}$$

4. **Conversion of** $Force\,[F] - Time\,[t]$ **to** $Force\,[F] - Indentation\,[z(t), nm]$ (**Figure 2.10D**). This can be accomplished with **Equation 2.4**, with the indentation depth

($z[t]$) calculated using the sensitivity (S), modulation factor (U), driving amplitude (D_{amp}), drive frequency (v), time (t), and the phase (Φ). Phase is initially calculated from the DPFM of a hard surface (e.g., Si) and calculating $z(t)$ in such a way that the Φ leads to a total reduction of the hysteresis in the curve. As such, any hysteresis observed in the subsequent curves from the sample surface will be a true representation of its mechanical property and not a result of the tip-AFM system.

$$z(t) = SUD_{amp} * cos(2\pi vt + \Phi) \tag{2.4}$$

5. **Baseline and contact point correction** (**Figure 2.10E-F**). Residual signal from cantilever dampening is no longer required so data after the crossing of the baseline after detachment can be removed (Panel E). Using the lead-in ahead of the snap-in position, the baseline can be estimated and should be scaled to 0 accordingly along the Y-axis. The snap-in position should be scaled to 0 along the X-axis. The resulting graph (Panel F) can now be processed to assess the mechanical properties.

2.3.2 Mechanical properties assessed

Once DPFM curves have been converted to that seen in Figure **2.10A**, extraction of a series of parameters can be performed with a list of these stated in **Table 2.1**.[75] Stiffness of the substrate can be calculated by measuring the reciprocal slope of the approach, similar to the determination of sensitivity. Hysteresis is the area under the curve, above baseline. Detachment energy is the area under the curve, below the baseline. Hardness (H) can be calculated with **Equation 2.5** and compliance (D) is calculated with **Equation 2.6**

$$H = \frac{F_{max}}{A} \tag{2.5}$$

where H is the hardness, F_{max} is the maximum force applied, and A is the contact area projected at the surface

$$D = \frac{F_{max}}{\delta_{max}} \tag{2.6}$$

where D is the compliance, F_{max} is the maximum force applied, and δ_{max} is the maximum indentation

Table 2.1 List of parameters that can be extracted from processed DPFM curves

Parameter	Typical units
Snap-in position	nm
Maximum force	nN
Stiffness	N / m
Remnant depth	Nm
Indentation at maximum force	(δ_{Fmax}) / nm
Maximum indentation	(δ_{max}) / nm
Hysteresis	10^{-15} J
Hardness	GPa
Compliance	N / m
Adhesion force	nN
Detachment distance	Nm
Detachment energy	10^{-15} J
Young's modulus	GPa

CHAPTER 3

Materials and Methods

3.1 Preamble

This section contains the combined materials and methods of both studies due to the degree of repetition in some of the techniques used. Shared information is contained under the section with study specific information under subsections. A summary of the techniques used per study is shown in **Table 3.1**.

3.2 Sample preparation

Substrates (i.e. grade 2 titanium and standard glass slides) were immersed in a freshly prepared 2 mg/mL solution of Dopamine HCl (Sigma-Aldrich, H8502) in study specific concentrations of Tris-HCl (pH=8.6, Sigma-Aldrich, No T6664) for 24 hrs. Study 1 used 10 mM Tris-HCl to coincide with previously reported methods [76] while Study 2 used 25 mM Tris-HCl to match with the previously reported antibacterial surface [14]. Samples were then washed three times in deionized water (DI) and dried at room temperature (RT). Prior to use in cell culture, samples were sterilized in 70% ethanol (EtOH).

3.2.1 *"Evaluation of the direct effects..."*

Commercial grade 2 titanium disks (12 mm in diameter, 1 mm in thickness) were polished by two-step mechanical process by the supplier (Firmetal Co., Ltd, China). Discs were immersed in toluene in an ultrasonic bath for 20 minutes, washed three times in DI and once in 70% EtOH prior to being dried at RT. A portion of these discs were kept as the **Control** (**Ti**) condition. The remainder were immersed in "Piranha Solution", a 1:1 solution of H_2SO_4 (37N, Fisher Scientific):H_2O_2 (30%, Fisher Scientific) at RT on a stir plate for 2 hrs in order to generate nanoporous surfaces. Samples were removed and washed three times with DI, 70% EtOH and dried at RT. A portion of these disks were used as the **Nanoporous Titanium** (**NPTi**) condition. The remainder of the chemically treated disks were coated with polydopamine (PDA) using the aforementioned *static* method (i.e., static PDA solution with no stirring) to generate the **PDA coated NPTi** (**NPTi+PDA**) condition (**Figure 3.1A**).

3.2.2 *"Method of deposition affects..."*

12mm borosilicate glass coverslips (#1.5, Fisher, 1254580) were ultrasonically cleaned with toluene and rinsed three times in DI. Coverslips were divided into three batches for different surface preparations over 24 hrs. Batch 1 was immersed in 1x-PBS and kept as the **Control** (**CTRL**) condition. Batch 2 and 3 were both immersed in the Dopamine solution (**Figure 3.1B**). Batch 2 was left in static position during deposition thus creating the **Statically Deposited PDA** (**sPDA**) condition. Batch 3 was put on a rotation platform (200 rpm) during deposition, resulting in the **Rotationally Deposited PDA** (**rPDA**) condition, as first described by Su et al. (2016). During deposition, rPDA samples were placed on a Styrofoam surface to prevent reported heat effects generated from the long-term electromechanical use of the shaker platform. Surfaces were then incubated overnight in one of three solutions related to the preadsorption of sera protein to the surface. Conditions for **normal culturing** (**NORM**) were incubated in 1x-PBS, conditions **without preadsorption** (**NPA**) were incubated in serum-free culture media and those conditions **with preadsorption** (**PA**) were incubated in culture media containing 10% FBS. Culturing media is further described in **Section 3.10**.

3.3 Scanning electron microscopy (SEM)

SEM imaging was accomplished with a JSM-7500F Field Emission Scanning Electron Microscope (FESEM, JOEL, Japan). The primary purpose was to ensure the effective nanopatterning of NPTi samples prior to deposition as well as to give initial visualization of all PDA deposited surfaces. In addition, cell-substrate interaction was also studied.

3.4 Atomic force microscopy (AFM)

Imaging of both PDA coated and bare substrates were carried out with the AFM module of the alpha300 RSA (WITec, Germany) system.

3.4.1 *"Evaluation of the direct effects..."*

Images were obtained by using the DPFM mode and rectangular Si_3N_4 Cantilever B of a multi-tip MLCT chip (Bruker). This cantilever is characterized by a tetrahedral tip with

Table 3.1 Summary of the techniques used in each study

Technique	Evaluation of the direct effects of poly(dopamine) on the *in vitro* response of human osteoblastic cells	Method of deposition affects physicochemical, bioactive and serum-independent components of polydopamine coatings
Sample preparation	✓	✓
Scanning electron microscopy	✓	✓
Non-contact AFM	✗	✓
Digital pulsed force mode AFM	✓	✓
Contact angle goniometry	✗	✓
X-ray photoelectron spectroscopy	✗	✓
Raman spectroscopy	✓	✗
Attenuated total reflectance Fourier transform infrared spectroscopy	✓	✗
Liquid chromatography mass spectroscopy	✓	✗
MG-63 cell culture	✓	✗
Human mesenchymal stem cell culture	✗	✓
Reverse transcriptase / polymerase chain reaction assay	✓	✗

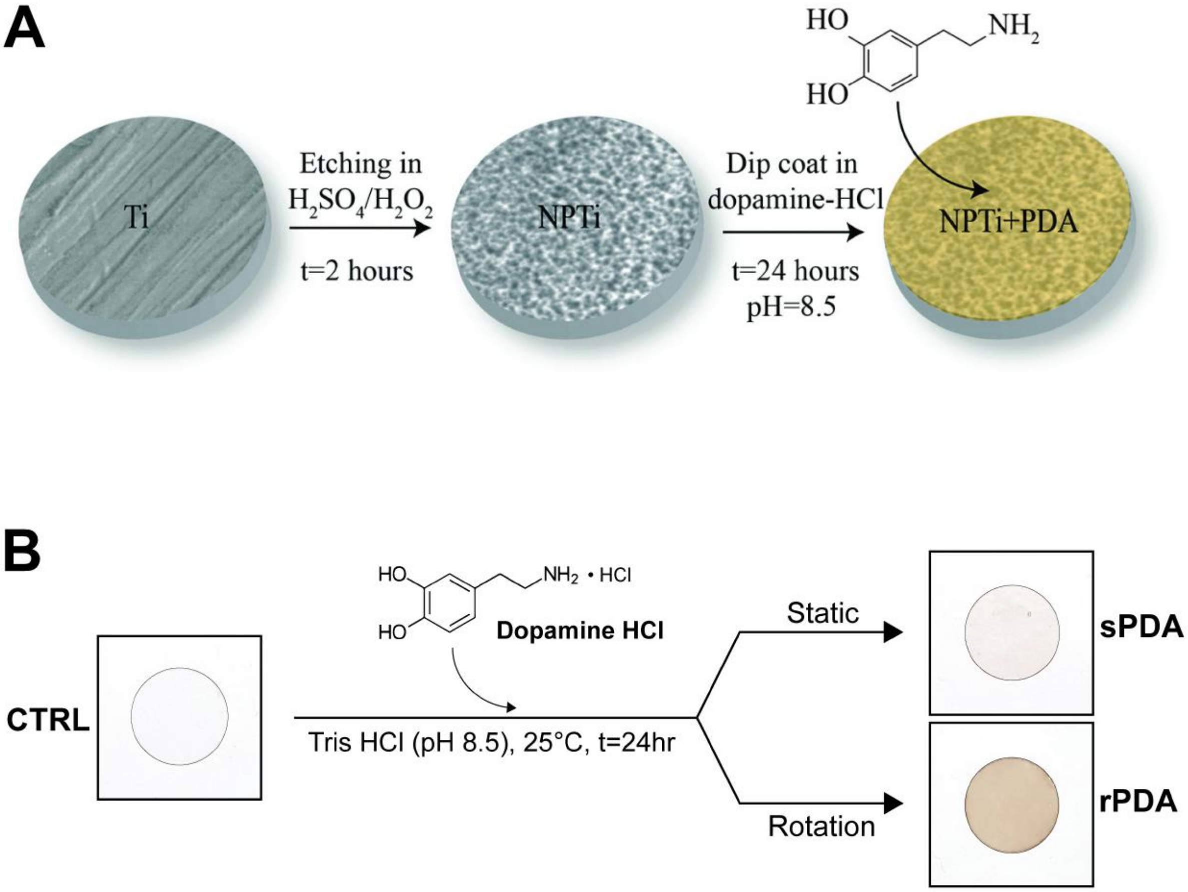

Fig. 3.1 Sample preparation with PDA deposition

Schematics of sample preparation. (**A**) Study 1 sample preparation to produce Control Untreated Titanium (Ti), Nanopourous Titanium (NPTi) and NPTi coated with PDA (NPTi+PDA) conditions. (**B**) Study 2 sample preparation to produce Control Borosilicate Glass (CTRL), Statically Deposited PDA (sPDA) and Rotationally Deposited PDA (rPDA).

a nominal radius of 20 nm, resonant frequency of 15 kHz and spring constant of 0.02 Nm^{-1}. Each DPFM image contains 2.5 x 10^5 force-distance curves, which were converted into $Force\,[nN]-Indentation\,[nm]$ data according to literature.[75] 40 randomly selected curves were analyzed for stiffness and further fitted with the Hertzian model to determine the Young's modulus.

3.4.2 *"Method of deposition affects..."*

Larger scale imaging for topography and mechanical properties was done in DPFM mode. The tip used was the triangular Si_3N_4 Cantilever C of the DNP-S chip (Bruker). This tip is characterized by a rotated pyramidal tip with a nominal radius of 10 nm, spring constant of 0.24 Nm^{-1} and nominal frequency of 56 kHz. Each 6 x 6 μm image provides 2.6 x 10^5 force distance curves. 40 curves were selected between the aggregates and thin-film in a relative proportion and analyzed for various mechanical properties. The Derjaguin Muller Toporov (DMT) model was used to determine the Young's modulus due to its inclusion of adhesive forces in the model.

Inter-aggregate imaging was done using the NC-mode as it provided additional clarity as to the underlying film due to the sensitivity of the technique. The rectangular cantilever of the RFESPA-40 chip (Bruker) was used and has a tip characterized by a rotated pyramidal tip with a nominal radius of 8 nm, resonant frequency of 40 kHz and spring constant of 0.9 Nm^{-1}.

3.5 Contact angle measurements

The water contact angle was measured with a VCA Optima Surface Analysis System (AST Products Inc.) after samples were washed and vacuum dried for 16 hrs. A drop of DI (1 μl) was ejected from a micro syringe (Hamilton Company), picture taken and a manual outline of key points of the droplet was performed to ensure accuracy prior to automated measurement of the angle. Three droplets were measured per samples and performed in triplicate.

3.6 X-Ray photoelectron spectroscopy (XPS)

The surface chemistry of deposited PDA surfaces was acquired by the XSAM-800 X-ray Photoelectron Spectroscope (XPS) with the assistance of Dr. Sander Mommers at the University of Ottawa Centre for Catalysis Research Institute (CCRI). A wide-scan survey spectrum was recorded to visualize the elemental composition of the surface which was further analyzed with CasaXPS software (CASA Software Ltd.). Investigation was performed in the 279-291 eV, 389-407 eV and 522-540 eV regions representing Carbon ($C\ 1s$), Oxygen ($O\ 1s$) and Nitrogen ($N\ 1s$). Curve fitting for specific chemical groups was done through OriginPro (Origin Labs Inc.) with insight into signals from literature.[77]

3.7 Raman spectroscopy

Raman spectroscopy, for the chemical mapping of the samples to ensure polymer deposition, was acquired with the Raman module of the alpha300 RSA system. 20 x 20 μm Raman maps were collected through a 100x Objective (EC Epliplan NEOFLUAR, N.A.=0.9, Zeiss) at high resolution (150 x 150) with excitation by a 524 nm doubled Nd:YAG Laser (9.5 mW, acquisition time=0.1s). Analysis of Raman bands in the 250-3000 cm^-1 region was analyzed with Project 4 PLUS (WITec) and OriginPro for the presence of PDA chemical signatures, in line with previous literature.[78][79]

3.8 Attenuated total reflectance Fourier transform infrared (ATR-FTIR) spectroscopy

Spectroscopic information was analyzed in the 1100-1800 cm^{-1} range as an indication for the presence of PDA, with signals in the 1500-1600 cm^{-1} range attributed to N-H vibrations, in the 1500-1700 cm^{-1} range attributed to C=C stretching and in the 1690-1740 cm^{-1} range attributed to C=O stretching.

3.8.1 *”Evaluation of the direct effects...”*

To confirm protein adsorption, Ti, NPTi and NPTi+PDA disks were immersed in 1x-PBS, serum-free media (αMEM) or complete culture media (αMEM + 10% FBS) for time intervals of 6 hrs and 3 days. Culturing media is further explained in **Section 3.10**. Samples were washed three times with deionized H_2O, dried under vacuum and analyzed by a Bruker Tensor 37 FTIR spectrometer (Bruker) equipped with a (RT)DLaTGS detector and a platinum ATR accessory with a 2 mm single reflection diamond crystal. Spectra were measured in randomly selected areas of each sample, performed in triplicate, with a resolution of 4 cm^{-1} and 256 acquisitions per spectrum.

3.9 In-solution digestion and liquid chromatography mass spectroscopy (LC-MS)

3.9.1 Digestion

In parallel, four samples per condition were immersed in the complete culture medium for LC-MS spectroscopy. After 6 hrs, samples were removed from the solution, rinsed thoroughly in DI and placed in a sterile 24-well plate. 200 μl of 8 M urea (Invitrogen) were added in each well and incubated for 15 min with moderate shaking. Successively, 200 μl of DTT (Fisher Scientific) in 100 mM ABC (BioUltra) were added into each well to bring the final concentration of DTT at 10 mM, and incubated at RT for 1 hour. 200 μl of IA (GE Healthcare) in 100 mM ABC was then added into each well to make the final concentration of IA at 55 mM, and incubated at RT in the dark for 1 hour. The alkylation reaction was quenched with 5 mM DTT in 100 mM ABC solution.

200 μl of MS grade trypsin (Pierce)/100 mM ABC solution with concentration of 1 ng μl^{-1} were added into each well and incubated at 37^oC overnight. Digestion was stopped by adding 5 μl of 5% formic acid (Fisher Scientific) into each well. The content of each well was transferred into a 1.5 mL Eppendorf tube, and the volume of liquid in each vile was reduced to 20 mL by using the SpeedVac. Five samples per condition were combined into 1 tube. Experiments were carried out in quadruplicates to ensure statistical significance. Samples were finally cleaned by 10 μl C18 tips according to manufacturer's protocol (Pierce), lyophilized with SpeedVac and re-suspended in 10 μl 0.1% formic acid for LCMS/MS analysis.

3.9.2 LC-MS

LC-MS measurements were carried out by using an Orbitrap Fusion mass spectrometer (Thermo Scientific) equipped with an Ultimate 3000 UHPLC (Thermo Scientific), a PepSwift monolithic pre-concentration column (Thermo Scientific) and an Acclaim PepMap C18 analytical column (Thermo Scientific).

The mobile phase for HPLC separation was composed of 2 components: buffer A and B. Buffer A was 0.1% formic acid in water and buffer B was composed of 0.1% formic acid, 90% acetonitrile and 9.9% water. 5 μl of sample was loaded onto the pre-concentration column with the loading pump flow rate set at 3 μl min^{-1}. The nano pump flow rate was set at 0.3 μl min^{-1}. Mobile phase B started at 2% at the beginning of the run and increased to 4% at 7 min. Then it increased to 13.5% at 32 min, 24.5% at 60 min, 33.5% at 70 min, followed by 5 min wash at 80% B. The column was re-equilibrated for 20 min at 2% B.

The peptides eluted from the analytical column were ionized by electrospray by a Thermo Scientific Nanospray Flex ion source and analyzed by the Thermo Orbitrap Fusion mass spectrometer. The full MS scan was performed by the Orbitrap and the resolution was set at 60 K and AGC target set at 2 x 10^5 with maximum injection time 50 ms. The MS/MS were done in the ion trap with the following filters in effect: (1) monoisotopic precursor selection was turned on; (2) intensity threshold was set at 5 x 10^3; (3) charge states 26; (4) dynamic exclusion 35 s. The MS/MS was performed at data dependent mode under Top Speed setting, meaning the instrument will maximize the MS/MS scans based on the cycle time and the frequency of the full scans. Peptide fragmentation activation mode was CID and the collision energy was set at 35%. The AGC target was set at 1 x 10^4 and maximum injection time was 35 ms.

3.10 Cell culture

3.10.1 *"Evaluation of the direct effects..."*

MG-63 human osteosarcoma cells (ATCC, CRL-1427) were grown with αMEM + 4.5 g/L glucose, L-glutamine (Corning, 10-010-CM) supplemented with 10% FBS (ThermoFisher, 12483020), 20 $U\ ml^{-1}$ penicillin and 20 $U\ ml^{-1}$ streptomycin (ThermoFisher, 15140122) in a 5% CO_2 water jacketed incubator at 37^{o}C. Cells were detached from surfaces using appropriate volumes of 0.25% trypsin-EDTA (ThermoFisher, 25200072) and incubating at 37^oC for 5 minutes. Cells were collected and centrifuged at 190g for 8 minutes, supernatant discarded and pellet reconstituted in fresh culture media to desired concentrations specific to the experiment to a total volume of 500 μl per well. Incubation periods thereafter were dependent on each experiment in question.

3.10.2 *"Method of deposition affects..."*

Bone marrow derived hMSCs (RoosterBio, MSC-001) were expanded using the High Performance Media (RoosterBio, KT-001), aliquoted and frozen down. Aliquots were thawed and initially cultured in High Performance Media in order to take advantage of its low FBS, high nutrient and growth factor nature to allow for better recovery of cells. Once confluent, further passaging and experiments were completed with DMEM + 4.5 g/L glucose, L-glutamine supplemented with 10% FBS, 20 Uml^{-1}, penicillin and 20 Uml^{-1} streptomycin in a 5% CO_2 water jacketed incubator at 37^{o}C. Cells were detached from surfaces using appropriate volumes of 1x TrypLE Express (ThermoFisher, 12604021) and incubating at 37^{o}C for 5 minutes. TrypLE was chosen as it contains a singular enzyme, versus a complex, which subsequently reduces unexpected cleaving. To ensure the complete neutrilization of the trypsin enzyme, 50 $\mu g/mL$ Soybean Trypsin Inhibitor (Sigma-Aldrich, 10109886001) was used and added for 5 minutes. Cells were collected and centrifuged at 190g for 8 minutes, supernatant discarded and pellet reconstituted in fresh culture media to desired concentrations specific to the experiment, approximately 20,000 cells/ml, to a total volume of 500 μl per well. Incubation periods thereafter were dependent on each experiment in question.

Samples prepared for immunofluorescence were fixed with freshly prepared RT 4%-PFA (Sigma-Aldrich, 158127) for 10 minutes, washed with 1x-PBS and further processed. Samples prepared for SEM imaging were fixed after 24 hrs with a mixture of 1$\%$ glutaraldehyde (Grade 1, Sigma-Aldrich, G7526), 4$\%$ paraformaldehyde mix for 1 hr at RT. Samples were washed with deionized H_2O then subjected to a six-step dehydration series in EtOH from 50$\%$ to 100$\%$. To reduce charging effects of the organic PDA film and cells, samples were coated using a Q105R Rotary-Pumped Sputterer (Quorum, Canada) prior to imaging.

3.11 Immunofluorescence

3.11.1 Acquisition

After cells were incubated for experimental intervals, cells were fixed with RT 4%-PFA for 10 minutes, washed with 1x-PBS and permeabilized with 0.25% Triton-X100 for another 10 minutes. Nuclei were stained with NucBlue ReadyProbes (Thermofisher, R37605) and the actin cytoskeleton was stained via Rhodamine conjugated Phalloidin (ThermoFisher, R415). To visualize the focal adhesions, we targeted Vinculin with a 1:400 mouse monoclonal Anti-hVIN1 (Sigma-Aldrich, V9131) as the primary antibody and 1:600 Goat anti-Mouse IgG conjugated to Alexafluor 488 (ThermoFisher, A-11001) as the secondary antibody.

Multi-channel images were captured with an AxioObserver.Z1 inverted microscope (Zeiss, Germany) fitted with the Zeiss Filter Set 49 (Hoechst), Chroma Filter Set 49002 (GFP) and Chroma Filter Set 49005 (Rhodamine). Low-magnification tiles of the surfaces were imaged with a 10x A-Plan (Ph2) Objective (NA=0.25, Zeiss) for assessment of cell proliferation. Mid-magnification tiles of the surfaces were imaged with a 20x Plan-Apo (Ph2, DIC II) Objective (NA=0.8, Zeiss) for assessment of general morphology and cell spreading. High-magnification tiles of the surface were imaged with a 40x Plan-Apo Corr. (DIC III) Objective (NA=0.95, Zeiss) for high resolution imaging of focal adhesions and cell structure.

3.11.2 Analysis

Image collections were stitched together with AxioVision Mosaix Software (Zeiss) and focus stacked with ImageJ (NIH). These files were then run through custom pipelines in CellProfiler 3.0.[80] Quantification of focal adhesions were achieved using a custom macro in ImageJ that performed background subtraction, thresholding and particle analysis. All data was aggregated and statistical analysis performed in OriginPro.

3.11.3 CellProfiler

For the measurement of cell morphology, characteristics and proliferation, multiple custom pipelines were produced in CellProfiler which were constantly calibrated for the images to ensure quality control of results. Four main measurements were scrutinized for the cell structure which are cell area, perimeter, form factor and compactness. Cell area was calculated by counting the number of pixels within the identified cells. Perimeter was calculated by measuring the number of pixels around the boundary of the identified cell periphery. Form factor is a representation of the irregularity of the cell shape, measured with Equation 3.1, with perfectly circular objects having a calculated value $=1$. Compactness is calculated as the mean squared distance of the object's pixels from the centroid divided by the area with a whole circle having a value $=1$ and irregular objects with a value >1.

$$F = \frac{4 * \pi * A}{P^2} \tag{3.1}$$

where A is the area, and P is the perimeter

3.12 Reverse transcriptase / polymerase chain reaction (RT-PCR) assay

After incubation on their respective surfaces for 24 hrs, 1 mL TRIzol (ThermoFisher, 15596026) was added to the samples for five minutes at RT and then transferred to centrifuge tubes. Chloroform was then added, vigorously vortexed and centrifuged (12 000g, 10 minutes, 4^oC). The aqueous phase was mixed with isopropyl alcohol, incubated at RT for 10 minutes and centrifuged. The pellet was dissolved in DNAse/RNAse free water and protein concentration measured. Total RNA ($2\mu g$) was subjected to RT for 60 minutes at 42^oC using 200 units $SuperScript^{TM}$ and First Strand Buffer (Invitrogen, 18080044) in the presence of 0.5 $\mu g\ \mu l^{-1}$ oligo dT, 10 mM DTT and 1 mM dNTP mix, in the presence of 10 μM of each specific primer and 2.5 units of Taq DNA polymerase (NEB, M0273X). Amplifications were performed in an Eppendorf thermocycler (Brinkmann). Each sample was run in triplicate. cDNA was also amplified with RhoA primers (sense 5'-CCA GTT CCC AGA GGT GTA TGT-3'; antisense 5'-CCT GTT TGC CAT ATC TCT GCC-3') and GAPDH primers (sense 5'-CAT GGC CTT CCG TGT TCC TAC CC-3'; antisense 5'-CCT CGG CCG CCT GCT TAC-3') as a positive control. 10 μl aliquots of PCR products were size-separated by electrophoresis on a 1-2% agarose gel. Experiments were repeated in triplicate.

CHAPTER 4

Evaluation of the direct effects of poly(dopamine) on the *in vitro* response of human osteoblastic cells

4.1 Preamble

The research presented in this chapter was accepted for publication in the Journal of Materials Chemistry B on April 12th, 2016.[26]

4.1.1 Motivation

Characteristics of titanium and its alloys make it an ideal candidate for orthopaedic and periodontal implants. Advantages include its increased strength, lower weight, superior fatigue resistance and biocompatibility. Contributing to its biocompatability and subsequent osseointegration, the surface energy and microstructure of titanium has been affected through means including the use of Piranha solution to create a nanopourous surface (NPTi) that further enhances bioactivity. Biofunctional polymeric substrate are commonly studied and whose generation and inspiration can often be found in nature. Polydopamine (PDA), a bioactive polymer discovered when investigating the adhesive capability of *Mytilus edulis* mussels, has growing interest due to its bioactive capabilities. It is yet known whether the bioactivity of nanopourous titanium can be further strengthened by use of PDA as a coating. Characterizing the physicochemical and bioactive components of this combination can provide insight into, and evidence for, the use of this polymer in treatments for future implants.

4.1.2 Hypothesis and objectives

The main objective of this study was to characterize and determine whether the addition of PDA to NPTi will create a surface with enhanced bioactivity when tested with human bone-like cells (MG-63, osteosarcoma). Given the previously recorded bioactive advantages of the individual components, we postulated that NPTi + PDA surface would surpass that of NPTi alone. In addition we sought to gain a better understanding of the mechanism behind the activity of generated surfaces where we believed it may be at least in part to the enhancement of sera protein adsorption.

4.2 Abstract

Functional polymeric coatings have rapidly become one of the most efficient strategies to endow biomaterials with enhanced bioactive properties. Among the bio-inspired polymers used for biomedical applications, mussel-derived PDA has increasingly attracted considerable interest because of its unique characteristics. In this work, we carried out detailed physicochemical characterization of a PDA film deposited on nanoporous titanium. In particular, we employed spectroscopic techniques (Raman and ATR-FTIR) and Digital Pulsed Force Mode Atomic Force microscopy (DPFM-AFM) to probe the chemical makeup and the nanomechanical properties of PDA-coated surfaces. In addition, we investigated protein adsorption by ATR-FTIR and quantified it with ten different serum proteins by Liquid Chromatography Mass spectroscopy (LC-MS), aiming at elucidating their potential contribution to the subsequent cell colonization. Successively, we assessed the response of MG-63 human osteoblastic cells to PDA-coated titanium both the multiple- and single-cell levels. Results for this study demonstrate that, compared to bare and nanoporous titanium, the PDA coating positively influences the adhesion and proliferation of MG-63 cells. In addition, we focus on how the three different substrates influence cell morphology (i.e. aspect ratio and form factor), the establishment of focal adhesions and the expression of RhoA, a protein involved in cell contractility. In conclusion, our work provides a deeper insight on the in vitro response of human osteoblastic cells to poly(dopamine) by closing in on specific aspects of cell-PDA interactions, ultimately reaffirming the potential of this bio-inspired polymer as a functional coating for bone tissue engineering applications.

4.3 Results and discussion

4.3.1 Structural analysis

In agreement with previous work, while polished controls did not exhibit any reproducible features at the nanoscale, nanoporous surfaces showed the characteristic 3-dimensional network of nanometric pits (image not shown, the reader can refer to references [81][82][83] for details). In the case of PDA-coated nanoporous titanium, SEM and AFM analysis revealed the distinctive granular appearance that typifies deposited films of PDA (**Figure 4.1A** and **B**).[77] High resolution (5 x 5 μm^2) AFM imaging and line scans (**Figure 4.1C**) permitted to close in on the 3-dimensional structure of the granular features, which resulted to be 95 ± 11 nm in width and 22 ± 6 nm in height. The average dimension of these elements is significantly larger than that previously reported for PDA films deposited via dip coating process on gold (in the 25-30 nm range in diameter).[77] However, the granular features we report are similar in size to those resulting from a multiple dip cycles deposition ($>$100 nm).[84] This may be ascribed to the longer deposition used for this study (24 hours), a factor that could have permitted the growth of the granular features with time.[77]

By exploiting the DPFM capabilities of the AFM, we generated stiffness maps by assigning a color code to the cantilever's deflection when indenting the sample's surface (**Figure 4.1D**). The average stiffness of the poly(dopamine) coating resulted to be 0.24 ± 0.06 Nm^{-1}. This value is similar to the stiffness of rubbery polymeric films, such as styrene-butadiene copolymers (0.23 Nm^{-1}).[85] DPFM data also permitted to quantify the Young's modulus. Every point of a DPFM map can in fact be converted into a force-distance curve from which the value of the elastic modulus can be extracted. In particular, the PDA coating exhibited an average Young's modulus of 92 ± 17 MPa. The comparison of our results with the existing literature was not unequivocal because of the variability in the published results. For example, a previous study which employed the AFM to determine the elastic modulus of poly(dopamine) films deposited on a gold substrate reported a value of 12.1 ± 1.6 MPa.[86] Conversely, a PDA coating of mica was shown to exhibit an elastic modulus of 870 MPa.[87] The inconsistencies between our results and previous literature may originate from different assumptions used in the contact mechanics models, the adhesion strength between the substrate and the polymeric layer,[88] as well as from the different parameters used to deposit the PDA coating (which, in turn, may affect its physical properties), all factors which may have influenced the AFM-based nanoindentation measurements.

4.3.2 Physicochemical analysis

In order to probe the physicochemical characteristics of the PDA coating and its ability to retain serum proteins, we exploited Raman (**Figure 4.2**) and infrared (**Figure 4.3**) spectroscopy.

In the case of Raman analysis, while the Ti and NPTi disks did not show any significant band in the 250-3000 cm^1 range (indicative of a mainly amorphous outer TiO_2 layer),[81][83] spectra collected on NPTi + PDA samples were characterized by two peaks at 1350 and 1580 cm^1, attributed to C=O catechol stretching vibrations (**Figure 4.2A**).[25] [89] The Raman signature of the dopamine molecule was successively used to map out the chemical composition of NPTi + PDA samples to ensure that the deposited films were

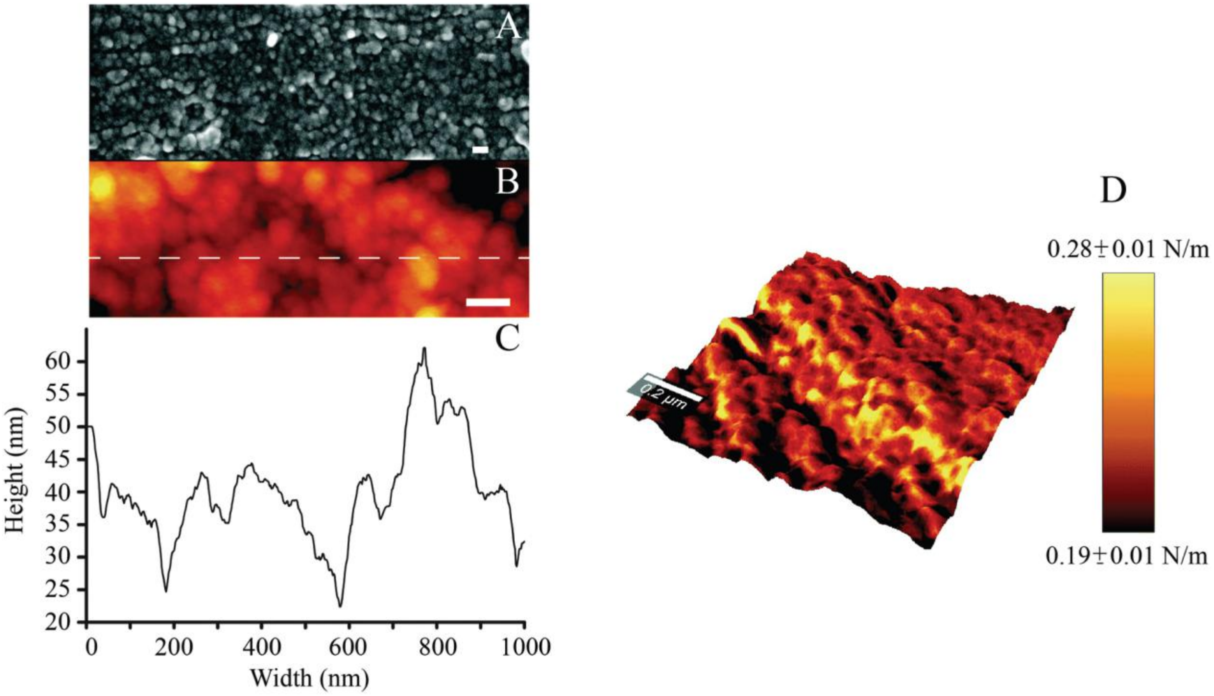

Fig. 4.1 SEM and AFM imaging

(**A**) SEM and (**B**) AFM images of the PDA coating (scale bar = 100 nm). (**C**) AFM line scan. (**D**) DPFM-AFM image showing the topography with stiffness overlay for the PDA coating.

homogeneously distributed on the surface of the disks. **Figure 4.2B** displays a representative Raman map (superimposed to the corresponding AFM topographical image) which demonstrates the presence of a continuous PDA surface film. However, localized variations in the band intensity were detected, and although minimal (**Figure 4.2B**, intensity scale), they may nonetheless suggest the presence of distinct domains in the PDA film in the 600-2000 nm range in diameter, therefore larger than the individual granular features detected by AFM. Because of the different spatial resolution of AFM (1 nm)[90] and Raman imaging (diffraction-limited spatial resolution of about 300 nm for a 524 nm laser with a 100 objective),[91] we were not able to unequivocally correlate these domains to the surface distribution of the granular features resolved by the AFM. However, we can infer that such contrast in Raman images may derive from localized variations in the film's thickness, most likely resulting from microtopographical alterations (e.g. polishing marks) of the underlying titanium surface and/or from the deposition of PDA aggregates from solution.[92]

A previous study determined that FTIR spectroscopy of native (Ti) and modified (NPTi) titanium permits to probe the characteristics (i.e. thickness and crystallinity) of the surface oxide layer by considering the characteristics IR bands in the 600-1000 cm^1 interval which result from the Ti-O stretching vibrations.[93] At larger wavenumbers, Ti (data not shown, the reader can refer to reference [81]) and NPTi samples did not display distinctive absorption bands (**Figure 4.3A**). Conversely, NPTi + PDA disks revealed the characteristic infrared signature of poly(dopamine), featuring absorption bands at 1210 cm^1 (O-H bending in the catechol group), 1260 cm^1 (C-O stretching in the catechol group), 1510 cm^1 (N-H scissoring) and 1600 cm^1 (C=C stretching in the aromatic ring) (**Figure 4.3B**).[77][79] Together with the Raman analysis, these results confirm that the PDA film was successfully deposited across the surface of nanoporous titanium samples.[94]

ATR-FTIR was successively employed to investigate protein adsorption on surfaces. Cellular processes on surfaces are believed to be affected by an adlayer of proteins adsorbed from bodily fluids prior to cell colonization.[94][95] Therefore, investigating the distinctive capacity of surfaces to retain proteins may contribute to understand the differential cellular response observed on the three conditions tested. In order to reproduce the in vitro conditions of cell cultures, we immersed Ti, NPTi and NPTi + PDA samples in a solution of 10% FBS in α-MEM for 6 hours and 3 days, thereby considering a large number of proteins at once without any biological bias. Noteworthy, although the selected intervals considerably exceed the time required for proteins to adsorb (in a timeframe of seconds to minutes),[94] such a choice permitted us to obtain a snapshot of the surface adlayer presented to cells between the adhesion and the growth phase.

The infrared spectrum of α-MEM (**Figure 4.3C**, dotted line) and FBS (**Figure 4.3C**,

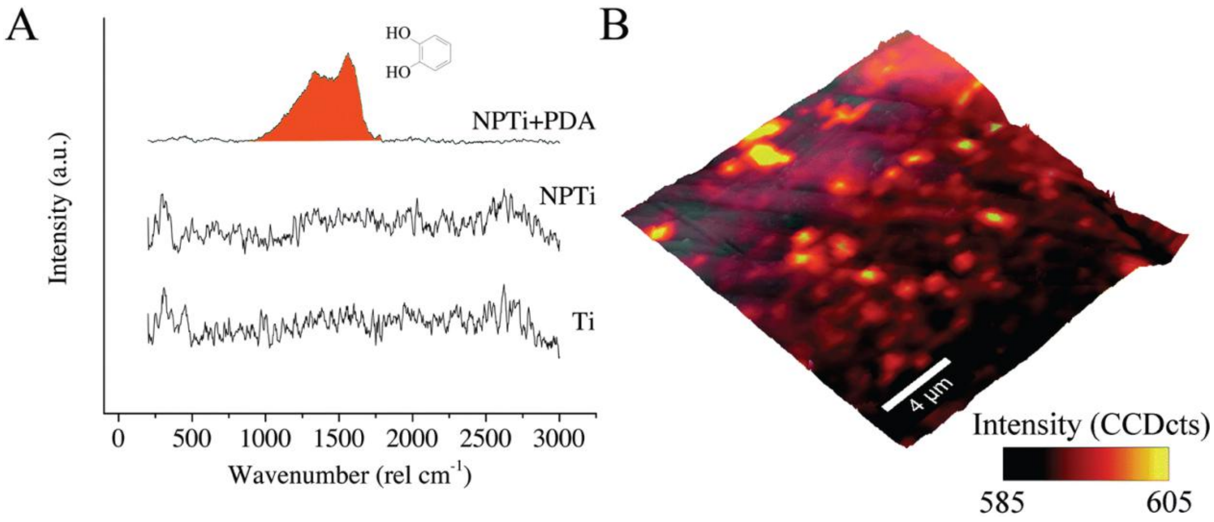

Fig. 4.2 Raman spectroscopy

(**A**) Representative Raman spectrum of Ti, NPTi and NPTi + PDA. (**B**) representative Raman + AFM overlay showing the intensity distribution of the catechol stretching vibrations band for NPTi + PDA samples.

solid line) as well as that of Ti (**Figure 4.3D**), NPTi (**Figure 4.3E**) and NPTi + PDA (**Figure 4.3F**) samples after 6 hours of immersion in α-MEM + 10% FBS are shown in **Figure 4.3**. Infrared analysis of α-MEM revealed a main absorption band at 1640 cm^1 (H-O-H bending in water) and minor peaks in the mixed region (1450-1220 cm^1) (**Figure 4.3D** inset, dotted line) which includes contributions from proteins, amino acids and glucose in the medium. Conversely, FBS displayed two main absorption bands at 1650 cm^1 (amide I) and at 1550 cm^1 (amide II), associated to the secondary structure of proteins,[96] as well as other minor peaks in the mixed region, most likely associated to additional vibrational modes of serum proteins (**Figure 4.3D** inset, solid line).

After immersion for 6 hours and thorough rinse in deionized water, all samples displayed the amide I and II bands (**Figure 4.3D-F**, red and green shadowing) as well as bands in the mixed region (**Figure 4.3D-F**, blue shadowing). In this case, the precise assignment of the bands in the mixed region was not possible since they can derive from constituents of both the medium and the FBS. In the case of NPTi + PDA samples, the amide I and II bands overlaid with those of poly(dopamine), represented with dotted vertical lines in **Figure 4.3F**. As one could expect, the same result was also observed after immersion for a longer interval (i.e. 3 days).

Taken together, our infrared data allow us to infer that proteins are retained by the three surfaces, regardless of their physicochemical characteristics. The amide I and II bands, evidence of the presence of adsorbed proteins, were in fact detected on Ti, NPTi and NPTi + PDA samples after exposure to complete medium for 6 hours. Therefore, we can conclude that during the growth phase, cells adhered and proliferated on surfaces all capable of retaining a protein adlayer. However, because of the multi-component nature of the system under investigation, we cannot draw definite conclusions about the precise identity, amount, conformational characteristics and/or surface-specific affinity of the adsorbed proteins. We can nonetheless hypothesize that the retention mechanisms most likely vary from one surface to the other, encompassing a combination of specific and non-specific interactions as well as physical entrapment effects exerted by the nanometric pores in the case of NPTi samples.[82]

To provide a better insight on whether protein adsorption was affected by a differential affinity with surfaces, we carried out liquid chromatography mass spectroscopic (LC-MS) analysis. **Figure 4.4** shows the unique spectral count for the 10 most abundant proteins retrieved from NPTi and NPTi + PDA samples after immersion in complete medium, normalized against the counts obtained on bare titanium. It can be readily observed that Ti, NPTi and NPTi + PDA samples are characterized by similar counts for 8 different proteins, suggesting that their adsorption occurs irrespective of the surface treatment. Only two pro-

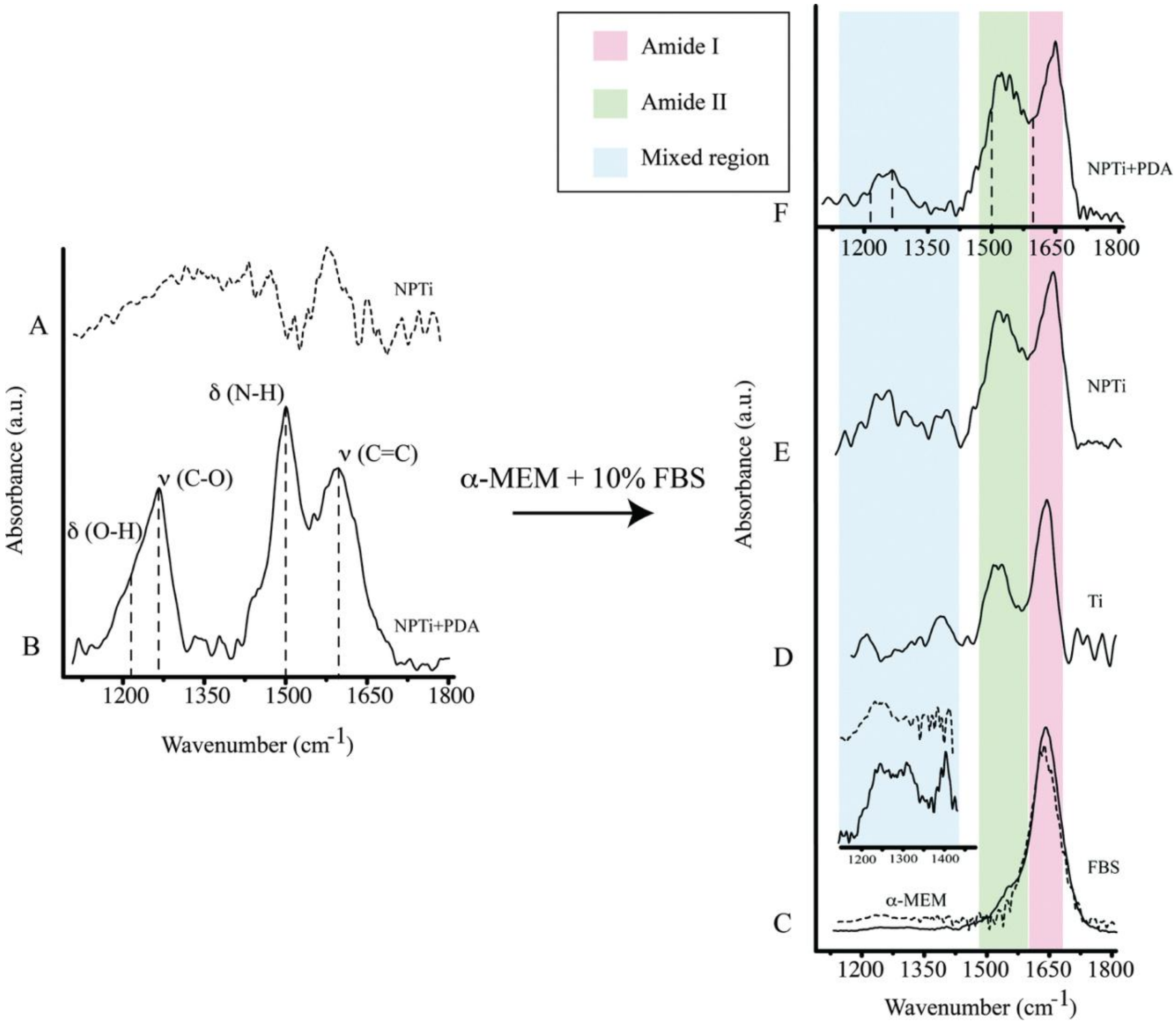

Fig. 4.3 ATR-FTIR

Representative ATR-FTIR spectrum of (**A**) NPTi, (**B**) NPTi + PDA, (**C**) 10% FBS (solid line) and α-MEM (dashed line). Enhancement of the mixed region in 10% FBS (solid line) and α-MEM (dashed line) (inset). Representative ATR-FTIR spectrum of (**D**) Ti, (**E**) NPTi and (**F**) NPTi + PDA (dashed lines show the center maxima of PDA bands.) after immersion in α-MEM + 10% FBS for 6 hours.

teins among the ones we tested (i.e. #5 and #10) showed a statistically significant difference when compared to bare titanium. Noteworthy, despite these differences, NPTi and NPTi + PDA samples exhibited similar values. In this context, it should be noted that the same trend was obtained by considering the total ion current (TIC) values (data not shown).

Taken together, the FT-IR and LC-MS results indicate that the PDA coating does not affect the amount of adsorbed serum proteins when compared to nanoporous surfaces as well as bare titanium. Noteworthy, a potential substrate-induced protein denaturation could still occur on surfaces and affect cell adhesion and proliferation, an aspect that, however, we could not address by these techniques.

4.3.3 MG-63 bioactivity experiments

In order to assess the biological response to PDA-coated titanium, we carried out cell culture studies with MG-63 human osteosarcoma cells. The choice of this cell line was motivated by the fact that among osteoblastic cell models used for in vitro studies (e.g. MC3T3-E1, Saos-2), MG-63 may provide a better alternative for studies interested in initial attachment to various materials.[28] This cell line also manifests a behavior closer to that of human osteoblasts while still providing the beneficial aspects of a cell line, such as the ease of maintenance, unlimited number of cells without the need for isolation.[28] In addition, MG-63 cells permit to avoid the interspecies and genomic differences that may occur with MC3T3-E1 cells, a factor which can make extrapolation to human clinical disease and treatment outcomes challenging.[28]

In this study, we first evaluated MG-63 cell viability at short (at 1, 4 and 8 hours) and longer (1, 2 and 3 days) intervals to validate the beneficial effects of PDA on cell adhesion and proliferation previously reported with different cell lines. **Figure 4.5** displays the relative variations in cell number determined by employing the CellProfiler software[97] to count DAPI-stained nuclei on the three surfaces. Our results demonstrate that in the shorter interval (1-4 hours), cell number did not significantly vary in relation to the substrate. While significant cell growth is not expected to occur in such relatively short interval, we can however consider this finding an indicator of a consistent seeding efficiency across different samples. Therefore, any difference in cell number that may result at longer intervals will be most likely associated to a substrate-dependent differential behavior during the late adhesion/proliferation phase. Noteworthy, from 8 hours onwards, proliferation of cells grown on NPTi + PDA samples experienced a statistical significant increase ($p < 0.05$) of 15-25% in respect to Ti samples, an evidence of the bioactive effects exerted by poly(dopamine). This result demonstrates that cells grown on the coating still maintain a higher viability at 72 hours when compared to uncoated controls, unlike what was

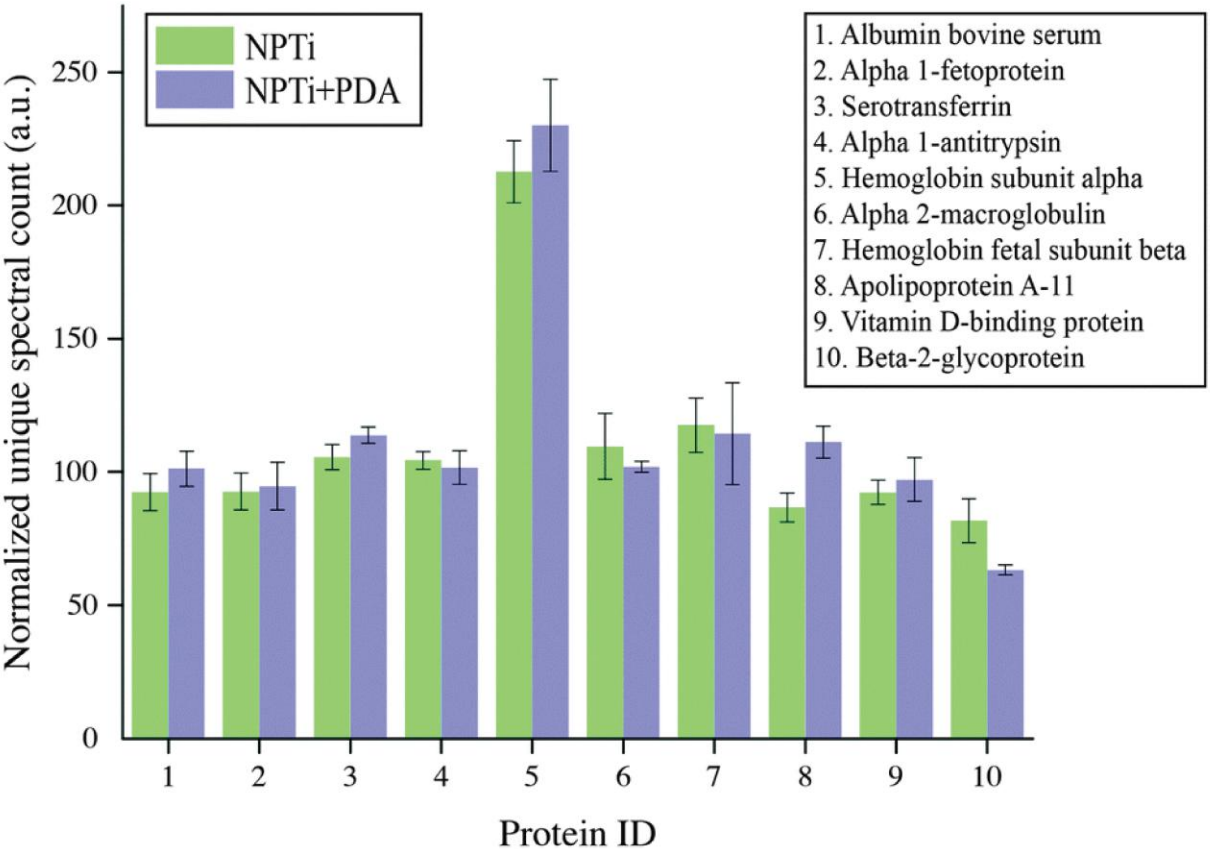

Fig. 4.4 LC-MS

Liquid chromatography mass spectroscopic (LC-MS) analysis of serum proteins adsorbed on NPTi and NPTi + PDA surfaces. Results show the unique spectral count normalized against the values determined on bare titanium controls.

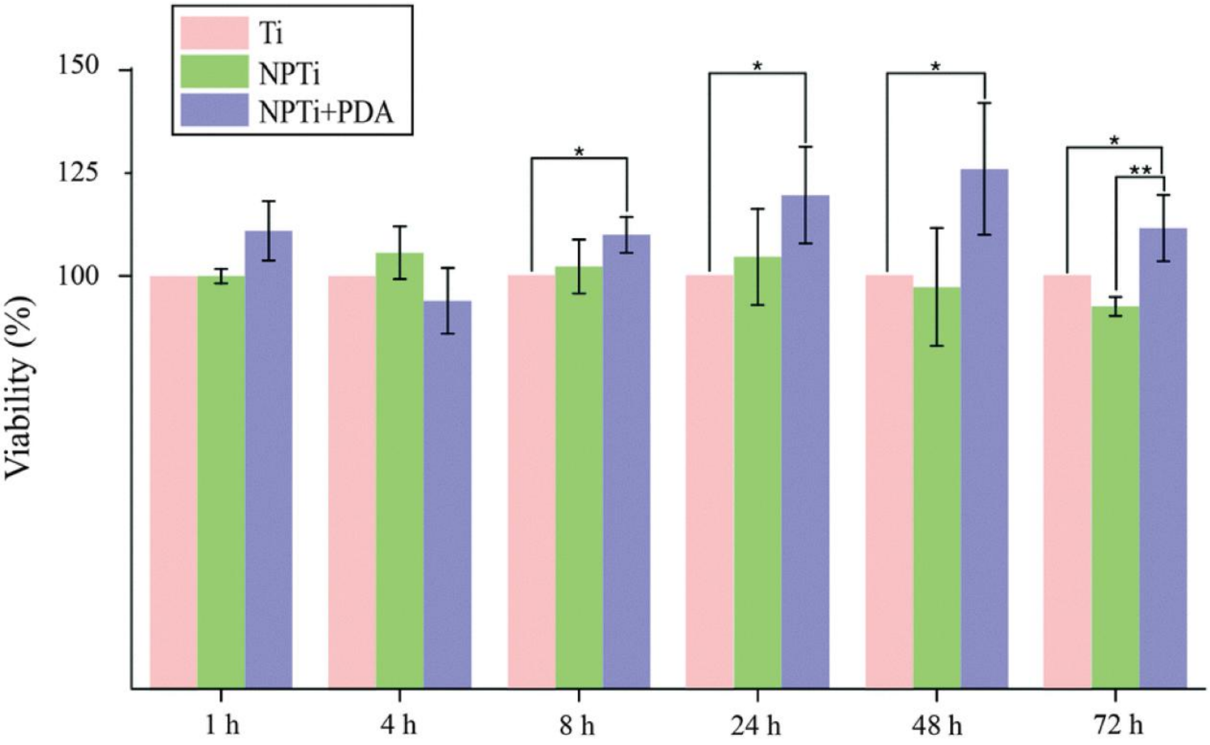

Fig. 4.5 MG-63 cell proliferation

Nuclei counts at different intervals (ANOVA test: * = $p < 0.05$, ** = $p < 0.01$). Results are expressed as percentage increase/decrease in respect to bare titanium (Ti).

previously reported for PDA-coated silicon oxide chips.[92]

However, when compared to nanoporous titanium, a marked increase in cell number was only detected at 3 days. It should be noted that nanoporous surfaces generated by oxidative nanopatterning inherently posses bioactive capacities, in particular the ability to enhance the proliferation of UMR-106 and primary calvaria-derived osteoblastic cells.[98]-[99] Therefore, while the PDA coating offers a distinctive advantage over bare titanium in terms of cell proliferation from early intervals onwards, its bioactive effects are similar to that of the bioactive nanoporous surface, and only become more evident in the longer term. Interestingly, our ATR-FTIR and LC-MS results demonstrate that despite the differential cellular behavior, serum proteins were equally adsorbed onto the three surfaces, a factor which was expected to yield similar biological outcome. The differential behavior in cellular colonization reported herein could be attributed to a denaturation of proteins adsorbed onto Ti and NPTi samples[25] and/or their nanoscale distribution.[100]

In order to close in on the effects exerted by poly(dopamine) at the single-cell level, we quantified substrate-dependent variations in the cellular morphology in terms of area (spreading), aspect ratio and form factor.[101][102] From the representative fluorescence images of cells shown in **Figure 4.5A**, it readily transpires that the morphology of cells adhering onto the poly(dopamine) after 1 hour of culture is distinctive, exhibiting a larger and more elongated structure with membrane projections. At 4 hours, cells on bare and nanoporous surfaces begin to assume a similar morphology, until it is no longer possible to qualitatively discern evident morphological differences at 8 hours. To further our investigation of cell morphology, we carried out image analysis to quantify parameters such as area, aspect ratio and form factor. **Figure 4.5B** shows that the surface area of cells in contact with the PDA layer is significantly larger (20-25%) when compared to that of cells adhering on both Ti and NPTi samples, demonstrating an enhanced cellular spreading at early intervals. The aspect ratio and the form factor were also affected by the substrate. In fact, the boxplots in **Figure 4.5C** confirm the qualitative observations: a more elongated shape characterizes cells on the PDA coating at 1 hour, but after 4-8 hours such morphology becomes predominant also in cells adhering on Ti and NPTi samples. **Figure 4.5D** provides information about the complexity of cellular shape by comparing the form factor, an indicator of a jagged edge. Cells on the PDA coating increasingly assume a more complex geometry as a function of time, which could be related to a membrane ruffling and/or the emission of membrane protrusions. The same trend was exhibited by cells adhering on the other two substrates, but their morphological complexity consistently resulted less pronounced than that of cells on poly(dopamine). A different trend was observed at later intervals. Cell area was greater on PDA-coated samples until 3 days of culture, when compared to that of cells proliferating on Ti and NP-Ti samples (**Figure 4.7A** and **B**). However, both the aspect ratio (**Figure 4.7C**) and the form factor (**Figure 4.7D**) were similar on the three surfaces, indicating that an elongated and well-spread morphology was achieved regardless of the substrate. Noteworthy, the form factor at 3 days for cells adhering onto NPTi and NPTi + PDA samples decreased, suggesting the onset of cellular events (e.g. differentiation) that could contribute to modify their membrane edge.

To better investigate potential molecular mechanisms for the variations in cell morphology on PDA-coated substrates, we investigated the development of focal adhesions (FAs) at earlier time points, where differences were most pronounced in both cell-substrate contact (**Figure 4.6B**) and aspect ratio (**Figure 4.6D**). FAs are dynamic membrane-associated protein complexes act as the interface between the extracellular matrix (ECM) and actin cytoskeleton through sensing of biochemical and/or physical cues. These cues, such as ECM proteins, interact with integrin transmembrane proteins leading to clustering and formation of early focal complexes, dot-like structures of 0.5 μm in length, that can mature into focal adhesions, 1-5 μm in length, in response to force transduction through myosin-II mediated contractile force.[103] Proper cell-ECM tethering and FA development has shown to be important for proper cell function including proliferation, motility and osteospecific differentiation of stem cells.[104] Qualitative assessment to investigate detectable differences in FA maturity indicated that presence and maturation of these complexes varied across all three substrates (**Figure 4.8A**). In particular, we observed that cells adhered on NPTi + PDA showed abundant and mature, dash-like, FAs as early as 1 hour after seeding whereas Ti and NPTi tended to show smaller round-like aggregations of vinculin that resembled early focal complexes. Wide spread mature focal adhesions were then seen on the NPTi and Ti conditions at 4 hours and 8 hours, respectively. Although accurate analysis of FA size was excluded because of the difficulty to measure it by confocal microscopy, assessing the quantity of FAs (focal adhesion and complexes together) during initial adhesion was achieved as displayed in **Figure 4.8B**. At 1 hour, there is a noticeable difference in detected FAs between all three substrates. When normalized to Ti, NPTi showed a substantial 25% increase whereas NPTi + PDA had the most dramatic increase of nearly 50%. After 4 hours, the effect of the substrate seemed to widen between Ti and the other two conditions. Although NPTi and NPTi + PDA conditions were approximately the same, they presented an almost 70% increase over Ti. Following 8 hours, all three conditioned presented cells with similar numbers of detected FAs. Later time point results were similar to that of 8 hours (data not shown). Quantitative confirmation of increased FA assembly and qualitative maturation help to explain the accelerated cell spreading on PDA-coated substrate seen in **Figure 4.6B**, although the mechanisms, whether physical or biochemical

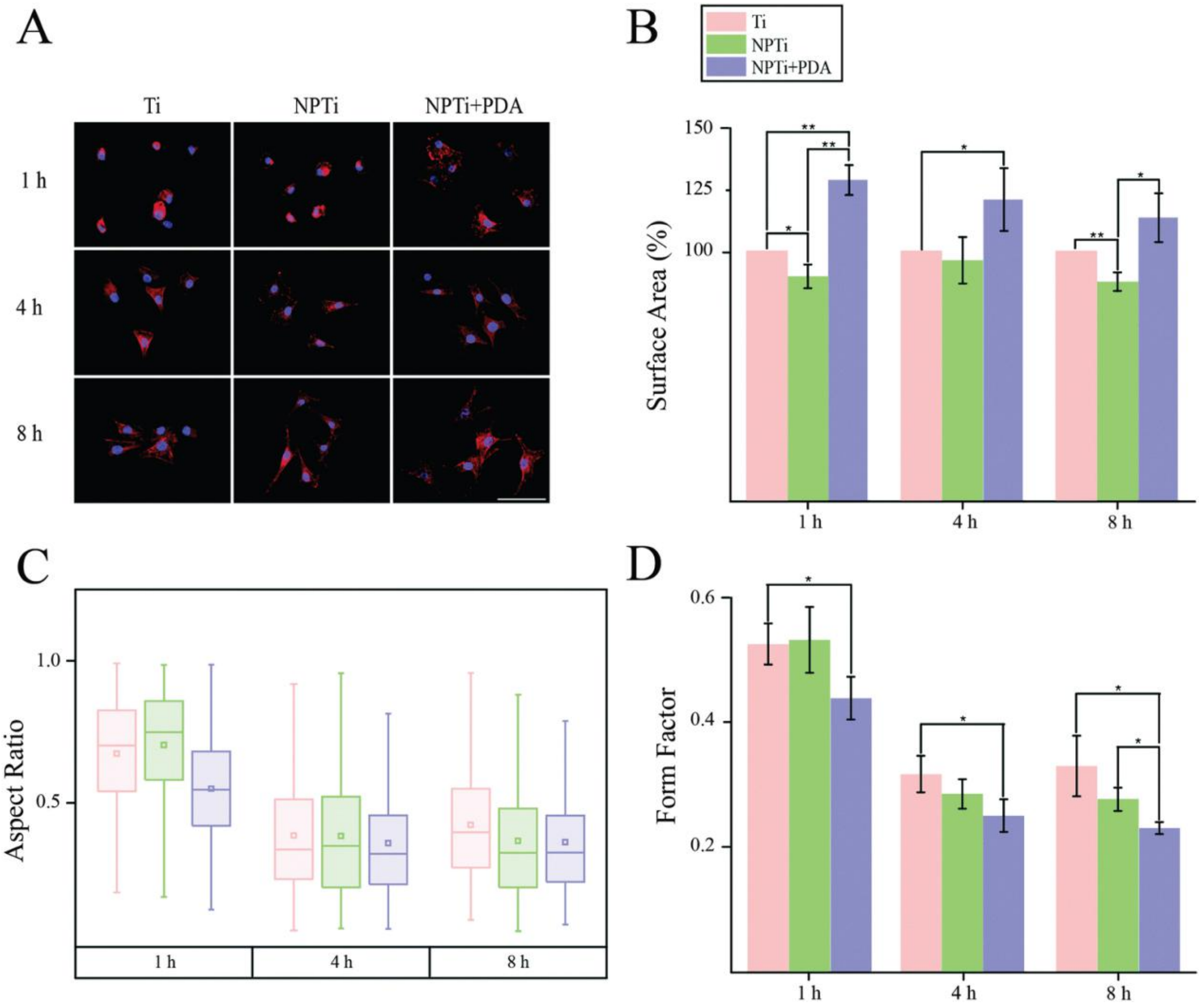

Fig. 4.6 Early cell spreading and morphology

(**A**) Fluorescence images (scale bar = 200 μm), (**B**) surface contact area (expressed as percentage increase/decrease in respect to bare titanium), (**C**) aspect ratio and (**D**) form factor of MG-63 osteoblastic cells adhering on Ti, NPTi and NPTi + PDA surfaces at 1, 4 and 8 hours. ANOVA test: * = $p < 0.05$, ** = $p < 0.01$

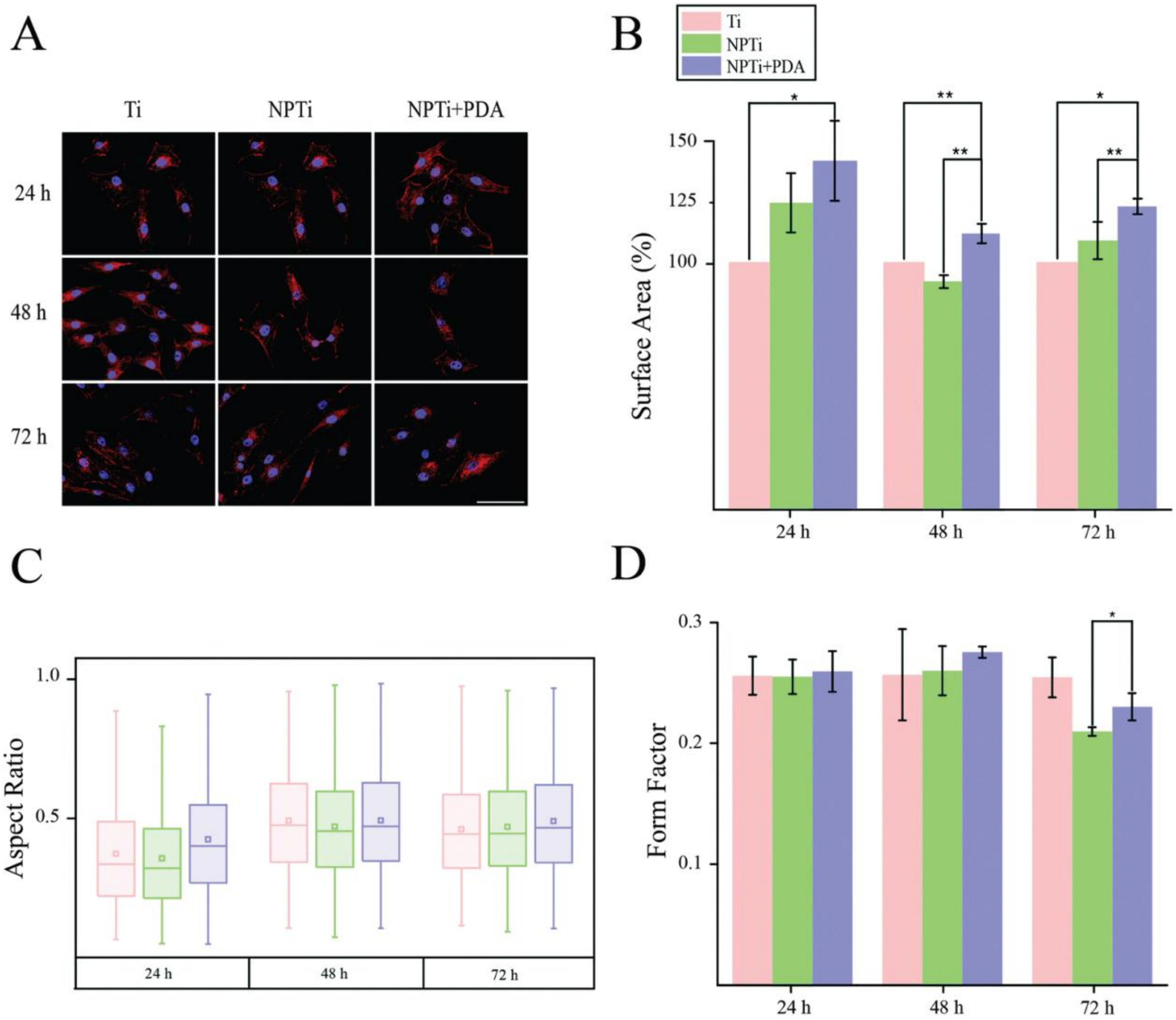

Fig. 4.7 Late cell spreading and morphology

(**A**) Fluorescence images (scale bar = 200 μm), (**B**) surface contact area (expressed as percentage increase/decrease in respect to bare titanium), (**C**) aspect ratio and (**D**) form factor of MG-63 osteoblastic cells adhering on Ti, NPTi and NPTi + PDA surfaces at 1, 2 and 3 days. ANOVA test: * = $p < 0.05$, ** = $p < 0.01$

cued, to which this is achieved is still undetermined. Noteworthy, while the FAs presence normalizes across all substrate after 8 hours, cells continue to present a more spread morphology and viability extending up to 3 days later. This indicates that there is a prolonged mechanotransductional effect between the substrate and intracellular signaling.

Of interest in mechanotransductional signaling pathways is the Rho family of GTPases, including Rac1, Cdc42 and RhoA, which act as molecular switches that influence cell processes such as cell cycle regulation, adhesion and actin cytoskeleton reorganization. These proteins switch between their active GTP-bound and inactive GDP-bound conformations. Integrin mediated Rac1 and Cdc42 activation has been shown to promote cell spreading through associated extension of lamellipodia and filopodia, respectively.[105] RhoA which plays an important role in actomyosin contractility and cell cycle maintenance, has been shown to have its activity modulated through mechanotransduction of cell adhesion molecules.[106] PCR assay suggested a trend towards lower expression of RhoA after 24 hours in NPTi and NPTi + PDA conditions when compared to bare titanium (67 ± 23% and 77 ± 22%, respectively), indicating lowered relative RhoA activity. In turn, lowered activity in NPTi and NPTi + PDA conditions could help to explain cell-substrate morphology as integrin-mediated lowering of RhoA though p190RhoGAP activity has been shown to promote cell spreading in addition to motility through regulation of cell protrusion and polarity.[107] Conversely, enhanced RhoA activity through use of constitutively active RhoA-V14 promotes commitment of hMSCs towards osteogenic lineages, as seen previously on PDA coated substrate, whereas dominant-negative RhoA-N19 led to commitment to an adipogenic fate.[108] This implies that there is an intricate mechanotransductional relationship between PDA and MG-63 cells that is not fully understood. Future work should have an emphasis on understanding the dynamics of Rho GTPase expression and activity, at both early and late time points, to elucidate how the accelerated cell adhesion, prolonged spreading, enhanced viability and amplified osteogenic differentiation is regulated and achieved.

4.4 Conclusion

In conclusion, our results reaffirm the potential of poly(dopamine) for biomedical applications, not only as an intermediate linker to immobilize bioactive agents, but also as a functional coating capable of beneficially affecting adhering cells. In this study, we have carried out detailed physicochemical characterization of a poly(dopamine) film deposited on nanoporous titanium and demonstrated its effects on MG-63 cell activity at short and longer intervals in terms of adhesion, viability and morphological changes. These may

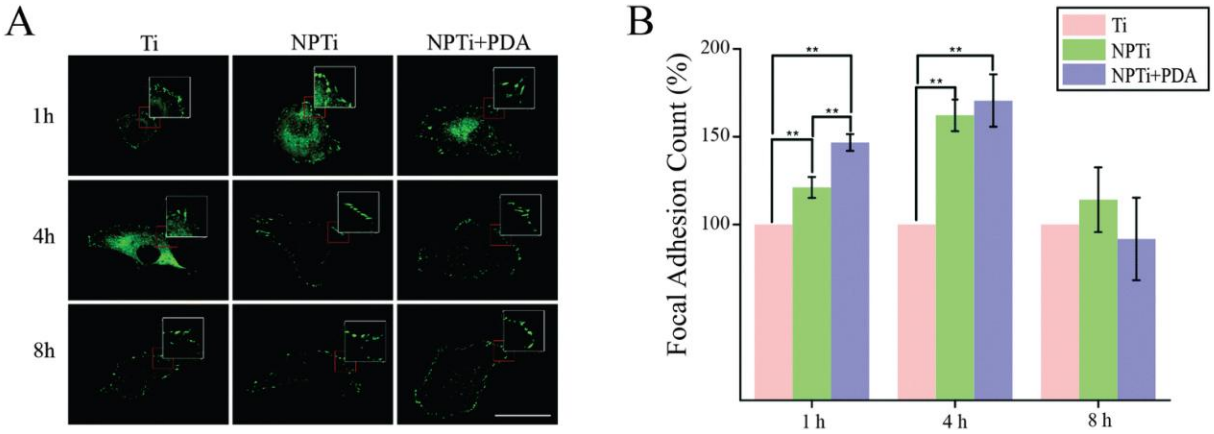

Fig. 4.8 Focal adhesion analysis

(**A**) Confocal fluorescence images of focal adhesion complexes at short intervals (scale bar = 50 μm). Insets were magnified 2x. (**B**) Number of focal adhesion complexes at short intervals. ANOVA test: ** = $p < 0.01$

be associated to the granular nanotopography of deposited PDA, its nanomechanical characteristics and chemistry, a differential influence on proteins adsorption (in terms of conformational arrangement) or, most likely, a synergistic combination of these factors. In addition, our results open the door new fundamental studies aimed at understanding additional aspects of the mechanisms that control cell spreading mechanics and motility on poly(dopamine).

CHAPTER 5

Method of deposition affects physicochemical, bioactive and serum-independent components of polydopamine coatings

5.1 Preamble

The research presented in this chapter is currently in preparation for publication.

5.1.1 Motivation

Over the past decade, PDA has increasingly become a material of interest in many applications, ranging from biomaterials to bioadhesives. Previous literature has attempted to study the mechanisms underlying the enhanced bioactivity attributed to PDA. However, significant discrepancies exist between these studies due to the unchecked constraint of experimental variables that are known to critically effect the deposition process (e.g., chemical composition of solvent), and which ultimately determine the final physicochemical makeup of the deposited polymer. The vast majority of research that examined the biological effects of PDA in forms of coatings have also been performed on differing metals or ceramics with little control for chemical or structural differences that the underlying substrate may exert on the deposition process. In addition, a major limitation of using these materials for imaging purposes is their opaque impenetrability to light which limits *in vitro* studies to static time points, preventing the perception of dynamic processes (e.g., cell migration) which are hallmarks of biological systems. Lastly, there is a lack of consensus over the role of protein adsorption in PDA-based biological models with opinions suggesting that PDA exerts effects through the improved adsorption and stability of sera protein. Recently, this supposition has been challenged by work in our lab that had shown no major differences between PDA and modified Titanium surfaces despite marked advantages in biological activity.

To address these limitations and to better understand the physicochemical affects of PDA, we sought to utilize two methods of deposition in order to generate two distinct surfaces with minimal variance in all other variables (e.g., reaction conditions). Both PDA surfaces were deposited on borosilicate glass (BSG), a transparent material commonly used as a base substrate in life sciences, which is advantageous due to its tightly controlled quality and minimal variance in topography during manufacturing. The use of glass enables the potential use of live-cell microscopy techniques that commonly utilize an inverted turret system which have, until now, been inaccessible. Subsequently, these choices of deposition standards and underlying substrate allow for (**1**) the critical analysis of physicochemical effects between substrate of varied physical attributes and (**2**) the confident attribution of these differences to the measured effects on our cell system. In addition, this controlled comparison provides an ideal platform to unequivocally determine whether there is a serum independent effect to PDA surfaces.

5.1.2 Hypothesis and objectives

In this study, we set out to elucidate two primary objectives.

- **Determining the differences between two uniquely controlled PDA surfaces.**
  This objective can be broken down into first a critical analysis of the physicochemical properties of each surface, and second whether these features result in a differential effect on human mesenchymal stem cells. We postulate that although both surfaces are presumed to be chemically similar, the increased roughness as a result of larger and more numerous aggregates will result in an enhancement of bioactivity.
- **Confirming whether PDA surfaces possess a serum independent effect and to what degree does the surface topology impact this effect.**
  Taking into consideration previous work in our lab, we postulate that there is indeed a serum-independent component of PDA surfaces and that it works in concert with circulation sera protein to elicit an overall enhancement of bioactivity.

5.2 Abstract

Polydopamine (PDA), a unique bioinspired polymer, has been a subject of interest in the field bioengineering, electrochemistry and structural engineering. Notably in the study of biomaterials, PDAs well documented biocompatibility and ability to be polymerized in diverse conditions has led to its varied use including as an immobilization platform for surface functionalization and bioactive cue for cell differentiation and mineralization. While classical deposition, here-in referred to as sPDA, involves the 12-72 hr dip-coating in an alkaline solution of Dopamine HCl, an interest in better control of the synthesis and structure

has led to studies on altering the base material hydrophobicity, deposition as a function of pH and temperature as well as UV mediated polymerization. Recently, a highly effective antibacterial PDA coating, here-in referred to as rPDA, has been generated with the sole addition of shaking during deposition.[14] These surfaces presented with an increased size and density of adhered PDA particles and were linked to a contact-kill mechanism against bacteria. It was undetermined whether it may affect cellular response. Previous work in our lab has shown that the classical deposition of PDA on nanoporous titanium enhances bioactivity without major changes to protein adsorption, suggesting an additional component to its effects (e.g., structural, chemical), which is yet to be determined.[26] Supplementary experiments have also suggested that PDA has a serum-independent effect on cell behavior and viability.

In an effort to better understand the roles of sera and topography, we sought to investigate (**1**) the potential cellular benefits of the novel antibacterial surface and (**2**) to the role of the surface alone in the enhancement of bioactivity, independent of sera adsorption. This study provides one of the most comprehensive physicochemical analyses of PDA surfaces while showing that the simple addition of shaking during deposition generates a PDA surface that, in addition to its previously reported antibacterial properties, is now characterized with further enhancing bioactivity beyond that of sPDA and glass substrate. Regardless of protein preadsorption or circulating serum, rPDA surfaces yield advanced cell spreading morphologies in both normal and serum-starved cells. It has also been shown that the surface works synergistically with adsorbed and circulating sera protein, supporting the hypothesis that it possesses lone physicochemical cues that work in concert with the environment to elicit its advantageous affects. On going work has also shown signs of greater osteogenic differentiation which, in combination with its added bioactivity and antibacterial properties, advances its potential as a surgical bioadhesive. Subsequently, rPDA may promote osseointegration while reducing post-operative infection thereby furthering polydopamine's prospects in orthopedic bioengineering and beyond.

5.3 Results and discussion

5.3.1 Physicochemical analysis of generated surfaces

5.3.1.1 rPDA surfaces display greater wettability with distinct structures under SEM

Scanning Electron Microscopy (SEM) imaging was employed to confirm a successful deposition of PDA coatings and subsequently to provide insight to the degree of aggregate formation as well as qualitative surface roughness (**Figure 5.1C**). Micrographs were analyzed for the transverse diameter of aggregates which we classified into small (<300 nm) and large (>300 nm) structures. Results from SEM image analysis are summarized in **Table 5.1**. The small nanostructures on rPDA (232 ± 51 nm in width) were found to be 70% larger than those on sPDA (136 ± 47 nm in width) with relatively low statistical deviation providing confidence in a predictable relationship in size. This trend continued with larger nanostructures on rPDA (1726 ± 687 nm in width), which resulted to be 131% larger than those on sPDA (743 ± 687 nm in width). However, in this case, the statistical deviation was found to be substantial, suggesting that the formation of these aggregates is inherently stochastic and unpredictable.

While the mechanism of aggregate formation is still largely unknown, control in our deposition process provides insight into two key variables: solvent choice and local temperature. It has been determined that the choice of Tris as the reaction solvent generates particles of larger size, when compared to other common solvents (e.g., NaOH).[109] In our study, we used 2.5x the concentration (25 mM) of the common Tris-HCl for PDA coating, to stay in line with the previous work on rPDA, which may further the impact of Tris on aggregate formation.[14] A combination of increased environmental heat and stirring has also been shown to rapidly increase the thickness of PDA films.[92] However, the mechanism and impact on the aggregate formation was omitted and no control for the local increase in heat, resulting from the transfer of kinetic energy. As a result, we suggest that the combination of Tris-HCl as our solvent, in relatively high amounts, with the addition of local heat through shaking, is sufficient to generate these surfaces.

Following the deposition of sPDA and rPDA surfaces on BSG, contact angle measurements were performed to confirm the generation of a surface in line with previous literature.[14] Contact angle goniometry was utilized to measure surface hydrophilicity and as an indicator of surface energy which have been previously reported to increase with PDA coatings on a variety of materials.[14][110] In agreement with this, PDA surfaces presented with substantially decreased static contact angle when compared to the 78° of BSG, with sPDA and rPDA with 52° and 26°, respectively (**Figure 5.1A-B**). While values for classically deposited PDA (sPDA) are consistent with previously published values (ranging 50° to 70° depending on the underlying substrate), our rPDA coatings have a notably larger contact angle.[25] Differences in apparatus during rotational deposition, including speed variability and use of a shaking versus rotational platform, are thought to contribute to these discrepancies. Although the initial concentration of PDA during deposition and thickness of the film has been shown to not affect surface energy, the presence of larger observed structures at the nano- and microscales are thereby suggested to result in enhanced Wenzel homogeneous wetting due to the improved immersion of the droplet in the asperities of the

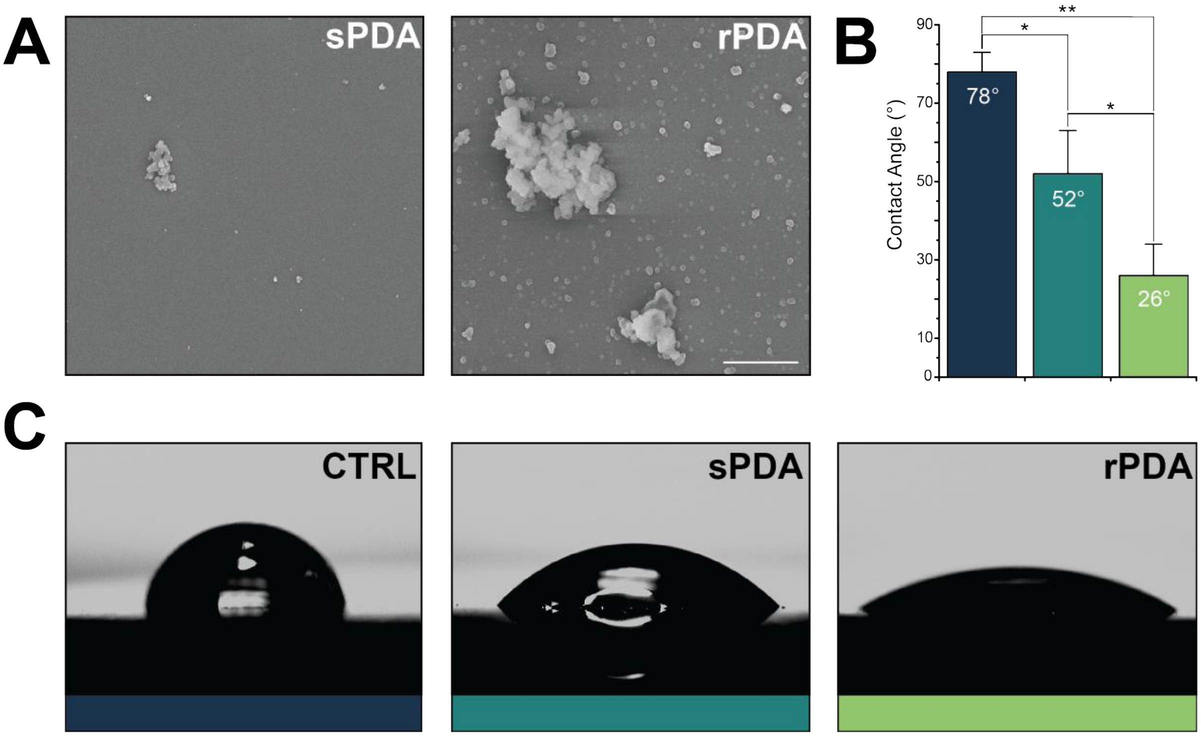

Fig. 5.1 The effect of PDA coating on surface wettability and initial visualization

(**A**) Contact angle goniometry of control, sPDA and rPDA surfaces with reference colours underneath each image. (**B**) Summary of contact angle measurements. (**C**) SEM images of sPDA and rPDA coatings.

surface.[11]

5.3.1.2 Deposition method greatly effects nanotopography of gross aggregate and interaggregate regions

DPFM-AFM imaging was employed to create large scale three-dimensional reconstructions of the sPDA and rPDA surfaces with the added benefit of measuring a variety of mechanical properties. Similar to what was initially seen on SEM images, rPDA surfaces at smaller scales presented with a topography consisting of comparatively larger scale aggregates in a higher density (**Figure 5.2A-B**).

Nanostructures were analyzed for height and diameter dimensions with rPDA structures presenting with a $\sim$7-fold increase in average diameter and $\sim$40-fold increase in average height when compared to sPDA (**Table 5.1**). These structural differences contributed to the substantial increase in comparative rPDA surface roughness with a sPDA RMS of 5.2 $\pm$ 2.1 nm and a rPDA RMS of 95.6 $\pm$ 12.7 nm. Coating glass with sPDA led to an overall 1.2% increase in surface area whereas rPDA led to an overall 15.6% increase in surface area, a factor which is believed to contribute to its bioactive effects (**Table 5.1**).

5.3.1.3 rPDA interaggregate regions are substantially rougher than sPDA

SEM imaging of the interaggregate regions was inconclusive as to the difference between sPDA and rPDA. To overcome this limitation, AFM was employed to visualize 3-D morphological changes in these regions. NC-AFM was chosen as high-resolution mapping of small regions with DPFM-AFM led to substantial degradation of nanographs which we suggest to be due to high tip-surface adhesive forces required for detachment from the film (**Table 5.2**). Results show that the rPDA interaggregate regions are characterized by a maximum height of features $>$400% than that observed in sPDA (**Figure 5.2C-D**). This translates to a significant difference in roughness with a rPDA RMS of 22.62 $\pm$ 5.4 nm and a sPDA RMS of 5.01 $\pm$ 1.31 nm. In addition, the surface area of these regions followed the global trend with sPDA having a 1.5% increase as opposed to 9.9% for rPDA.

5.3.1.4 Discrimination of structures is critical when assessing mechanical properties of PDA surfaces

To better understand the mechanical properties of the polymer surfaces, DPFM data was processed into $Force\,[F] - Indentation\,[z(t), nm]$ curves according to a previously published procedure.[75] While global contrast maps for stiffness qualitatively indicated very little difference across the surface (not shown), adhesion contrast maps pointed toward

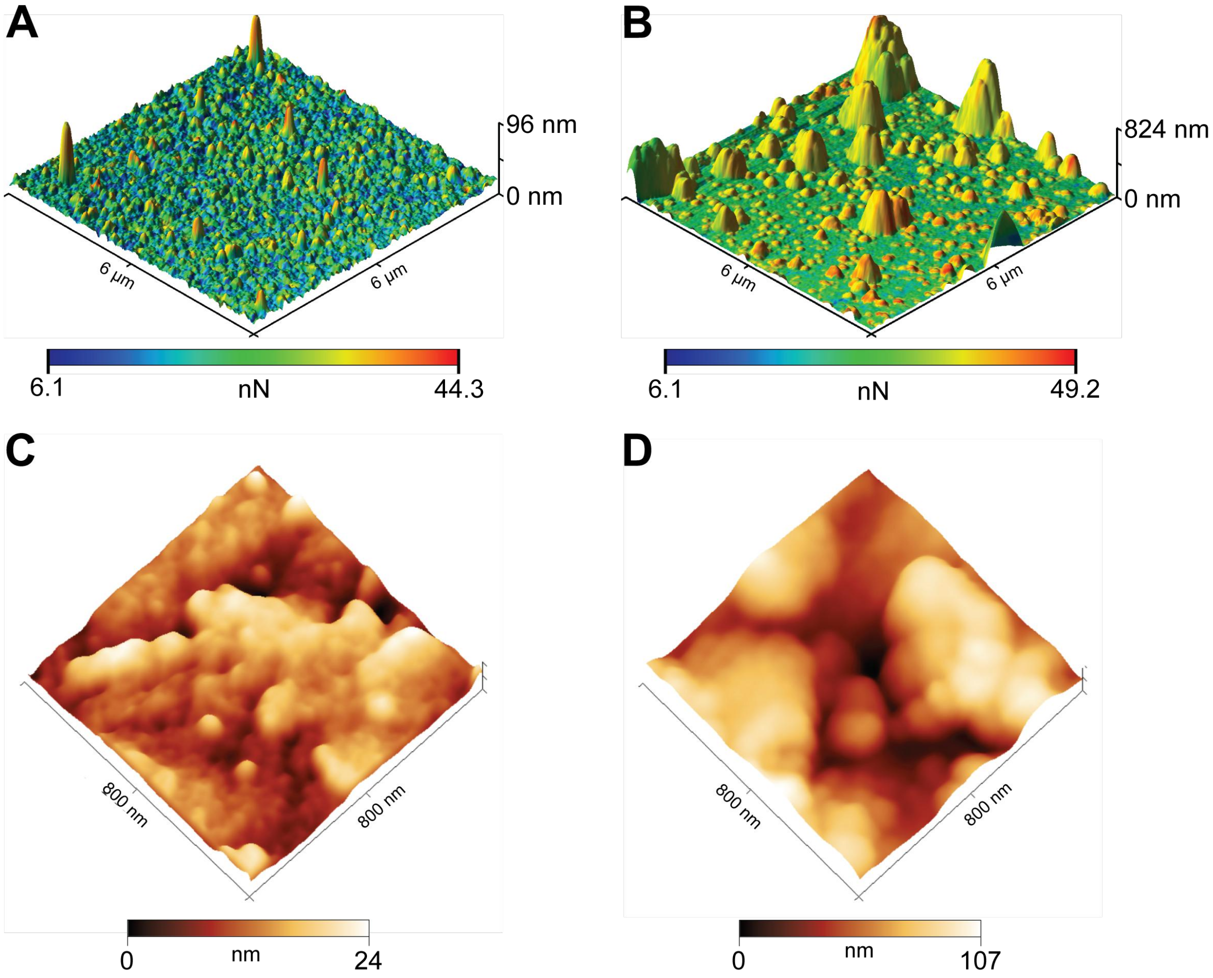

Fig. 5.2 DPFM-AFM of large scale topography with NC-AFM of interaggregate regions

(**A-B**) DPFM-AFM imaging of (**A**) sPDA and (**B**) rPDA surfaces overlayed with measured adhesion force values, referenced in colour bars. (**C-D**) NC-AFM imaging of (**C**) sPDA and (**D**) rPDA interaggregate regions. Colour bar represents feature height.

Table 5.1 Summary of structural measurements

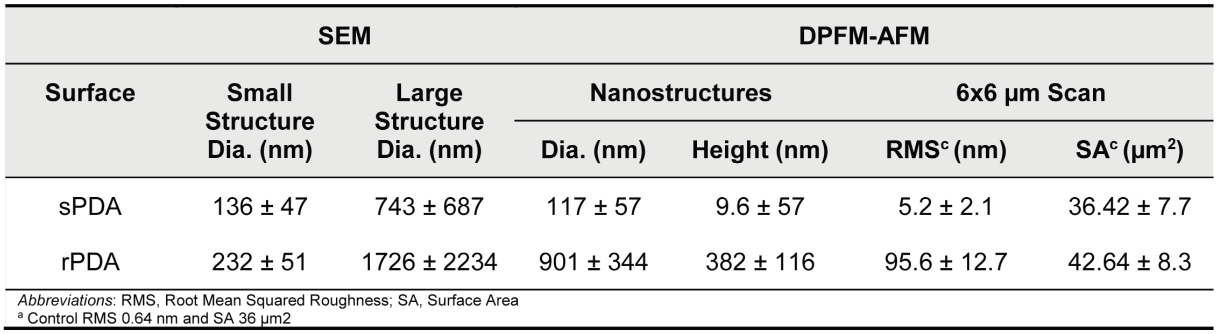

	SEM		DPFM-AFM			
Surface	Small Structure Dia. (nm)	Large Structure Dia. (nm)	Nanostructures		6x6 µm Scan	
			Dia. (nm)	Height (nm)	RMS[c] (nm)	SA[c] (μm^2)
sPDA	136 ± 47	743 ± 687	117 ± 57	9.6 ± 57	5.2 ± 2.1	36.42 ± 7.7
rPDA	232 ± 51	1726 ± 2234	901 ± 344	382 ± 116	95.6 ± 12.7	42.64 ± 8.3

Abbreviations: RMS, Root Mean Squared Roughness; SA, Surface Area

[a] Control RMS 0.64 nm and SA 36 µm2

structure-specific differences (not shown). Consequently, processed data was further discriminated as either underlying film or aggregate formation. The average stiffness, hysteresis and compliance were found to be consistent across both PDA surfaces, whether as an aggregate or film (**Table 5.2**). However, disparity was seen regarding structure-specific adhesion as initially identified by the contrast maps and confirmed with subsequent post-processing.

Regardless of the sample condition, the force required to detach the tip from the underlying film and the associated detachment energy were found to be substantially greater when compared to aggregates. In fact, compared to aggregates, detachment from the sPDA film required 471% more force (film: 35.66 ± 6.35 nN; aggregates: 7.58 ± 0.78 nN) and 1854% more energy (film: 1056.97 ± 354.32 nJ; aggregates: 56.98 ± 10.83 nJ). Similar results were found on rPDA with film detachment requiring 493% more force (film: 37.37 ± 7.57 nN; aggregates: 7.58 ± 0.77 nN) and 2040% more energy (film: 1162.41 ± 445.42 nN; aggregates: 56.98 ± 10.71 nN), versus aggregates.

To provide additional insight in PDA nanomechanical properties, we calculated Young's modulus by using the DMT method, versus Hertz, due to its inclusion of adhesive forces in the calculation.[111] It followed that the aggregates on both surfaces showed a substantially lower elastic modulus (sPDA: 8.41 ± 1.62 GPa; rPDA: 7.79 ± 2.33 GPa) than their respective film (sPDA: 2.63 ± 3.12 GPa; rPDA: 3.51 ± 2.90 GPa). Comparatively, the elastic modulus of the films is on the lower range of common polymers, similar to that of Polymethylmethacrylate (PMMA, 2.43 GPa), while the aggregates are in the middle of the previously reported range of PDA surfaces (4.3-10.5 GPa).[112] Accordingly, the global Youngs modulus of the rPDA (6.69 ± 3.22 GPa) was found to be greater than sPDA (4.81 ± 2.76 GPa) which we suggest is a result of greater proportion of the surface composed of aggregates versus film.

5.3.1.5 XPS indicates similar chemical groups in the C 1s, N 1s and O 1s regions

Although X-ray photoelectron spectroscopy (XPS) has been previously used to elucidate the functional groups and elemental composition of the bulk polymer, successive dip-coating and short interval depositions, it is still unknown whether the introduction of kinetic energy may affect the surface chemistry.[113][84][77] Initially, a survey scan was carried out on all surfaces confirming the characteristic $Si\ 2s$ and $Si\ 2p$ regions of borosilicate glass which were lessened, though still identifiable, after coating (**Figure 5.3**). Major differences consisted in the appearance of a signal at the $N\ 1s$ field and enhancement of the $C\ 1s$ signal in sPDA and rPDA surfaces. Further analysis was carried out specifically in the $C\ 1s$, $N\ 1s$ and $O\ 1s$ regions to determine differences in functional group prevalence. The

Table 5.2 Summary of measured mechanical properties from DPFM data

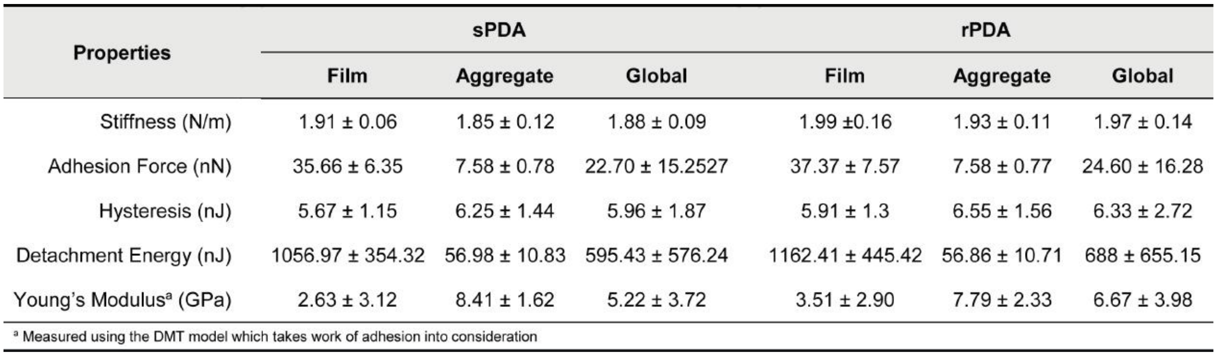

Properties	sPDA			rPDA		
	Film	Aggregate	Global	Film	Aggregate	Global
Stiffness (N/m)	1.91 ± 0.06	1.85 ± 0.12	1.88 ± 0.09	1.99 ±0.16	1.93 ± 0.11	1.97 ± 0.14
Adhesion Force (nN)	35.66 ± 6.35	7.58 ± 0.78	22.70 ± 15.2527	37.37 ± 7.57	7.58 ± 0.77	24.60 ± 16.28
Hysteresis (nJ)	5.67 ± 1.15	6.25 ± 1.44	5.96 ± 1.87	5.91 ± 1.3	6.55 ± 1.56	6.33 ± 2.72
Detachment Energy (nJ)	1056.97 ± 354.32	56.98 ± 10.83	595.43 ± 576.24	1162.41 ± 445.42	56.86 ± 10.71	688 ± 655.15
Young's Modulus[a] (GPa)	2.63 ± 3.12	8.41 ± 1.62	5.22 ± 3.72	3.51 ± 2.90	7.79 ± 2.33	6.67 ± 3.98

[a] Measured using the DMT model which takes work of adhesion into consideration

functional groups that were analytically deconvoluted correspond to those found in **Table 5.3**.

The C $1s$ signal in borosilicate glass is assumed to be due to adventitious carbon contamination and is disregarded. Reviewing the fitted peaks for both PDA samples, the three major peaks noted in **Table 5.3** are consistent with previous literature, however we could not clearly identify the $\pi \rightarrow \pi*$ shakeup satellite which is indicative of aromatic carbon species in either surface.[77]

N $1s$ regions were analyzed and fit for the primary (R-NH_2), secondary (R-NH-R) and tertiary/aromatic (=N-R) amines with respective binding energies noted in **Table 5.3**. Each class of amine has been associated with either PDA (primary, secondary) or its intermediates (secondary, tertiary) with functional group dominance being shown to change with deposition time and reaction conditions.[77][109] Primary amines, associated with the structure of unreacted dopamine, are reported in literature to be most prevalent at very short deposition periods ($<$ 2 minutes) with the formation of intermediates and subsequent polymer in later timepoints leading to a proportional transition toward secondary and tertiary amines with the majority determined as secondary.[77] Although sPDA and rPDA surfaces agree with minimal detection of primary amines, as expected due to the length of deposition, the proportion of secondary and tertiary amines deviate from literature with the vast majority detected as tertiary/aromatic amines (**Figure 5.3**). We suggest this is due to the use of Tris buffer as the solvent in our deposition series, versus the bicarbonate buffer of the Zangmeister et al. (2013) study. Evidence supporting this supposition has been recently reported in Patel et al. (2018), which has shown that the chosen solvent critically impacts the predominance of terminal amines with a comparative preference for primary and secondary amines in bicarbonate buffer and secondary and tertiary/aromatic in Tris buffer. Although results from Patel et al. (2018) still show secondary amines as the most prevalent, the dominance of tertiary/aromatic amines in our samples can be best explained by the use of comparatively high concentrations of Tris (25 mM v. 10 mM) which may increase the opportunity for nitrogen in Tris to covalently bind to the quinone groups of the polymeric surface.[114] Additional differences may be attributed to the wettability and chemistry of the underlying surface which can affect PDA deposition.[41]

O $1s$ regions were fit with two primary peaks representing alcohol (C-O), associated with the C-OH of catechol groups and indoles, and carbonyl (C=O), associated with the structure of quinones. Our results show a predominance of hydroxyl over carbonyl functional groups. This is in line with literature that use Tris as a reaction buffer and can be best explained by the conversion of intermediate quinone carbonyl groups to indole hydroxyl groups during the covalent binding of Tris amino groups (e.g., 5,6-indolequinone

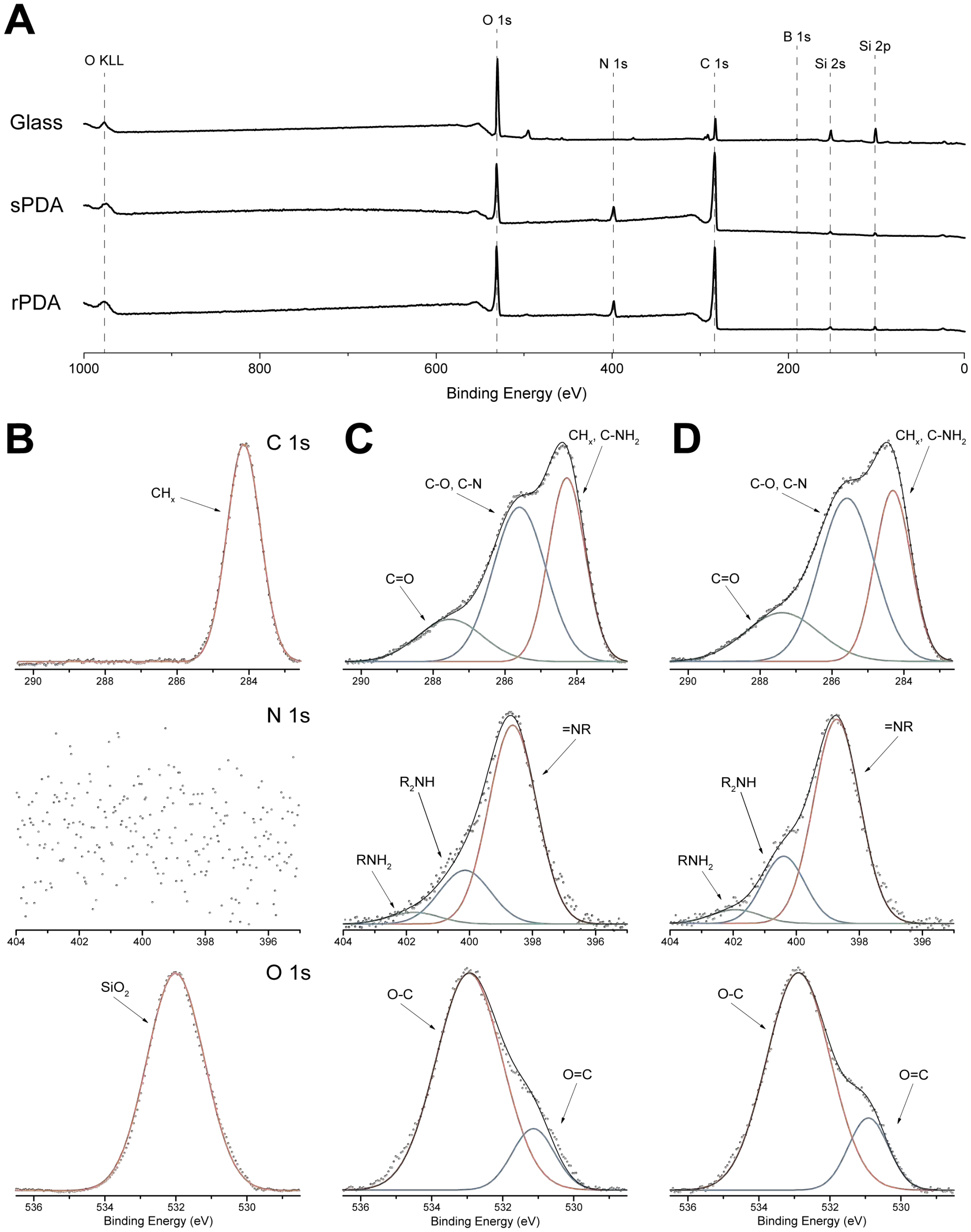

Fig. 5.3 XPS wide-scan survey with analysis of $C\ 1s$, $N\ 1s$ and $O\ 1s$ regions

(**A**) Wide-scan survey results, (**B-D**) High resolution spectra of $C\ 1s$, $N\ 1s$ and $O\ 1s$ regions for (**B**) borosilicate glass, (**C**) sPDA and (**D**) rPDA.

	Functional Group	Binding Energy (eV)
C1s	CH_x, $C-NH_2$	284.7 ± 0.2
	C-O, C-N	285.9 ± 0.1
	C=O	287.1 ± 0.3
N1s	=N-R	398.5 ± 0.3
	R-NH-R	399.9 ± 0.1
	R-NH2	401.5 ± 0.3
O1s	O=C	531.0 ± 0.1
	O-C	532.9 ± 0.1

Table 5.3 Table of XPS functional groups used for peak fitting

$\rightarrow$ 5,6-dihydroxyindole).[109][22]

5.3.2 Comparative bioactivity analysis of sPDA and rPDA surfaces

In this section, we compare the differential cellular response to sPDA and rPDA surfaces. As demonstrated in the previous chapter, these surfaces are chemically similar but differ in terms of global topography and bulk physical properties. Based on such detailed physicochemical characterization, we are now able to assess the influence of topographical and physical variables on the bioactivity of PDA surfaces. This analysis includes the morphological, structural and dynamic (e.g. proliferation, migration) characterization of hMSCs under normal (i.e. culturing conditions).

5.3.2.1 rPDA enhances cell spreading when compared to sPDA and CTRL

The differential activation of integrin-mediated transmembrane mechanotransductive complexes, in response to recognition of substrate physicochemical features, will in turn modulate several characteristics of the dynamic spreading process including velocity and predominance and behavior of morphological structures (e.g. filopodia).[63] Another dependent variable is the initiation of spreading after initial cell-substrate adherence, which will lead to the transition from the spherical to circular morphologies which represents uninitiated and initiated spreading, respectively.[64] As a result, changes in cell structure during this process may allow for the progressive categorization of cells into a sequence of well-defined spreading morphologies. After 1h and 4h, hMSCs plated glass and PDA samples with regular culture media were imaged and categorized into six distinct morphologies, ranked in the progression of cell spreading (**Figure 5.4A**).

At 1h, hMSCs seeded on both PDA surfaces displayed advanced cell spreading morphologies, when compared to control (**Figure 5.4B**). Respectively, the morphology for cells on sPDA and rPDA was predominantly protrusive (62.1% v. 56.4%) followed by elongated (13% v. 29.7%). Interestingly, while control surfaces had the greatest comparative proportion of cells being of early circular stage (26.3%) compared to sPDA (9.9%) and rPDA (6.8%), they also possessed the greatest share of the advanced elongated morphology with 13.6% versus 3.1% and 3.7% for sPDA and rPDA, respectively. These elongated morphologies are correlated to the generation of cell traction forces throughout the cell body via actin stress fibers which is the result of focal adhesion maturity.[58]

At 4h, the development of a well-spread morphology on rPDA is more evident with 68.2% of cells showing of the most advanced multipolar morphology, which is a nearly 63% and 1300% greater proportion than that observed on sPDA (41.8%) and on control

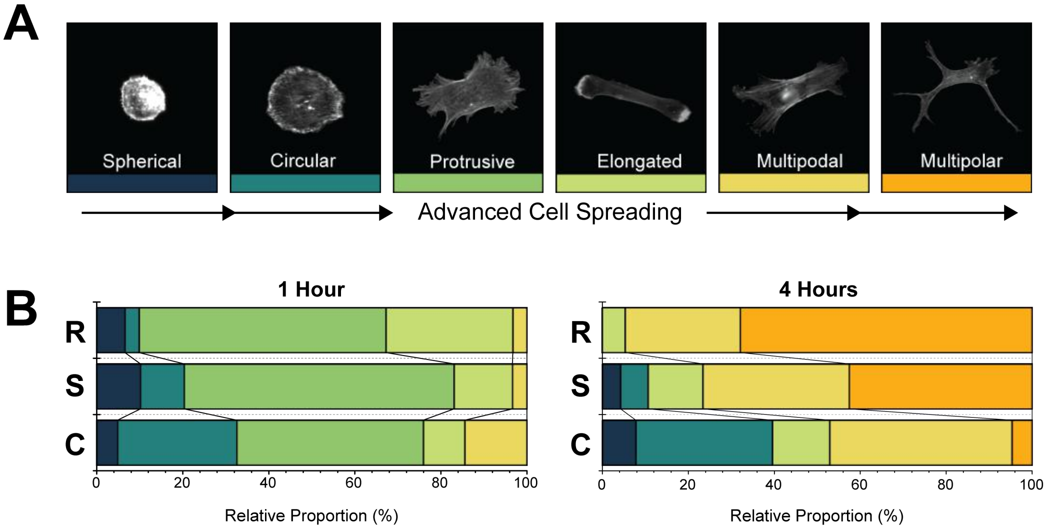

Fig. 5.4 Proportional categorization of early spreading morphologies in the first 4h with regular culturing conditions

(**A**) Legend of morphologies exhibited through the advancement of cell spreading with correlated colour bars. (**B**) Relative proportions of morphologies categorized from hMSCs incubated in serum-containing media and seeded on CTRL [C], sPDA [S] and rPDA [R] surfaces.

surfaces (5.2%), respectively (**Figure 5.4B**). The relative proportion of the next most advanced morphology, namely multipodal, was statistically similar between sPDA (34.5%) and rPDA (27.2%). Conversely, the multipodal proportion in control surfaces (42.9%) was significantly greater than both PDA surfaces. Of note, all cells characterized on rPDA surfaces had progressed beyond the initial spherical and circular morphologies which signifies that all populations of cells have been able to generate adequate cell-substrate signaling (e.g., integrin clustering) in order to progress to later morphologies.

Interestingly, the proportion of cells in the early spherical and circular stages on control surfaces between 1h and 4h were found not to be significantly different ($p > 0.05$). This suggests an inability for control surfaces to adequately activate integrin clusters, such as $\alpha5\beta1$, whose expression has been shown to be critically important in the initiation of spreading and subsequent spreading-dependent cell proliferation.[115] Wang et al. (2013) was able to conclusively show that PDA coatings stimulated the incredible expression and activation of integrin $\alpha5\beta1$, however it was not determined whether this is the result of intrinsic activity of PDA or its ability adsorb and stabilize circulating sera protein. Although our experiments were performed in normal culturing conditions with circulating serum protein, the evidence of enhanced cell spreading morphologies in rPDA versus sPDA suggests that the differences in physicochemical properties (e.g., feature size and distribution) may be a defining characteristics of intrinsic PDA bioactivity, reducing the extent of the influence of protein adsorption.

5.3.2.2 Cells adhering on rPDA are well spread at early timepoints but display contracted morphology within the first 24h hours

Local and bulk interfacial characteristics, including stiffness and topography, can directly affect the activation of integrin-ECM binding groups which play a role in the kinetics of spreading and motility.[116][62] Once initiated, cells will undergo a fast period of quick isotropic spreading, represented herein by circular morphology, characterized by lower centripetal actin flow indicative of low projection formation.[65] Following this, the cells undergo anisotropic spreading through a sequence of ”stochastic, transient extension periods” (STEPs) that results in high centripetal actin flow due to peripheral projection formation and is represented herein by the protrusive morphology.[65] These generalized processes, in combination with resultant substrate induce cell structure formation, will produce whole cell morphologies that can be quantitatively analyzed to better understand the cell-substrate relationship.

Using post-processing of fluorescence microscopy images in a custom Cellprofiler pipeline, cell area, perimeter, form factor and compactness were quantified. Form factor

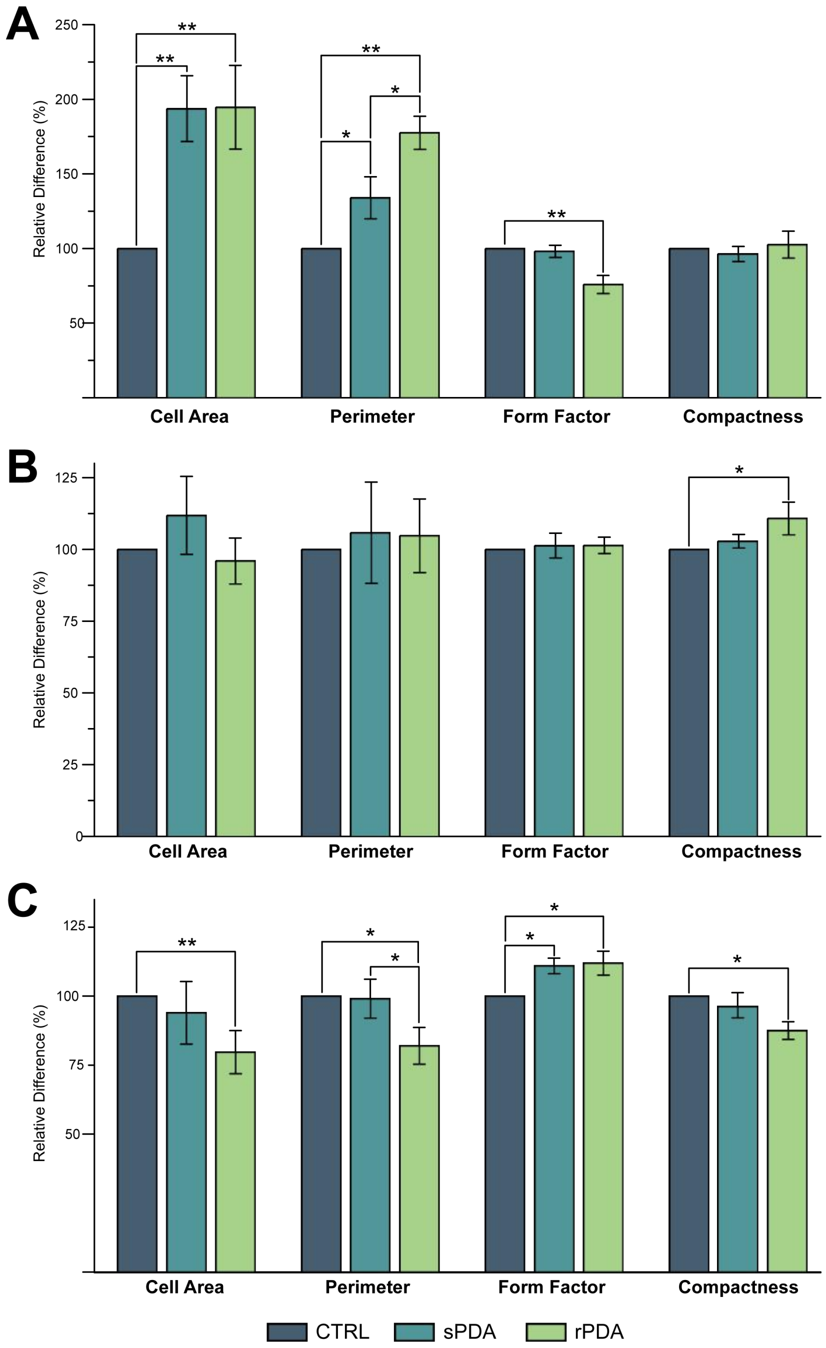

Fig. 5.5 Advanced cell structure analysis in the first 24 hours

(**A**) 1 hr, (**B**) 4 hrs and (**C**) 24 hrs after seeding. Measures included cell area, perimeter, form factor and compactness. Form factor is the measure of a cell circularity whereas a value of 1 representative of a completely circular cell and 0 being that of a linear cell and is calculated by $4*\pi*(\text{Area}/\text{Perimeter}^2)$. Compactness is calculated as the mean squared distance of all pixels of the object to the centroid of the cell with a regular object having a value of 1 and irregular objects having a value of 0. ANOVA test: $*=p < 0.05$; $**=p < 0.01$

is the measure of a cell circularity whereas a value of 1 representative of a completely circular cell and 0 being that of a linear cell and is calculated by 4*π*(Area/Perimeter^2). Compactness is calculated as the mean squared distance of all pixels of the object to the centroid of the cell with a regular object having a value of 1 and irregular objects having a value of 0.

At 1h, hMSCs deposited on sPDA and rPDA surfaces were found to be significantly ($p < 0.01$) more spread than on control surfaces with ~94% and 95% greater relative area, respectively (**Figure 5.5A**). As expected with enhancement in cell area, cells on PDA surfaces had a significantly larger perimeters than on control surfaces. Intriguingly, although cells on sPDA and rPDA had insignificant differences in cell area, calculated perimeter was found to be dissimilar ($p < 0.05$). In fact, when compared to control surfaces, cells on sPDA and rPDA had perimeter enhancement of 34.1 ± 14% and 77.6 ± 11%, respectively. These findings suggest that substantial cell populations on sPDA and rPDA are either undergoing, or have largely completed, early stage isotropic spreading which is responsible for rapid area increases, explaining the similarity in cell area.[65] Such 32.5% difference between PDA samples can be best explained by the increase in protrusive morphologies in rPDA, indicating a greater proportion of the rPDA population undergoing the anisotropic STEPs process, which is characterized by minimal area changes but large perimeter variations reflective of plasma membrane protrusions.[117] This is further confirmed by the significant decrease in form factor for rPDA cells, compared to control and sPDA, which indicates less circular cells.

At 4h, differences in cell area, perimeter and form factor are offset. However, cells on rPDA have a significantly ($p < 0.05$) greater degree of compactness which is indicative of a more irregular morphology, akin to that seen in multipolar morphologies which were predominant in the earlier morphological analysis at this timepoint (**Figure 5.5B**).

Of note, at 24h, cells seeded on rPDA presented with a significant decrease (-19.3%; $p < 0.01$) in comparative size to control surfaces (**Figure 5.5C**). These differences were not significant between PDA surfaces. This reduction in cell area is thought to be due to the transition to late stage morphologies (e.g. multipolar) which are characterized with a more contracted structure. In this context, Rac1-dependent recruitment of Myosin IIA and subsequent actinomyosin mediated contraction during adherence and late stage spreading is indicative of the onset of cell traction forces which translate into polarization and initiation of migratory behavior.[118][119] This is further supported by the significant decrease in perimeter in rPDA versus both sPDA and control surfaces ($p < 0.05$) which can be proposed to be due to the retraction of multiple podia in favor of polarization with the lamella rich front and contracted rear, indicative of a migratory cell responding to environmental physicochemical cues.[120] Important to note is that the form factor of cells on sPDA and rPDA, while both significantly higher and therefore less circular than control, are statistically similar. This indicates that differences in cell area and perimeter resulting from cell body contraction in rPDA are uniform in aspect. Taken together, our results suggest that rPDA surfaces are superior to sPDA surfaces in the promotion of advanced cell spreading, indicating a surface that is increasingly capable of generating meaningful integrin-mediated cell-substrate adhesions that translate downstream into earlier productive traction force via the actin cytoskeleton. As such, initiation of subsequent cell functions, such as the expression of Cyclin D1 for the progression of the cell cycle, can begin earlier and may be further promoted in ways that have yet to be studied (e.g., post-migratory influence on protein expression for enhanced bioactivity including differentiation).[39]

5.3.2.3 Cells deposited on rPDA present with higher levels of focal adhesions (FAs) only in the first 8 hours

The adhesion of a cell to synthetic (e.g. biomaterials) and natural (e.g. extracellular matrix) substrates is regulated by transmembrane integrin-mediated multimeric protein complexes which link the extracellular environment to internal cytoskeletal structures enabling the process of mechanotransduction.[121] Early stage focal complexes ($\sim$0.5 μm in length) signify initial integrin activation and aggregation, forming transient supramolecular complexes, and may undergo maturation into focal adhesions (1-5 μm in length) following adequate stimulation, namely RhoA activity.[122] These highly dynamic structures, critical in the initial interaction with the environment, will form in response to physicochemical stimuli (e.g., microtopography, surface stiffness). The establishment of FAs in turn directs cell behavior, and therefore it is a critical aspect in the investigation of cell-substrate interactions.[123] To better understand the dynamics of focal adhesions in PDA bioactivity, we utilized indirect immunofluorescence to label for the vinculin protein, an early member of the focal adhesion complex.

At 1h, we were unable to discern focal complexes and adhesions on all surfaces due to the contracted nature of adhering cells, which stacked the noise of non-specific binding. In the future we may be able to overcome this by use of specialized techniques for cell-substrate imaging, namely Total-Internal Reflection Fluorescence (TIRF) microscopy. At 4h, both PDA surfaces showed a remarkably significant elevation in focal adhesions ($p < 0.01$) compared to control surfaces with sPDA at +47 ± 11% and rPDA at +72 ± 7% (**Figure 5.6**). Between PDA samples, rPDA was measured to have a significant 17% lead over sPDA ($p < 0.05$). The rapid increase in PDA focal adhesion formation in early timepoints has been previously described and is believed to be the result of activation and

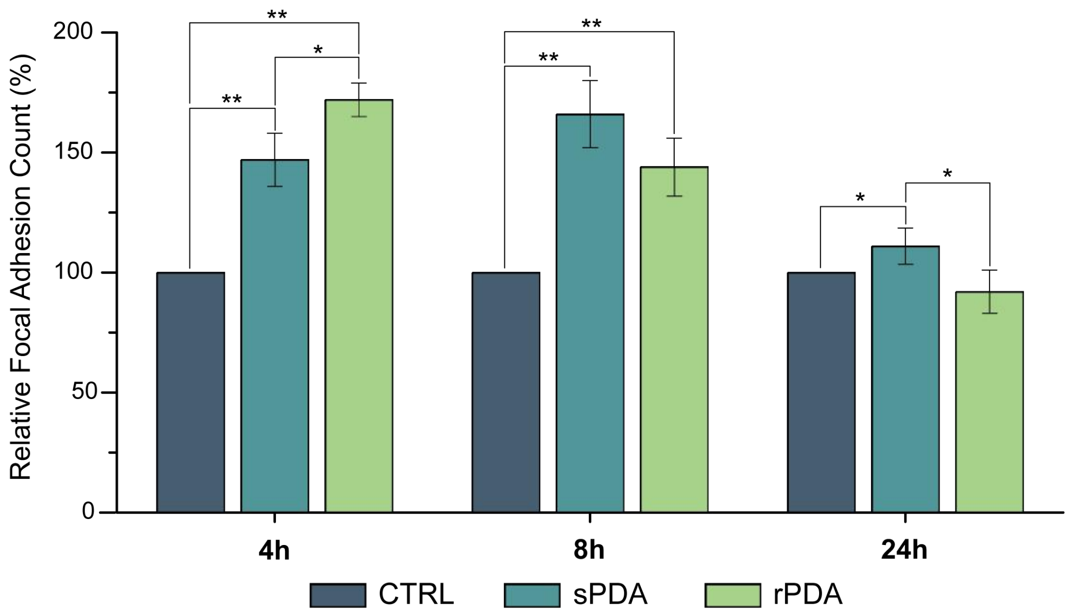

Fig. 5.6 Focal adhesion prevalence in the first 24 hours

Focal adhesions visualized with indirect immunofluorescence using a primary antibody for Vinculin (hVin1). Results are expressed as percentage increase/decrease in respect to untreated BSG (CTRL). ANOVA test: *=$p < 0.05$; **=$p < 0.01$

clustering of integrin $\alpha5\beta1$.[26][124]. The sheer prevalence of the adhesions is an indication of effective generation of cell-substrate interactions, which have undergone productive force transduction through myosin-II mediated contractile forces, and implies the presence of superior physicochemical stimuli.[103] The lead in PDA samples continued into the 8h timepoint with sPDA and rPDA presenting with +66 ± 14% and +44 ± 12% more focal adhesions than control ($p < 0.01$). Of note, the lead that rPDA had over sPDA diminished and were no longer discernible. At 24h, the significant leads in PDA surfaces was heavily reduced. While rPDA was found to have a considerable -17% lag behind sPDA ($p < 0.05$), it was indistinguishable from control surfaces. sPDA on the other hand retained a lessened but still significant +11 ± 6% lead over control surfaces. When taking into consideration the morphological and cell structure data, the reduction in focal adhesion prevalence in the PDA surfaces, namely rPDA, is suggestive of late stage cell spreading and is indicative of a cell entering motility. During the transition to motility, focal adhesions around the periphery of the cell undergo pruning and stress fiber orientation in favor of polarization resulting in a highly dynamics leading lamellipodium and less dynamic rear retracting edge.[125][126] As such, taken together with the morphological and structural data, these results suggest that by 24hr, rPDA surfaces support populations of cells that are at later stages of motility. The comparative decrease between 8h and 24h for sPDA implies the transition to motility as well. Combined data for the control surfaces, however, indicate that the cells are less able to create productive cell-substrate interactions and as such are in earlier stages of cell spreading and/or may be less motile.

5.3.2.4 rPDA promotes cell proliferation in the first 24 hours but trails off within the first 7 days

PDA coatings have long been explored for their ability to enhance cellular viability and cell proliferation for a variety of applications, ranging from revascularization with endothelial cells and scaffolding for cartilage tissue engineering to ceramic enhancement coatings for osteoblasts and cryogel scaffold for stem cell therapy.[127][24][26][128] As of yet, the mechanism to which PDA coatings elicit these cytocompatible and proliferative effects is not fully understood: major limitations in generalized models derive from the high degree of variability between the PDA surfaces being studied, with differences stemming from key variables including deposition method, solvent choice and underlying base substrate. As such, the ability to control for multiple variables while manipulating an experimental (i.e., topography) provides a framework to better understand the mechanism of action with the potential for additional insight into its other noted effects. Cell proliferation was measured through the fixation and fluorescent imaging of stained hMSCs cultured

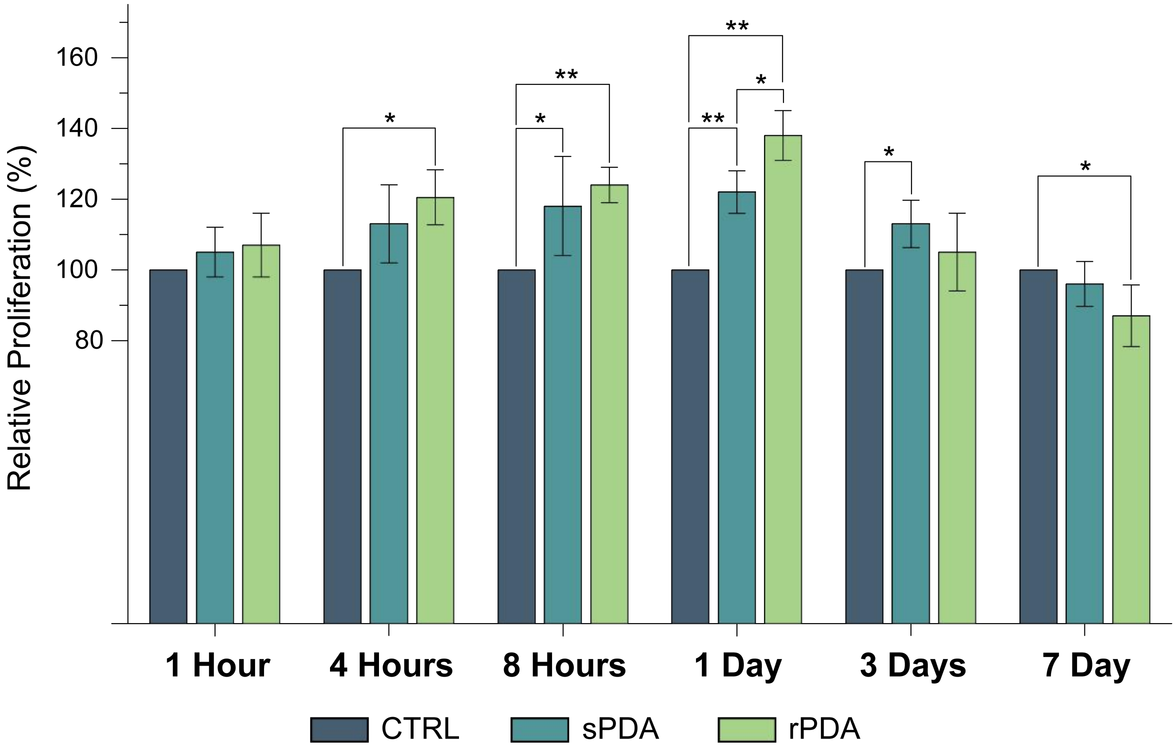

Fig. 5.7 hMSC proliferation measured over 7 days

hMSCs proliferation expressed as percentage difference in respect to untreated BSG (CTRL). ANOVA test: $*=p < 0.05$; $**=p < 0.01$

in serum-containing media over the course of the first 7d post-seeding (**Figure 5.7**) with post-processing and quantification achieved with a custom pipeline in Cell Profiler.

Within the first 4h, rPDA surfaces are shown to have a significant increase (+20.5 ± 8%) in proliferative ability ($p < 0.05$), compared to control surfaces, while sPDA surfaces remain similar. By 8h, the proliferative ability of rPDA over control surfaces is much more evident with a substantially significant rise in relative proliferation (+23.7 ± 5%; $p < 0.01$). Of note, it is not discernible from sPDA surfaces which, however, were similarly found to be different from control surfaces (+18.2 ± 14%; $p < 0.05$). The relatively large variance in the sPDA surfaces at 4h and 8h may be indicative of the heterogeneous progression of spreading and downstream cell cycle initiation between populations on the surface, a theory that is reinforced by the morphological analysis. A method to reduce inherent heterogeneity in seeded cells would be the use of a temporary cell cycle arresting compounds such as Cytochalasin D which prevents actin polymerization and arrests in the G1-S phase transition.[129] 24h after seeding, we encounter peak marked differences between all samples. In comparison to control surfaces, cells on rPDA increase their proliferative induction to a significant +38 ± 7% ($p < 0.01$) with sPDA following closely behind with +22.2 ± 6% ($p < 0.01$). At this point, the PDA surfaces can first be seen to be statistically different with a significant +13.1% in proliferative effect of rPDA over sPDA ($p < 0.05$). Intriguingly, over the following 6 days, the proliferative characteristics of rPDA undergoes a substantial reduction with a significant -11% decrease by Day 7 ($p < 0.05$) in cell count with respect to the control surfaces. Although at 3d sPDA surfaces retain their significant 13% elevation ($p < 0.05$) in comparison to control, this is diminished by Day 7.

Generalized explanation for the advancement of cell proliferation by PDA samples is still inconclusive with most work incomparable based on developed substrate and studied cell lines. Luo et al. (2013) determined that for endothelial cells, the proliferative capability may be associated with the surface quinone content which was enhanced with thermal treatment and subsequently producing greater viability. However, in our case, XPS results indicated no significant difference in functional groups associated with elevated catechol presence on rPDA versus sPDA. Another theory associated is that the proliferative ability is dependent on enhanced serum protein preadsorption. A study by Zhou et al. (2014) found that when comparing the standard deposition method with a rapidly depositing shaking method at similar deposition times, the BSA binding ability was indistinguishable. In addition, previous work in our lab indicated no differences in adsorptive capacity between modified titanium and PDA coated titanium despite considerable bioactive enhancement in spreading and proliferation which extended beyond 3d.[26] Although it has been suggested that cell spreading and proliferation are mainly dependent on surface chemistry while cell elongation and morphology is topography driven (e.g., grooves), our results indicate that given differential proliferation on PDA surfaces of similar chemistry and differing topography, physicochemical characteristics do in fact play a major role in the proliferative inductive capability of PDA.[124]

Of unique interest is the drop off and reduction of relative proliferation in rPDA surfaces at 3d and 7d which were unexpected due to previous results in our lab with MG63 proliferation showing advancement beyond 3d with no substantial reduction.[26] An explanation may be the amplified inductive capacity of rPDA for osteogenic differentiation with PDA in general having been well described and utilized in a variety of methods.[4][130][131] The osteogenic potential of PDA has been correlated to the promotion of integrin clustering and activation of subsequent PI3K signaling pathways.[132] PI3K signaling is enabled by FAK activity at established focal adhesions which in turn has been found to stimulate osteogenic differentiation of hMSCs through ERK-dependent pathways.[133] Thereby rPDA, which we have shown to promote cell spreading and focal adhesion formation, may in turn promote the FAK/PI3K/ERK mediated osteogenic differentiation of hMSCs which is known to have an antagonistic relationship with cell proliferation.[134] Terminal differentiation is correlated to a reduction, and sometimes complete exit, from the cell cycle.

The lack of osteogenic induction by control surfaces allows for the retention of proliferation rates of the non-differentiated hMSCs, which in combination with the potential reduction in cell cycle progression of differentiated cells in rPDA, may explain the relative drop off by 3d and into 7d. This may be supported by the relative decreases in sPDA surfaces at these timepoints which are following a similar, though lagging, trend and may be indicative of the reduced, though present, osteogenic inductive abilities of sPDA.

5.3.2.5 hMSC filopodial projections directly interact with PDA aggregates

SEM imaging confirmed that filopodial-like projections sprouting from hMSCs were more numerous on both PDA surfaces and do directly interact with PDA aggregates (**Figure 5.8**). Further analysis suggests that the filopodia have preference of terminal interaction for aggregates of a critical size, particularly seen on rPDA, with projections seen migrating between larger particles (**Figure 5.8E-F**). Although the qualitative average projection length on rPDA surfaces are seen to be less than sPDA, upon closer qualitative inspection the abundance of projections was much greater on rPDA. The clear majority of projections extending from cells on sPDA seemed unbound to surface aggregates and still in a state of exploratory behavior. However, projections from cells on rPDA surfaces appear terminally bound to the aggregates with an abundance of plasma membrane surrounding the PDA particles (**Figure 5.8F**) thereby increasing the surface area of the cell-substrate interface,

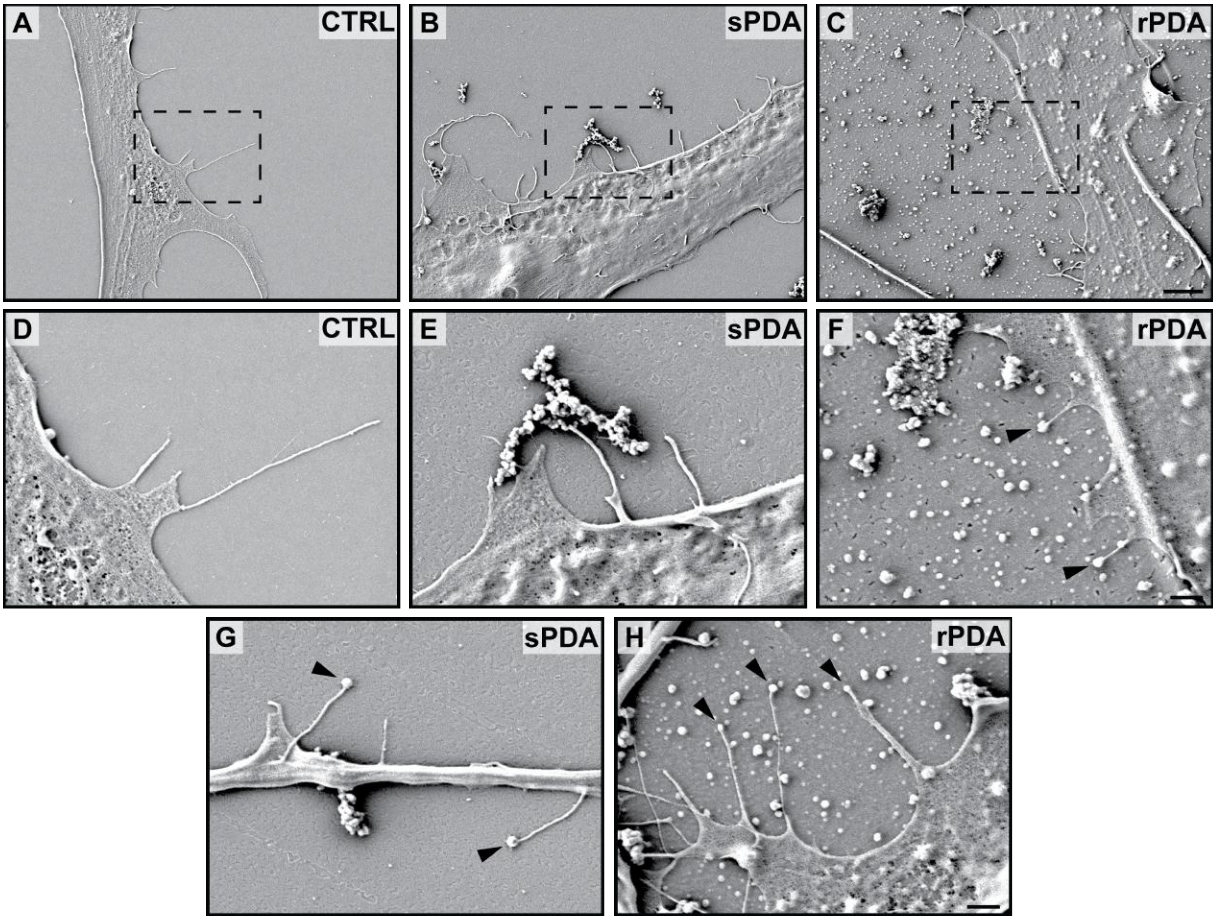

Fig. 5.8 SEM visualization of cell-surface interaction at 24 hours

(**A-C**) Low magnification images of hMSCs seeded on respective surfaces. Mag=3k, Scale Bar=1 μm. (**D-F**) High magnification images of projections from hMSCs. Mag=10k, Scale Bar=4 μm. (**G-H**) Representative images of projections from hMSCs that are bound to features on sPDA and rPDA surfaces. Mag=10k, Scale Bar=4 μm.

suggesting a reinforcement of the cell projection adhesion forces.

5.3.3 Confirming the serum independent component (SIC) of PDA surfaces

In this section, we investigated the SIC through the application of hMSCs, cultured in serum-free media, on sPDA and rPDA surfaces that were pretreated to an overnight incubation in either PBS (no preadsorption) or serum-containing media (preadsorption). Critical measures were performed on (**1**) morphological analysis and (**2**) the determination of a preadsorption effect size for detection and scaling of a serum independent component.

5.3.3.1 A SIC effect on cell morphology exists and is enhanced with serum preadsorption

After 1h and 4h, hMSCs plated on control and PDA samples were imaged and categorized into one of six distinct morphologies, ranked in the progression of cell spreading (**Figure 5.9A**).

At 1h, cells on non-preadsorbed surfaces were found to be primarily protrusive in nature on sPDA (72%) and rPDA (68%) surfaces, while circular cells were the clear majority in control (66%) surfaces (**Figure 5.9B**). Cells on rPDA surfaces, when compared to sPDA, showed a substantial increase in the proportion of the more advanced elongated (14.5% vs. 7.2%) and multipodal (6.8% vs. 3.6%) morphologies. When comparing the non-preadsorption and preadsorption conditions, similar inter-sample differences were seen with rPDA presenting with superior advancement in morphologies (**Figure 5.9C**). In general, the preadsorption of sera protein further progressed cell spreading morphologies, when compared to their respective non-preadsorbed surface.

At 4h, cells adhering on non-preadsorbed and preadsorbed surfaces continued to show increasingly progressed morphologies, compared to control, with similar trends to that at 1h (**Figure 5.9B-C**). Under non-preadsorption, the PDA surfaces presented with most cells on sPDA and rPDA being as either multipodal (46% v. 38%) and multipolar (28% v. 45%). On control samples, there was an absence of multipolar cells with the majority of cells being circular (63%) followed by multipodal (21%). These trends continued in the preadsorbed condition, namely with a significant 52% reduction in circular cells on control samples and an 87% increase in multipodal cells.

Taken together, on all samples and timepoints, cells rPDA surfaces were confirmed to display significantly advanced cell morphologies when compared to sPDA and control surfaces. Herein, we have confirmed that even under serum independent conditions, PDA surfaces enhance the cell spreading of cells, further adding evidence to a serum indepen-

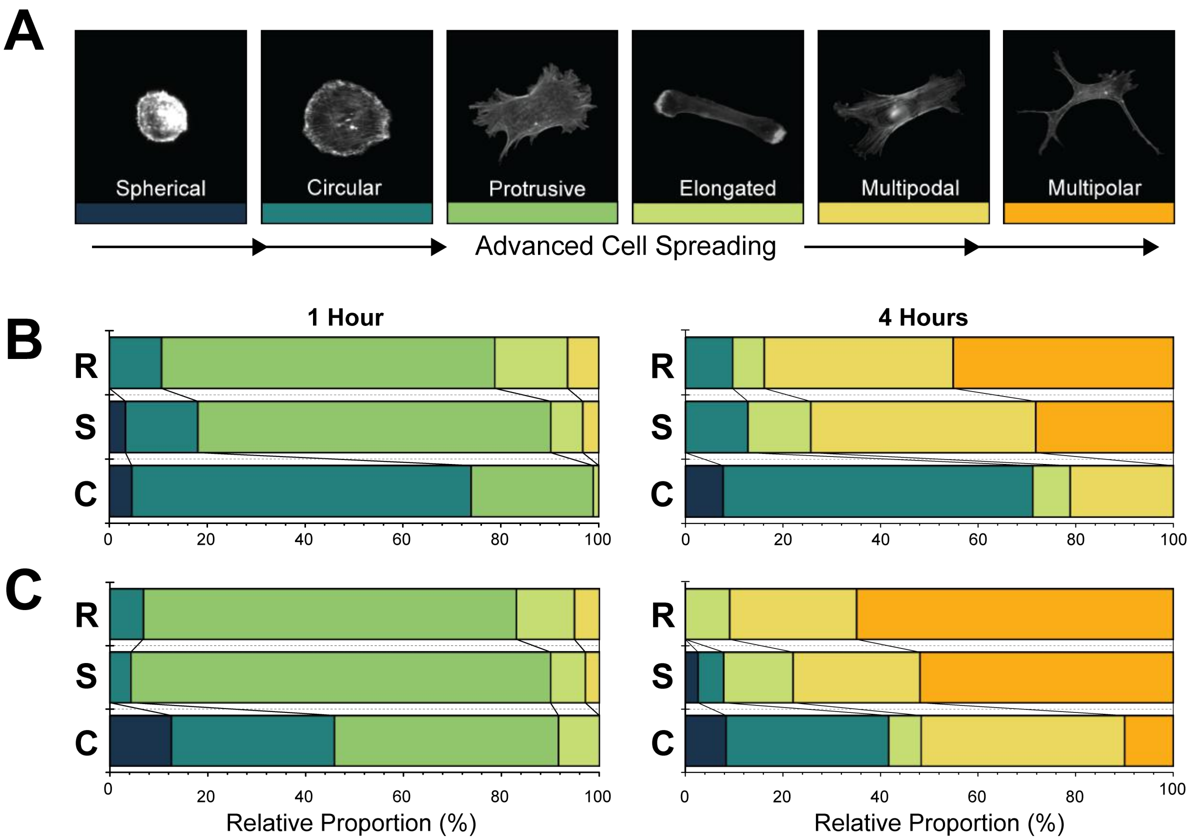

Fig. 5.9 Proportional categorization of early spreading morphologies in the first 4h on preadsorbed and non-preadsorbed surfaces

(**A**) Legend of morphologies exhibited through the advancement of cell spreading with correlated colour bars. (**B-C**) Relative proportions of hMSCs morphologies after incubation in serum-free media on CTRL [C], sPDA [S] and rPDA [R] surfaces. (**B**) Surfaces pretreated in 1X-PBS, no preadsorption. (**C**) Surfaces pretreated in serum containing media, preadsorption. ANOVA test: *=$p < 0.05$; **=$p < 0.01$

dent component. In comparison to normal culturing conditions (**Figure 5.4**), at 1h there is a remarkable decrease in protrusive morphologies, which are indicative of anisotropic spreading, and is in agreement with Dubin-Thaler et al. (2004) whom indicated that serum deprivation promotes isotropic spreading. Although this particular morphology is hindered, the deprivation of circulating serum does not seem to retard the transition to later morphologies at future timepoints. Consequently, this reduction in transient anisotropic spreading in combination with the low proportions of spherical and circular morphologies, in both NPA/PA conditions, indicates that PDA surfaces capable of generating productive cell-substrate adhesions that result in quicker spreading initiation and morphological transitions, instead of relying more heavily on the stochastic environmental sensing of STEPs. It has been proposed in multiple studies that the primary mechanism of action for PDA bioactivity is tied to its adsorptive capacity, despite little consideration taken to inter-study control for physicochemical traits (e.g., aggregate size, distribution).[25][5] Our results clearly show that although serum preadsorption positively impacts morphological progression, as expected, the absence of preadsorbed proteins does not lead to a critical loss of morphological progression in cell spreading especially in rPDA surfaces. This indicates that regardless of chemically similarity and adsorption condition, rPDA possess additional features (e.g., topography) that can further promote the initial behavior of cells beyond that of the classically deposited sPDA.

5.3.3.2 The SIC of PDA surfaces elicits a greater effect on cellular spreading and a lesser effect on proliferation

In our analysis, we determined the optimal measure to conclusively confirm the presence of a SIC was to determine its effect size which we defined as that ratio of a measured variable on preadsorbed surfaces over non-preadsorbed surfaces. The resultant dividend would then provide a reflection of the difference correlated to the specific effects of preadsorption as all other variables would remain constant. While we expect that the addition of serum will produce an increase in all variables under all conditions and timepoints, if no serum independent component existed, the relative effect size should remain statistically consistent across the different samples under the same timepoint. Thereby, this measure not only allows the confirmation of a SIC, but also to which degree the SIC might change dependent on the surface.

In the first 7 days of culture, we have confirmed that a serum independent component on cell spreading exists for PDA surfaces (**Figure 5.10A**). Within the first hour, the preadsorption of sera amounts to a +218% enhancement in cell spreading and is found to be statistically different to the effect size of sPDA (+126%; $p < 0.05$) and rPDA (+78%; $p <$

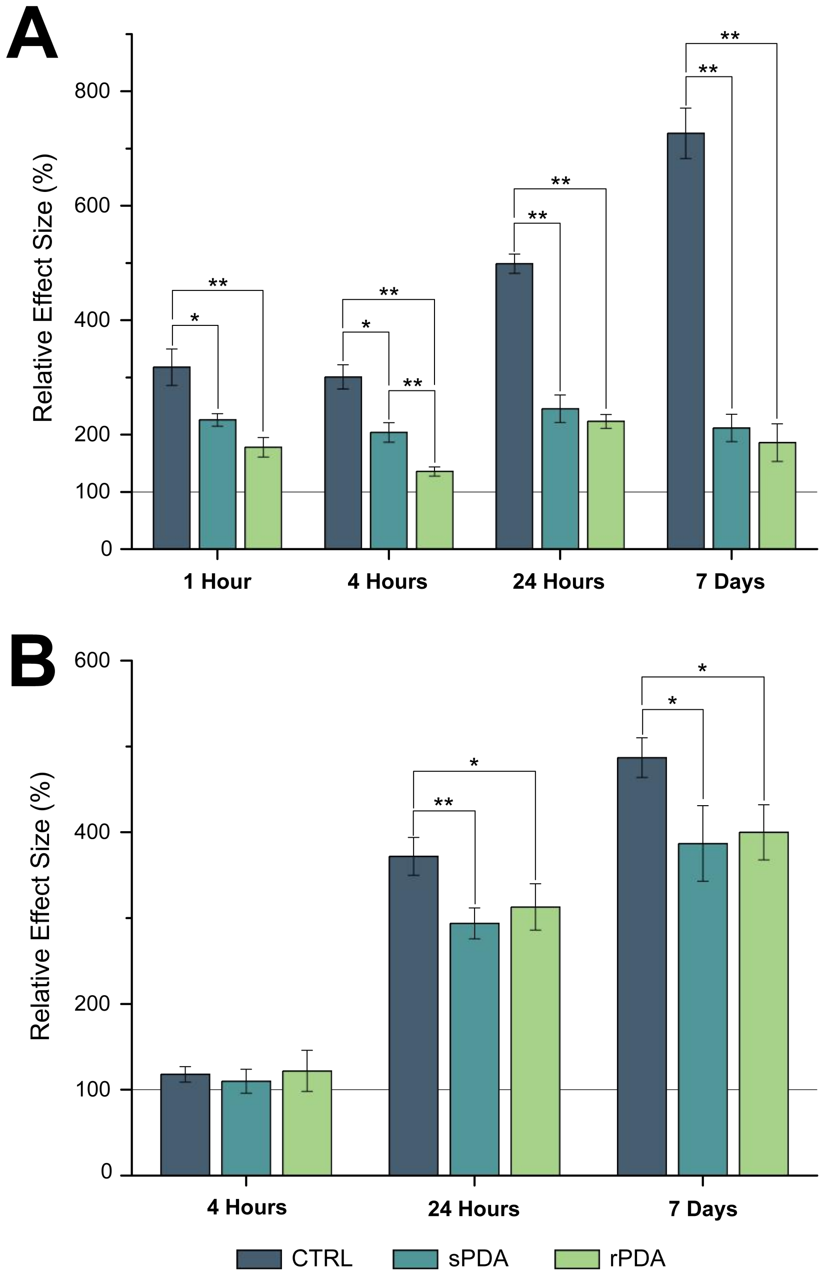

Fig. 5.10 Serum independent component effect size for cell spreading and proliferation

(**A**) Cell spreading. (**B**) Cell proliferation. Effect size is calculated as the dividend of the respective measure (e.g., proliferation) from preadsorbed samples over non-preadsorbed samples. Resultant is the change in measure associated with the preadsorption of serum protein. ANOVA test: *=$p < 0.05$; **=$p < 0.01$

0.01). This confirms that the addition of serum affects the PDA surfaces to a lesser degree and that another beneficial component exists. This trend continues throughout the first 7 days, however interesting to note is that the effect size of the serum preadsorption on control surfaces increases over time as exemplified by a peak effect size at 7 days (+626%). Conversely, the effect sizes of the sPDA and rPDA surfaces stay relatively consistent between timepoints with statistically significant inter-sample differences evident only at the 4h timepoint ($p < 0.05$).

We have also confirmed the presence of a serum independent component on cell proliferation in the first 7 days of culture (**Figure 5.10B**). At 4h, no significant differences were detected as expected due to the early stages of cell spreading whereas adherent cells are noted to arrest cell division until spread on target substrate, allowing for the induction of cyclin D expression.[135] The evidence of a serum independent effect on cell proliferation is first evident after 24h with a relative effect size of +272%, +194% and +213% detected for control, sPDA and rPDA surfaces, respectively. The effect size on control surfaces was found to be statistically higher than the sPDA ($p < 0.01$) and rPDA ($p < 0.05$), however no differences were detected between PDA surfaces. This trend continues at 7d however the preadsorption effect size increases proportionally.

5.4 Conclusions

The first part of this study focused on evaluating whether a unique PDA surface, generated by the simple addition of rotation, can result in a polymeric substrate that enhances the bioactive characteristics beyond that of classically dip-coated PDA. While there have been many studies investigating the bioactivity of PDA, inconsistent control for variables (e.g., deposition method) and lack of sufficient surface analysis which in turn abolishes their external validity.

Surface analysis generated a comprehensive physicochemical characterization of the differences in PDA surfaces. rPDA surfaces, though chemically similar to sPDA, possess a higher degree of wettability associated with the presence of surface-bound and scattered micro-/nano-scale particles resulting in elevated roughness. Through discrimination of PDA aggregates versus the underlying film, we were able to characterize the novel differences in physical characteristics, namely the fact that 1,845% more energy and 381% more force is required to detach from PDA films versus aggregates. This in turn led to the global reduction in required detachment force and energy in rPDA surfaces, due to the ubiquity of large aggregates over the surface. This reduction in required forces may impact the ability for cells to readily generate and collapse adhesions associated with the generation of traction force as seen during spreading and motility.

Cellular assays provided insight into the degree to which the physical differences between PDA surfaces can be attributed to differences in bioactivity. Our results have shown that despite chemical similarity, rPDA surfaces are induce advanced spreading morphologies, confirmed through structural and focal adhesion analysis, at early timepoints beyond that of classically deposited PDA. In addition, rPDA presented with elevated cell proliferation in the first 24hr, an effect that was diminished in the first 7d which may be indicative of differentiation. This elevated bioactivity, coupled with the previously reported enhancement of antibacterial activity, provides further evidence support the use of rPDA has a bioactive coating for orthopedic and dental implants.

The second part of this study was to confirm the existence of a serum-independent component to PDA, a variable that has been largely unconsidered and overshadowed by the adsorptive capacity of the polymer. We have confirmed that there is in fact a SIC of PDA that plays a role on cell spreading and proliferation of hMSCs over the first 7d of cell culture. Of note, in cell spreading, the effect size of preadsorption remained relatively consistent for PDA surfaces throughout timepoints whereas under proliferation, the effect size of the SIC increased over time. This indicates that PDA surfaces contain a serum independent effect that is consistent in its promotion of cell spreading over time, whereas still evident in proliferation studies, the SIC plays a lesser role. As such, these analyses suggest that the differences between sPDA and rPDA surfaces in normal cell culture conditions are not a direct result of differences in respective SICs, suggesting any differences are the result of a variables other than the surface chemistry and adsorptive capacity.

In summary, this study provided novel insight into the physicochemical attributes of sPDA and rPDA coatings. In addition, cellular analyses between them provided context to their differential bioactive effects. We have also confirmed the existence of a serum independent component of PDA coatings which is shown to play a major role in cellular adhesion and less so in proliferation. Our results provide new evidence supporting to use of rPDA has a biomaterials interface while contributing to the further understanding of the mechanism behind PDA bioactivity which may impact and influence the reasoning of both past and future PDA-based studies.

CHAPTER 6

Conclusion and Future Directions

In our first study, we investigated whether the use of polydopamine (PDA) could be utilized as a enhancement coating for titanium surfaces that have previously been subject to oxidative nanopatterning, shown to enhance the availability of surface binding sites associated with improved bioactivity. Through this pursuit, we were able to generation a thorough physicochemical analysis of all generated surfaces which brought to light through spectroscopic techniques the fact that all surfaces were capable of adsorbing sera protein. Of novelty, we were able to determine through mass spectrometry that there were no significant differences in the adsorption of major proteins between NPTi and NPTi+PDA, suggesting that differences in bioactivity are the result of differences in intrinsic properties of the surfaces themselves. Furthermore, we determined that the coating of NPTi with PDA produced a substrate that provided greater bioactive effects as exemplified in the promotion of proliferation, accelerated cell spreading and prolific increases in focal adhesion prevalence. Together, this evidence provided motivation for the determination of a serum independent component of PDA in our second study.

In our second study, we sought to further explain the mechanism behind the bioactive effects of PDA through the exhaustive physicochemical analysis and the biological comparison of two surfaces for which we were able to manipulate key variables (e.g., serum adsorption, circulating sera). In doing so, we have shown that the addition of rotation produces substrate that is chemically similar to statically deposited PDA but possesses a film of larger feature size and an increased density of large aggregates deposited on its surface. Of novelty, we have been able to show a definitive physical difference between aggregates and film, namely the fact that aggregates require drastically less energy to detach from versus underlying film. Accordingly, we believe this discovery may affect the understanding of all PDA surfaces, past and future, as the surface was previously not thought to be heterogenous in its mechanical characteristics. Another feature, that has been largely ignored, is the now confirmed presence of an intrinsic serum independent component of PDA which has shown to strongly influence cell spreading and weakly influence proliferation. Future work could take advantage of the experimental setup of our PDA surfaces, in particular the fact that it has shown to deposit effectively on borosilicate glass. As PDA-coated glass is translucent, advanced live-imaging techniques may be used to measure the real-time behavior of cells on PDA surfaces, an aspect which is untouched due to the limitations imposed by the common use of opaque ceramics for orthopedic-centric research. We believe that given the accelerated transition to a polarized morphology and the proven effectiveness of PDA to generate cell-substrate adhesions, rPDA surfaces may enable enhanced motility which may prove to be of benefit for osseointegration and wound healing. Another aspect would be to run a proteomic analysis to measure key osteogenic markers (e.g., OSX, Runx2) to definitively determine the osteogenic benefit of rPDA over sPDA.

Together, this thesis has provided insight and evidence towards not only the mechanism of action for PDA surfaces, but also the positive application of this polymeric substrate to enhance surfaces (i.e., nanopourous titanium) that may be used in real world orthopedic and periodontal interfaces. Consequently, we believe that evidence is mounting towards the use of rPDA, which can be generated simply with rotation in bulk solution, as a coating for orthopedic prosthetics. We speculate that the process of osseointegration of a theoretical device may be assisted through multiple mechanisms including (**1**) the previously reported intrinsic antibacterial activity preventing infection, (**2**) the bolstered cytocompatibility of bone cells noted in our first study and (**3**) the biocompatibility with multipotent stem cells noted in our second study, including their potential induction toward the osteogenic lineage, generating new bone and opening the door for combination therapy. It is our hope that this work contributes toward the development of next-generation functional biomaterials that will result in medical prosthetics and devices with enhanced functionality and dependency, thereby improving patient quality of life.

Bibliography

1. Nedela, O., Slepicka, P. and Svorcik, V. Surface Modification of Polymer Substrates for Biomedical Applications. *Materials* **10,** 1115 (2017).
2. Zhou, Y., Tsai, T.-L. and Li, W.-J. Strategies to retain properties of bone marrow derived mesenchymal stem cells ex vivo. *Annals of the New York Academy of Sciences* **1409,** 3–17 (Dec. 2017).
3. O'Brien, F. J. Biomaterials and scaffolds for tissue engineering. *Materials Today* **14,** 88–95 (2011).
4. Lee, D. J., Lee, Y. T., Zou, R., Daniel, R. and Ko, C. C. Polydopamine Laced Biomimetic Material Stimulation of Bone Marrow Derived Mesenchymal Stem Cells to Promote Osteogenic Effects. *Scientific Reports* **7,** 12984 (Dec. 2017).
5. Tsai, W. B., Chen, W. T., Chien, H. W., Kuo, W. H. and Wang, M. J. Polydopamine coating to biodegradable polymers for bone tissue engineering. *Journal of Biomaterials Applications* **28,** 837–848 (Feb. 2014).
6. Tran, N. T. *et al.* Polydopamine and Polydopamine-Silane Hybrid Surface Treatments in Structural Adhesive Applications. *Langmuir,* acs.langmuir.7b03178 (2018).
7. Hou, J. *et al.* A novel high drug loading mussel inspired polydopamine hybrid nanoparticle as a pH sensitive vehicle for drug delivery. *International Journal of Pharmaceutics* **533,** 73–83 (Nov. 2017).
8. Qiu, W.-Z., Yang, H.-C. and Xu, Z.-K. Dopamine-assisted co-deposition: An emerging and promising strategy for surface modification. *Advances in Colloid and Interface Science* (Apr. 2018).
9. Ho, C.-C. and Ding, S.-J. The pH-controlled nanoparticles size of polydopamine for anti-cancer drug delivery. *Journal of Materials Science: Materials in Medicine* **24,** 2381–2390 (Oct. 2013).
10. Wei, Q., Zhang, F., Li, J., Li, B. and Zhao, C. Oxidant-induced dopamine polymerization for multifunctional coatings. *Polymer Chemistry* **1,** 1430 (Oct. 2010).

11. Ball, V., Frari, D. D., Toniazzo, V. and Ruch, D. Kinetics of polydopamine film deposition as a function of pH and dopamine concentration: Insights in the polydopamine deposition mechanism. *Journal of Colloid and Interface Science* **386,** 366–372 (Nov. 2012).

12. Chen, X. *et al.* Polydopamine Integrated Nanomaterials and Their Biomedical Applications, 4262–4275 (2015).

13. Kang, K., Choi, I. S. and Nam, Y. A biofunctionalization scheme for neural interfaces using polydopamine polymer. *Biomaterials* **32,** 6374–6380 (Sept. 2011).

14. Su, L., Yu, Y., Zhao, Y. S., Liang, F. and Zhang, X. J. Strong antibacterial polydopamine coatings prepared by a shaking-assisted method. *Scientific Reports* **6,** 24420 (2016).

15. Batul, R., Tamanna, T., Khaliq, A. and Yu, A. Recent progress in the biomedical applications of polydopamine nanostructures. *Biomater. Sci.* **5,** 1204–1229 (2017).

16. Ryu, J., Ku, S. H., Lee, H. and Park, C. B. Mussel-Inspired Polydopamine Coating as a Universal Route to Hydroxyapatite Crystallization. *Advanced Functional Materials* **20,** 2132–2139 (May 2010).

17. Liebscher, J. *et al.* Structure of polydopamine: A never-ending story? *Langmuir* **29,** 10539–10548 (2013).

18. Hong, S. *et al.* Non Covalent Self Assembly and Covalent Polymerization Co Contribute to Polydopamine Formation. *Advanced Functional Materials* **22,** 4711–4717 (Nov. 2012).

19. d'Ischia, M., Napolitano, A., Pezzella, A., Meredith, P. and Sarna, T. Chemical and Structural Diversity in Eumelanins: Unexplored Bio-Optoelectronic Materials. *Angewandte Chemie International Edition* **48,** 3914–3921 (May 2009).

20. Tan, J. and Martic, P. Protein adsorption and conformational change on small polymer particles. *Journal of Colloid and Interface Science* **136,** 415–431 (May 1990).

21. Nishimura, T., Ogino, Y., Ayukawa, Y. and Koyano, K. Influence of the wettability of different titanium surface topographies on initial cellular behavior. *Dental Materials Journal,* 2017–334 (2018).

22. Ding, Y., Floren, M. and Tan, W. Mussel-inspired polydopamine for bio-surface functionalization. *Biosurface and Biotribology* **2,** 121–136 (2016).

23. Liu, J. *et al.* Simple and tunable surface coatings via polydopamine for modulating pharmacokinetics, cell uptake and biodistribution of polymeric nanoparticles. *RSC Advances* **7,** 15864–15876 (Mar. 2017).

24. Tsai, W. B., Chen, W. T., Chien, H. W., Kuo, W. H. and Wang, M. J. Polydopamine coating of scaffolds for articular cartilage tissue engineering. *Acta Biomaterialia* **7,** 4187–4194 (Dec. 2011).

25. Ku, S. H., Ryu, J., Hong, S. K., Lee, H. and Park, C. B. General functionalization route for cell adhesion on non-wetting surfaces. *Biomaterials* **31,** 2535–2541 (Mar. 2010).

26. Steeves, A. J., Atwal, A., Schock, S. C. and Variola, F. Evaluation of the direct effects of poly(dopamine) on the in vitro response of human osteoblastic cells. *Journal of Materials Chemistry B* **4,** 3145–3156 (2016).

27. Pautke, C. *et al.* Characterization of osteosarcoma cell lines MG63, Saos2 and U2 OS in comparison to human osteoblasts. *Anticancer research* **24,** 3743–8.

28. Czekanska, E. M., Stoddart, M. J., Richards, R. G. and Hayes, J. S. In search of an osteoblast cell model for in vitro research. *European cells and materials* **24,** 1–17 (July 2012).

29. Weissman, I. L. Stem cells: units of development, units of regeneration, and units in evolution. *Cell* **100,** 157–68 (Jan. 2000).

30. Hagbard, L. *et al.* Developing defined substrates for stem cell culture and differentiation. *Philosophical transactions of the Royal Society of London. Series B, Biological sciences* **373** (July 2018).

31. Wang, Y. *et al.* Bioengineered Systems and Designer Matrices That Recapitulate the Intestinal Stem Cell Niche. *Cellular and molecular gastroenterology and hepatology* **5,** 440–453 (Mar. 2018).

32. Shafei, A. E.-S. *et al.* Mesenchymal stem cell therapy: A promising cell-based therapy for treatment of myocardial infarction. *The Journal of Gene Medicine* **19,** e2995 (Dec. 2017).

33. Nam, Y., Rim, Y. A., Lee, J. and Ju, J. H. Current Therapeutic Strategies for Stem Cell-Based Cartilage Regeneration. *Stem Cells International* **2018,** 1–20 (2018).

34. De Bari, C. and Roelofs, A. J. Stem cell-based therapeutic strategies for cartilage defects and osteoarthritis. *Current Opinion in Pharmacology* **40,** 74–80 (June 2018).

35. Leijnse, N., Oddershede, L. B. and Bendix, P. M. Helical buckling of actin inside filopodia generates traction. *Proceedings of the National Academy of Sciences of the United States of America* **112,** 136–41 (Jan. 2015).

36. Tamada, A., Kawase, S., Murakami, F. and Kamiguchi, H. Autonomous right-screw rotation of growth cone filopodia drives neurite turning. *The Journal of cell biology* **188,** 429–41 (Feb. 2010).

37. McNamara, L. E. *et al.* Investigation of the limits of nanoscale filopodial interactions. *Journal of Tissue Engineering* **5,** 204173141453617 (Feb. 2014).

38. Sit, S.-T. and Manser, E. Rho GTPases and their role in organizing the actin cytoskeleton. *Journal of cell science* **124,** 679–83 (Mar. 2011).

39. Watts, K., Cottrell, E., Hoban, P. and Spiteri, M. RhoA signaling modulates cyclin D1 expression in human lung fibroblasts; implications for idiopathic pulmonary fibrosis. *Respiratory Research* **7,** 88 (Dec. 2006).

40. Ohashi, K., Fujiwara, S. and Mizuno, K. Roles of the cytoskeleton, cell adhesion and rho signalling in mechanosensing and mechanotransduction. *Journal of Biochemistry* **161,** mvw082 (Jan. 2017).

41. Zhang, C. *et al.* Deposition and Adhesion of Polydopamine on the Surfaces of Varying Wettability. *ACS Applied Materials and Interfaces* **9,** 30943–30950 (2017).

42. Chen, Q. *et al.* Fate decision of mesenchymal stem cells: adipocytes or osteoblasts? *Cell Death and Differentiation* **23,** 1128–1139 (July 2016).

43. Hynes, R. O. Integrins: Bidirectional, Allosteric Signaling Machines. *Cell* **110,** 673–687 (Sept. 2002).

44. Paszek, M. J., Boettiger, D., Weaver, V. M. and Hammer, D. A. Integrin Clustering Is Driven by Mechanical Resistance from the Glycocalyx and the Substrate. *PLoS Computational Biology* **5** (ed Lauffenberger, D.) e1000604 (Dec. 2009).

45. O'Toole, T. E. *et al.* Modulation of the affinity of integrin alpha IIb beta 3 (GPIIb-IIIa) by the cytoplasmic domain of alpha IIb. *Science (New York, N.Y.)* **254,** 845–7 (Nov. 1991).

46. Luo, B.-H., Carman, C. V. and Springer, T. A. Structural Basis of Integrin Regulation and Signaling. *Annual Review of Immunology* **25,** 619–647 (Apr. 2007).

47. Gardel, M. L., Schneider, I. C., Aratyn-Schaus, Y. and Waterman, C. M. Mechanical Integration of Actin and Adhesion Dynamics in Cell Migration. *Annual Review of Cell and Developmental Biology* **26,** 315–333 (Nov. 2010).

48. Dalby, M. J., Gadegaard, N. and Oreffo, R. O. C. Harnessing nanotopography and integrin-matrix interactions to influence stem cell fate. *Nature Materials* **13,** 558–569 (June 2014).

49. Del Rio, A. *et al.* Stretching Single Talin Rod Molecules Activates Vinculin Binding. *Science* **323,** 638–641 (Jan. 2009).

50. Dumbauld, D. W. *et al.* How vinculin regulates force transmission. *Proceedings of the National Academy of Sciences of the United States of America* **110,** 9788–93 (June 2013).

51. Humphries, J. D. *et al.* Vinculin controls focal adhesion formation by direct interactions with talin and actin. *Journal of Cell Biology* **179,** 1043–1057 (2007).

52. Rothenberg, K. E., Scott, D. W., Christoforou, N. and Hoffman, B. D. Vinculin Force-Sensitive Dynamics at Focal Adhesions Enable Effective Directed Cell Migration. *Biophysical Journal* **114,** 1680–1694 (Apr. 2018).

53. Gallant, N. D., Michael, K. E. and García, A. J. Cell adhesion strengthening: contributions of adhesive area, integrin binding, and focal adhesion assembly. *Molecular biology of the cell* **16,** 4329–40 (Sept. 2005).

54. Ladoux, B. and Nicolas, A. Physically based principles of cell adhesion mechanosensitivity in tissues. *Reports on Progress in Physics* **75,** 116601 (Nov. 2012).

55. Swaminathan, V. and Waterman, C. M. The molecular clutch model for mechanotransduction evolves. *Nat Cell Biol* **18,** 459–61 (2016).

56. Zhang, H. *et al.* Proliferation of preosteoblasts on TiO2 nanotubes is FAK/RhoA related. *RSC Advances* **5,** 38117–38124 (2015).

57. Gilmore, A. P. and Romer, L. H. Inhibition of focal adhesion kinase (FAK) signaling in focal adhesions decreases cell motility and proliferation. *Molecular biology of the cell* **7,** 1209–24 (Aug. 1996).

58. Partridge, M. A. Initiation of Attachment and Generation of Mature Focal Adhesions by Integrin-containing Filopodia in Cell Spreading. *Molecular Biology of the Cell* **17,** 4237–4248 (July 2006).

59. Cavalcanti-Adam, E. A. *et al.* Cell Spreading and Focal Adhesion Dynamics Are Regulated by Spacing of Integrin Ligands. *Biophysical Journal* **92,** 2964–2974 (Apr. 2007).

60. Paluch, E. K., Aspalter, I. M. and Sixt, M. Focal Adhesion Independent Cell Migration. *Annual Review of Cell and Developmental Biology* **32,** 469–490 (Oct. 2016).

61. Lin, S. *et al.* Tuning heterogeneous poly(dopamine) structures and mechanics: in silico covalent cross-linking and thin film nanoindentation. *Soft matter* **10,** 457–64 (Jan. 2014).

62. Lo, C.-M., Wang, H.-B., Dembo, M. and Wang, Y.-l. Cell Movement Is Guided by the Rigidity of the Substrate. *Biophysical Journal* **79,** 144–152 (July 2000).

63. Geiger, B., Spatz, J. P. and Bershadsky, A. D. Environmental sensing through focal adhesions. *Nature Reviews Molecular Cell Biology* **10,** 21–33 (Jan. 2009).

64. Cuvelier, D. *et al.* The Universal Dynamics of Cell Spreading. *Current Biology* **17,** 694–699 (Apr. 2007).

65. Dubin-Thaler, B., Gianonne, G., Döbereiner, H.-G. and Sheetz, M. P. Nanometer analysis of cell spreading on matric-coated surfaces reveals two distinct cell states and STEPs. *Biophysical Journal* **86,** 1794–1806 (2004).

66. Letourneau, P. C. and Shattuck, T. A. Distribution and possible interactions of actin-associated proteins and cell adhesion molecules of nerve growth cones. *Development (Cambridge, England)* **105,** 505–19 (Mar. 1989).

67. Van Haastert, P. J. M., Keizer-Gunnink, I. and Kortholt, A. Coupled excitable Ras and F-actin activation mediates spontaneous pseudopod formation and directed cell movement. *Molecular biology of the cell* **28,** 922–934 (Apr. 2017).

68. Insall, R. The interaction between pseudopods and extracellular signalling during chemotaxis and directed migration. *Current Opinion in Cell Biology* **25,** 526–531 (Oct. 2013).

69. Punzón-Quijorna, E. *et al.* Nanostructured porous silicon micropatterns as a tool for substrate-conditioned cell research. *Nanoscale research letters* **7,** 396 (July 2012).

70. Bell, S. and Terentjev, E. M. Focal Adhesion Kinase: The Reversible Molecular Mechanosensor. *Biophysical Journal* **112,** 2439–2450 (June 2017).

71. Nguyen, A. T., Sathe, S. R. and Yim, E. K. F. From nano to micro: topographical scale and its impact on cell adhesion, morphology and contact guidance. *Journal of Physics: Condensed Matter* **28,** 183001 (May 2016).

72. Yang, L. *et al.* Disordered Topography Mediates Filopodial Extension and Morphology of Cells on Stiff Materials. *Advanced Functional Materials* **27,** 1702689 (Oct. 2017).

73. Wong, S., Guo, W.-H. and Wang, Y.-L. Fibroblasts probe substrate rigidity with filopodia extensions before occupying an area. *Proceedings of the National Academy of Sciences of the United States of America* **111,** 17176–81 (Dec. 2014).

74. Bangasser, B. L. *et al.* Shifting the optimal stiffness for cell migration. *Nature Communications* **8,** 15313 (May 2017).

75. Rezende, C. A., Lee, L.-T. and Galembeck, F. Surface Mechanical Properties of Thin Polymer Films Investigated by AFM in Pulsed Force Mode. *Langmuir* **25,** 9938–9946 (Sept. 2009).

76. Lee, H., Rho, J. and Messersmith, P. B. Facile Conjugation of Biomolecules onto Surfaces via Mussel Adhesive Protein Inspired Coatings. *Advanced materials (Deerfield Beach, Fla.)* **21,** 431–434 (Jan. 2009).

77. Zangmeister, R., Morris, T. and Tarlov, M. Characterization of Polydopamine Thin Films Deposited at Short Times by Autoxidation of Dopamine. *Langmuir* **29,** 8619–8628 (July 2013).

78. Wei, H. *et al.* Stability of polydopamine and poly(DOPA) melanin-like films on the surface of polymer membranes under strongly acidic and alkaline conditions. *Colloids and Surfaces B: Biointerfaces* **110,** 22–28 (Oct. 2013).

79. Baginska, M., Blaiszik, B. J., Rajh, T., Sottos, N. R. and White, S. R. Enhanced autonomic shutdown of Li-ion batteries by polydopamine coated polyethylene microspheres. *Journal of Power Sources* **269,** 735–739 (Dec. 2014).

80. Carpenter, A. E. *et al.* CellProfiler: image analysis software for identifying and quantifying cell phenotypes. *Genome Biology* **7,** R100 (Oct. 2006).

81. Yi, J.-H. *et al.* Characterization of a bioactive nanotextured surface created by controlled chemical oxidation of titanium. *Surface Science* **600,** 4613–4621 (Oct. 2006).

82. Ketabchi, A., Komm, K., Miles Rossouw, M., Cassani, D. and Variola, F. Nanoporous titanium surfaces for sustained elution of proteins and antibiotics. *PloS one* **9** (Mar. 2014).

83. Variola, F., Francis Zalzal, S., Leduc, A., Barbeau, J. and Nanci, A. Oxidative nanopatterning of titanium generates mesopourous surfaces with antimicrobial properties. *International Journal of Nanomedicine* **9,** 2319 (May 2014).

84. Bernsmann, F., Ersen, O., Jan, E., Kotov, N. A. and Ball, V. Melanin Containing Films Growth from Dopamine Solutions versus Layer by Layer Deposition. *ChemPhysChem* **11,** 3299–3305 (Oct. 2010).

85. Schmidt, U., Hild, S., Ibach, W. and Hollricher, O. Characterization of Thin Polymer Films on the Nanometer Scale with Confocal Raman AFM. *Macromolecular Symposia* **230,** 133–143 (Dec. 2005).
86. Stockle, B. *et al.* Precise Control of Polydopamine Film Formation by Electropolymerization. *Macromolecular Symposia* **346,** 73–81 (Dec. 2014).
87. Nirasay, S., Badia, A., Leclair, G., Claverie, J. and Marcotte, I. Polydopamine Supported Lipid Bilayers. *Materials* **5,** 2621–2636 (Dec. 2012).
88. Dimitriadis, E. K., Horkay, F., Maresca, J., Kachar, B. and Chadwick, R. S. Determination of elastic moduli of thin layers of soft material using the atomic force microscope. *Biophysical journal* **82,** 2798–810 (May 2002).
89. Shalev, T., Gopin, A., Bauer, M., Stark, R. W. and Rahimipour, S. Non-leaching antimicrobial surfaces through polydopamine bio-inspired coating of quaternary ammonium salts or an ultrashort antimicrobial lipopeptide. *J. Mater. Chem.* **22,** 2026–2032 (Jan. 2012).
90. Variola, F. Atomic force microscopy in biomaterials surface science. *Phys. Chem. Chem. Phys.* **17,** 2950–2959 (2015).
91. Ayas, S. *et al.* Label-free nanometer-resolution imaging of biological architectures through surface enhanced Raman scattering. *Scientific reports* **3,** 2624 (Dec. 2013).
92. Zhou, P. *et al.* Rapidly-deposited polydopamine coating via high temperature and vigorous stirring: formation, characterization and biofunctional evaluation. *PloS one* **9** (Nov. 2014).
93. Variola, F., Nanci, A. and Rosei, F. Assessment of the Titanium Dioxide Absorption Coefficient by Grazing-Angle Fourier Transform Infrared and Ellipsometric Measurements. *Applied Spectroscopy* **63,** 1187–1190 (Oct. 2009).
94. Kasemo, B. Biological surface science. *Surface Science* **500,** 656–677 (Mar. 2002).
95. Wilson, C. J., Clegg, R. E., Leavesley, D. I. and Pearcy, M. J. Mediation of Biomaterial Cell Interactions by Adsorbed Proteins. *Tissue Engineering* **11,** 1–18 (Jan. 2005).
96. Barth, A. and Zscherp, C. What vibrations tell about proteins. *Quarterly Reviews of Biophysics* **35,** 369–430 (Nov. 2002).
97. Kamentsky, L. *et al.* Improved structure, function and compatibility for CellProfiler: modular high-throughput image analysis software. *Bioinformatics* **27,** 1179–1180 (Apr. 2011).

98. Richert, L. *et al.* Surface Nanopatterning to Control Cell Growth. *Advanced Materials* **20,** 1488–1492 (Apr. 2008).

99. Vetrone, F. *et al.* Nanoscale Oxidative Patterning of Metallic Surfaces to Modulate Cell Activity and Fate. *Nano Letters* **9,** 659–665 (Feb. 2009).

100. Hiraguchi, Y. *et al.* Effect of the distribution of adsorbed proteins on cellular adhesion behaviors using surfaces of nanoscale phase reversed amphiphilic block copolymers. *Acta Biomaterialia* **10,** 2988–2995 (July 2014).

101. Ren, Z.-X., Yu, H.-B., Li, J.-S., Shen, J.-L. and Du, W.-S. Suitable parameter choice on quantitative morphology of A549 cell in epithelial-mesenchymal transition. *Bioscience reports* **35** (Apr. 2015).

102. Eidet, J. R., Pasovic, L., Maria, R., Jackson, C. J. and Utheim, T. P. Objective assessment of changes in nuclear morphology and cell distribution following induction of apoptosis. *Diagnostic Pathology* **9,** 92 (May 2014).

103. Kuo, J.-C. Focal adhesions function as a mechanosensor. *Progress in molecular biology and translational science* **126,** 55–73 (2014).

104. Biggs, M. J. and Dalby, M. J. Focal adhesions in osteoneogenesis. *Proceedings of the Institution of Mechanical Engineers, Part H: Journal of Engineering in Medicine* **224,** 1441–1453 (Dec. 2010).

105. Price, L. S., Leng, J., Schwartz, M. A. and Bokoch, G. M. Activation of Rac and Cdc42 by Integrins Mediates Cell Spreading. *Molecular Biology of the Cell* **9,** 1863–1871 (July 1998).

106. Marjoram, R., Lessey, E. and Burridge, K. Regulation of RhoA Activity by Adhesion Molecules and Mechanotransduction. *Current Molecular Medicine* **14,** 199–208 (2014).

107. Arthur, W. T. and Burridge, K. RhoA Inactivation by p190RhoGAP Regulates Cell Spreading and Migration by Promoting Membrane Protrusion and Polarity. *Molecular Biology of the Cell* **12,** 2711–2720 (Sept. 2001).

108. McBeath, R., Pirone, D. M., Nelson, C. M., Bhadriraju, K. and Chen, C. S. Cell shape, cytoskeletal tension, and RhoA regulate stem cell lineage commitment. *Developmental Cell* **6,** 483–495 (2004).

109. Patel, K. *et al.* Polydopamine films change their physicochemical and antimicrobial properties with a change in reaction conditions. *Physical Chemistry Chemical Physics* **20,** 5744–5755 (Feb. 2018).

110. Jiang, J., Zhu, L. L., Zhu, L. L., Zhu, B. and Xu, Y. Surface characteristics of a self-polymerized dopamine coating deposited on hydrophobic polymer films. *Langmuir* **27,** 14180–14187 (Dec. 2011).

111. Doksani, Y., Wu, J. Y., De Lange, T. and Zhuang, X. XSuper-resolution fluorescence imaging of telomeres reveals TRF2-dependent T-loop formation. *Cell* **155,** 345–356 (2013).

112. Liu, Y., Ai, K. and Lu, L. Polydopamine and its derivative materials: Synthesis and promising applications in energy, environmental, and biomedical fields. *Chemical Reviews* **114,** 5057–5115 (2014).

113. Clark, M. B., Gardella, J. A., Schultz, T. M., Patil, D. G. and Salvati, L. Solid-state analysis of eumelanin biopolymers by electron spectroscopy for chemical analysis. *Analytical Chemistry* **62,** 949–956 (May 1990).

114. Della Vecchia, N. F. *et al.* Tris Buffer Modulates Polydopamine Growth, Aggregation, and Paramagnetic Properties. *Langmuir* **30,** 9811–9818 (Aug. 2014).

115. Davey, G., Buzzai, M. and Assoian, R. K. Reduced expression of (alpha)5(beta)1 integrin prevents spreading-dependent cell proliferation. *Journal of cell science* **112 (Pt 24),** 4663–72 (Dec. 1999).

116. Liu, Y., Ai, K. and Lu, L. Polydopamine and its derivative materials: Synthesis and promising applications in energy, environmental, and biomedical fields. *Chemical Reviews* **114,** 5057–5115 (May 2014).

117. Reinhart-King, C. A., Dembo, M. and Hammer, D. A. The Dynamics and Mechanics of Endothelial Cell Spreading. *Biophysical Journal* **89,** 676–689 (July 2005).

118. Kuo, J.-C. Mechanotransduction at focal adhesions: integrating cytoskeletal mechanics in migrating cells. *Journal of cellular and molecular medicine* **17,** 704–12 (June 2013).

119. Paliashvili, K. Identification of novel Focal Adhesion Kinase binding partners and their biological functions in cancer cells Ketevan Paliashvili, 1–208 (2015).

120. Smith, L., Cho, S. and Discher, D. E. Mechanosensing of matrix by stem cells: From matrix heterogeneity, contractility, and the nucleus in pore-migration to cardiogenesis and muscle stem cells in vivo. *Seminars in Cell and Developmental Biology* **71,** 84–98 (Nov. 2017).

121. Cavalcanti-Adam, E. A. *et al.* Cell spreading and focal adhesion dynamics are regulated by spacing of integrin ligands. *Biophysical journal* **92,** 2964–74 (Apr. 2007).

122. Wozniak, M. A., Modzelewska, K., Kwong, L. and Keely, P. J. Focal adhesion regulation of cell behavior. *Biochimica et Biophysica Acta (BBA) - Molecular Cell Research* **1692,** 103–119 (July 2004).

123. McNamara, L. E. *et al.* The role of microtopography in cellular mechanotransduction. *Biomaterials* **33,** 2835–2847 (Apr. 2012).

124. Wang, J. L. *et al.* Direct Adhesion of Endothelial Cells to Bioinspired Poly(dopamine) Coating Through Endogenous Fibronectin and Integrin a5b1. *Macromolecular Bioscience* **13,** 483–493 (2013).

125. Kim, D.-H. and Wirtz, D. Focal adhesion size uniquely predicts cell migration. *FASEB journal : official publication of the Federation of American Societies for Experimental Biology* **27,** 1351–61 (Apr. 2013).

126. Parsons, J. T., Horwitz, A. R. and Schwartz, M. A. Cell adhesion: integrating cytoskeletal dynamics and cellular tension. *Nature reviews. Molecular cell biology* **11,** 633–43 (Sept. 2010).

127. Zhou, W., Xiao, X., Cai, M. and Yang, L. Polydopamine coated, nitrogen doped, hollow carbon sulfur double layered core shell structure for improving lithium sulfur batteries. *Nano Letters* **14,** 5250–5256 (2014).

128. Razavi, M., Hu, S. and Thakor, A. S. A collagen based cryogel bioscaffold coated with nanostructured polydopamine as a platform for mesenchymal stem cell therapy. *Journal of Biomedical Materials Research Part A* (Apr. 2018).

129. Chen, L., Hu, H., Qiu, W., Shi, K. and Kassem, M. Actin depolymerization enhances adipogenic differentiation in human stromal stem cells. *Stem Cell Research* **29,** 76–83 (May 2018).

130. Wu, C., Fan, W., Chang, J. and Xiao, Y. Mussel-inspired porous SiO2 scaffolds with improved mineralization and cytocompatibility for drug delivery and bone tissue engineering. *Journal of Materials Chemistry* **21,** 18300 (Nov. 2011).

131. Xue, R., Li, J. Y.-S., Yeh, Y., Yang, L. and Chien, S. Effects of matrix elasticity and cell density on human mesenchymal stem cells differentiation. *Journal of Orthopaedic Research* **31,** 1360–1365 (Sept. 2013).

132. Lee, J. S., Yi, J.-K., An, S. Y. and Heo, J. S. Increased Osteogenic Differentiation of Periodontal Ligament Stem Cells on Polydopamine Film Occurs via Activation of Integrin and PI3K Signaling Pathways. *Cellular Physiology and Biochemistry* **34,** 1824–1834 (2014).

133. Salasznyk, R. M., Klees, R. F., Williams, W. A., Boskey, A. and Plopper, G. E. Focal adhesion kinase signaling pathways regulate the osteogenic differentiation of human mesenchymal stem cells. *Experimental cell research* **313,** 22–37 (Jan. 2007).

134. Ruijtenberg, S. and van den Heuvel, S. Coordinating cell proliferation and differentiation: Antagonism between cell cycle regulators and cell type-specific gene expression. *Cell Cycle* **15,** 196–212 (Jan. 2016).

135. Margadant, C. *et al.* Focal adhesion signaling and actin stress fibers are dispensable for progression through the ongoing cell cycle. *Journal of cell science* **120,** 66–76 (Jan. 2007).